MATHEMATICAL MODELS AND NUMERICAL METHODS FOR POROUS MEDIA FLOWS ARISING IN CHEMICAL ENHANCED OIL RECOVERY

A Dissertation

by

SOURAV DUTTA

Submitted to the Office of Graduate and Professional Studies of
Texas A&M University
in partial fulfillment of the requirements for the degree of

DOCTOR OF PHILOSOPHY

Chair of Committee,	Prabir Daripa
Committee Members,	Peter Howard
	Michael King
	Peter Kuchment
	Raytcho Lazarov
Head of Department,	Emil Straube

August 2017

Major Subject: Mathematics

ABSTRACT

We study multiphase, multicomponent flow of incompressible fluids through porous media. Such flows are of vital interest in various applied science and engineering disciplines like geomechanics, groundwater flow and soil-remediation, construction engineering, hydrogeology, biology and biophysics, manufacturing of polymer composites, reservoir engineering, etc. In particular, we study chemical Enhanced Oil Recovery (EOR) techniques like polymer and surfactant-polymer (SP) flooding in two space dimensions. We develop a mathematical model for incompressible, immiscible, multicomponent, two-phase porous media flow by introducing a new global pressure function in the context of SP flooding. This model consists of a system of flow equations that incorporates the effect of capillary pressure and also the effect of polymer and surfactant on viscosity, interfacial tension and relative permeabilities of the two phases.

We propose a hybrid method to solve the coupled system of equations for global pressure, water saturation, polymer concentration and surfactant concentration in which the elliptic global pressure equation is solved using a discontinuous finite element method and the transport equations for water saturation and concentrations of the components are solved by a Modified Method Of Characteristics (MMOC) in the multicomponent setting. We also prove convergence of the hybrid method by assuming an optimal $O(h)$ order estimate for the gradient of the pressure obtained using the discontinuous finite element method and using this estimate to analyze the convergence of the MMOC method for the transport system. The novelty in this proof is the convergence analysis of the MMOC procedure for a nonlinear system of transport equations as opposed to previous results which have only considered a single transport equation. For this purpose, we consider an analogous single-component system of transport equations and discuss the possibility

of extending the analysis to multicomponent systems. We obtain error estimates for the transport variables and these estimates are validated numerically in two ways. Firstly, we compare them with numerical error estimates obtained using an exact solution. Secondly, we also compare these estimates with results obtained from realistic numerical simulations of flows arising in enhanced oil recovery processes.

This mathematical model and hybrid numerical procedure have been successfully applied to solve a variety of configurations representing different chemical flooding processes arising in EOR. We perform numerical simulations to validate the method and to demonstrate its robustness and efficiency in capturing the details of the various underlying physical and numerical phenomena. We introduce a new technique to test for the influence of grid alignment on the numerical results and apply this technique on the hybrid method to show that the grid orientation effect is negligible. We perform simulations using different types of heterogeneous permeability field data which include piecewise discontinuous fields, channel-like fractures, real world SPE10 models and multiscale fields generated using a stationary, isotropic, fractal Gaussian distribution. Finally, we also use the method to compare the relative performance of flooding schemes with different injection profiles both in a quarter five-spot as well as a rectangular reservoir geometry.

DEDICATION

I would like to dedicate this to my mother, my father, and my late grandmother. They have been a constant source of inspiration and motivation for all of my endeavors. Their unwavering faith and conviction in me helped me get through some of the most difficult times when failure and helplessness would make it extremely challenging to carry on. This is also dedicated to Shahina who has been the single greatest reason that led me to embark on this journey of graduate study. It had started with a shared dream and this dissertation is the ultimate culmination of that dream. I am eternally in debt for her unconditional support through all the trying times and for always being the voice of reason and a beacon of hope. Needless to say, this dissertation wouldn't have been possible without the presence of any one of these pillars of my life.

ACKNOWLEDGMENTS

First and foremost, I would like to thank my advisor, Dr. Prabir Daripa, for all his help and guidance. I would also like to thank my committee members - Dr. Peter Howard, Dr. Michael King, Dr. Peter Kuchment and Dr. Raytcho Lazarov, for their helpful comments and insights. I am thankful to my research group mates, Dr. Craig Gin and Zhiying Hai, for the numerous brainstorming sessions and fruitful discussions that helped me delve deeper into the subject. I would also like to thank the High Performance Research Computing (HPRC) Center of Texas A&M University. Many of the intensive numerical simulations would not have been possible without the computing resources provided by HPRC, TAMU. Finally, I would like to thank the TAMU Department of Mathematics and Dr. Daripa for supporting me as a Teaching Assistant and as a Research Assistant over the last several years.

At a personal level, I am eternally grateful for the support and company of my invaluable friends and colleagues, who have undoubtedly made the experience of graduate school most memorable for me and will be deeply missed as I venture towards the next challenges of life. I am also indebted to the wonderful staff members of the Mathematics Department, in particular, Ms. Monique Stewart and Ms. Judy Muzny, for making my journey through the graduate program as smooth as possible.

CONTRIBUTORS AND FUNDING SOURCES

Contributors

This work was supported by a dissertation committee consisting of Dr. Prabir Daripa, Dr. Peter Howard, Dr. Peter Kuchment and Dr. Raytcho Lazarov of the Department of Mathematics and Dr. Michael King of the Department of Petroleum Engineering.

All work conducted for the dissertation was completed by the student independently.

Funding Sources

Graduate study was supported in part as a Research Assistant of Dr. Prabir Daripa by the NPRP grant 08-777-1-141 through Qatar National Research Fund (QNRF) and by the U.S. National Science Foundation (NSF) grant DMS-1522782. The contents of this dissertation are solely the responsibility of the author and do not necessarily represent the official views of the QNRF or the NSF. Graduate study was also supported in part as a Teaching Assistant of the Department of Mathematics at TAMU.

NOMENCLATURE

$\mathbf{v}$	Total velocity
$\mathbf{v}_a$	Aqueous phase velocity
$\mathbf{v}_o$	Oleic phase velocity
p	Global pressure
p_a	Aqueous phase pressure
p_o	Oleic phase pressure
p_c	Capillary pressure
p_b	Entry pressure
s	Aqueous phase saturation
c	Polymer concentration in the aqeuous phase
Γ	Surfactant concentration in the aqueous phase
$\mathbf{K}$	Absolute permeability tensor
ϕ	Porosity
μ_w	Viscosity of pure water
μ_a	Viscosity of the aqueous phase
μ_o	Viscosity of the oleic phase
k_{ra}	Relative permeability of the aqueous phase
k_{ro}	Relative permeability of the oleic phase
λ_a	Mobility of the aqueous phase
λ_o	Mobility of the oleic phase
λ	Total Mobility

f_a	Fractional flow function of the aqueous phase
f_o	Fractional flow function of the oleic phase
q_a	Volumetric injection/production rate of the aqueous phase
q_o	Volumetric injection/production rate of the oleic phase
s_{ra}	Residual saturation of the aqueous phase
s_{ro}	Residual saturation of the oleic phase
σ	Interfacial tension (IFT) between the aqueous and the oleic phases
$s_{ra}^{\sigma 0}$	Residual saturation of the aqueous phase at IFT value of $\sigma 0$
$s_{ro}^{\sigma 0}$	Residual saturation of the oleic phase at IFT value of $\sigma 0$
$s_0^{\sigma 0}$	Connate water saturation at IFT value of $\sigma 0$
N_c	Capillary number of the displacement process
N_{co}	Capillary number of the oleic phase at IFT value of $\sigma 0$
N_{ca}	Capillary number of the aqueous phase at IFT value of $\sigma 0$
M_μ	Viscosity ratio
M_λ	Endpoint mobility ratio
M_s	Shock front mobility ratio
EOR	Enhanced Oil Recovery
TAMU	Texas A&M University
L^2	Space of square-Lebesgue-integrable functions, i.e., $\|f\|_2 = \left(\int \|f\|^2\right)^{1/2} < \infty$
L^∞	Space of essentially bounded Lebesgue-measurable functions, i.e., $\|f\|_\infty = \sup \|f\| < \infty$

TABLE OF CONTENTS

Page

LIST OF FIGURES

FIGURE Page

LIST OF TABLES

TABLE Page

1. INTRODUCTION

1.1 Motivation

Porous substances are ubiquitous. Natural objects such as rocks, zeolites, soil, biological tissues such as bones, skin, membranes and wood, and man made materials such as cements and ceramics are some instances of porous materials. The study of fluid flow through porous media is a subject of common interest in many areas of applied science and engineering such as filtration, geomechanics, bio-remediation, construction engineering, hydrogeology, biology and biophysics, material science, etc. Naturally, this has emerged as a separate field of study and it requires an understanding of the interaction between the medium and the fluid that flows through it.

Porous materials are often heterogeneous which means that the properties may vary from one place to another. A fractured rock is an extreme example which consists of a collection of blocks (regions offering high resistance to flow) separated by a network of fractures (regions offering very little resistance to flow). This heterogeneous nature of a porous medium is usually characterized by its *porosity* and *permeability*.

Porosity or void fraction is a measure of the void spaces in a porous material and is defined as the fraction of the void volume over the total volume. It takes a value between 0 and 1. It determines the total volume of fluid that can be contained in a porous medium.

Permeability of a porous material is a measure of its resistance to the flow of fluid. This property depends on various quantities such as the type of the porous medium, the porosity, the shapes of the pores in the medium, the extent of connectivity between the pores and the tortuosity. Here, tortuosity is a measure of how curved (or tortuous) the flow paths are in a porous medium and may be defined as the ratio of the length of a finite curved flow path to the distance between its two ends. Permeability values for different

types of materials can vary over a wide range. For example, permeability values for sandstones lie between 10^{-14}m^2 and 10^{-11}m^2 while those for granite range from 10^{-19}m^2 to 10^{-18}m^2. In anisotropic three dimensional media, permeability is modeled using a second order tensor. The term *absolute permeability* is used to signify the intrinsic property that is exclusively a function of the material structure of the porous medium and not of the fluid. In single-phase flow the absolute permeability is the effective permeability of the porous medium. The range of values stated before are absolute permeability values of sandstone and granite. When multiple fluid phases occupy the pore space, the flow of each phase is inhibited by the presence of the other phases. Hence in multphase flow the *relative permeability* of a phase is used as a multiplicative factor to the absolute permeability resulting in what is known as effective permeability of the medium to that specific phase. The relative permeability of a phase is a dimensionless number that takes a value between 0 and 1.

The study of multiphase flow in porous media is significantly more complicated than the study of single-phase flow due to a number of other physical effects that influence the properties of both the medium as well as the flow. Some of these effects will be discussed in detail in section 1.3. However, such flows are of vital interest to a vast array of physical, environmental and industrial problems at various spatial and temporal scales. These include groundwater flow and soil remediation, reactions in fluidized and fixed beds, filtration, flow in packed beds of catalysts, manufacturing of polymer composites, reservoir engineering to name a few. The understanding and accurate prediction of these flow processes can play an important role in a number of subsurface and technical applications. For example, the flow processes in the unsaturated zone of the subsurface need to be quantified in order to calculate groundwater recharge. Also, the prediction of the flux distribution of water and air helps in the modeling of contaminant transport, such as the displacement of pesticides and heavy metals. This work has been primarily motivated by chemical enhanced oil recovery processes like polymer and surfactant-polymer (SP) flooding. A brief

overview of the relevant oil recovery processes will be presented in the next section.

1.2 Enhanced Oil Recovery (EOR)

Oil recovery is categorized into three phases: primary, secondary and tertiary. At the early stage of development the entire porous medium is effectively filled with a single fluid phase like oil. Upon construction of a set of wells, the resident oil starts to spontaneously flow out due to the internal pressure of the porous medium and this stage rapidly comes to an end when the pressures in the porous medium and the atmosphere reach an equilibrium. This first stage is called *primary recovery* and typically only $5 - 15\%$ of the oil in the reservoir is recovered in this stage [3]. In order to recover part of the remaining oil, the available set of wells is categorized into injection wells and production wells. In this *secondary recovery* stage, the injection wells are used to inject an inexpensive external fluid, such as water or gas, in order to sweep out additional oil towards the production wells. These recovery processes involve the immiscible displacement of a more viscous fluid (oil) by a fluid of lesser viscosity (water or brine) which leads to the formation of undesirable nonlinear viscous fingers of the displacing fluid, thereby reducing the efficiency of the recovery process. Typically, after primary and secondary recovery about $65 - 70\%$ of the oil in the reservoir is still left [3]. In the past, often production used to halt at this stage as economics dictated that finding and producing oil from a new field was cheaper.

Today, however, fossil fuels account for more than 80% of the world's energy and oil is the dominant primary energy source with the consumption forecast to grow rapidly in the next decade. The growing global energy demand, slow rise in renewable energy sector and deep offshore locations of new oil wells are the primary factors that have led to a resurgence in seeking novel ways to either sustain or increase the production of oil from existing wells. This third phase of recovery, termed as *tertiary recovery* or *enhanced oil recovery* (EOR), is characterized by injection of a series of complex fluids, such as chem-

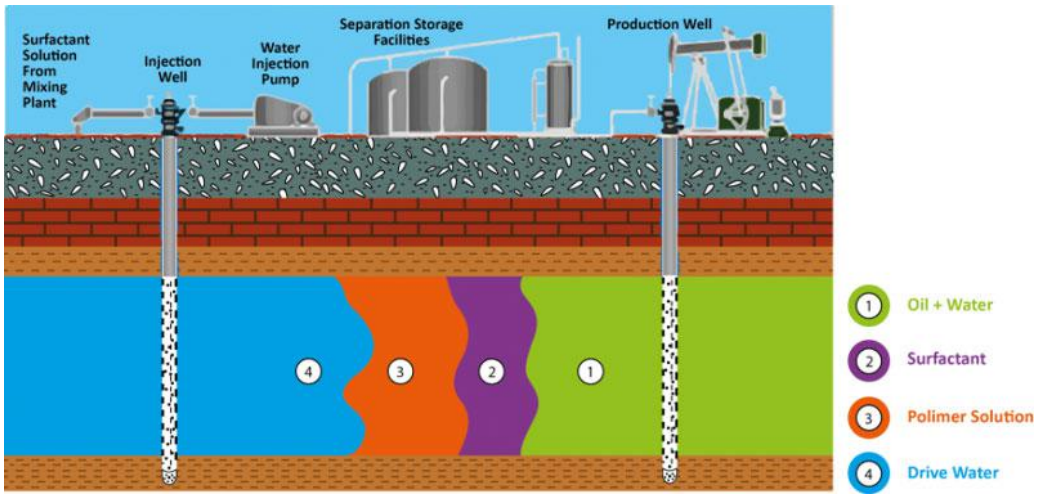

Figure 1.1: Pictorial representation of the schematic of a chemical enhanced oil recovery process using polymer and surfactant.
(Source: http://www.indospec.com/expertise/indospec-chemical-enhanced-oil-recovery/ last accessed 5/15/2017 2:30 PM)

icals, miscible gases, and/or the use of thermal energy. Figure 1.1 shows a schematic of such a tertiary recovery process where approrpiate amounts of chemicals like polymer and surfactant are being used to improve the recovery of oil. This particular type of chemical enhanced oil recovery process will be the focus of much of our study in this dissertation.

One of the effective methods of tertiary oil recovery is Surfactant-Polymer (SP) flooding which involves injection of polymer and surfactant laden aqueous phase in oil reservoirs. Polymer in the displacing fluid improves oil recovery by inhibiting the growth rate of the fingering instability and by increasing the water saturation level behind the displacing front. See Daripa *et al*. [4] for a study of these phenomena during polymer flooding which in general is a less effective method of tertiary oil recovery than SP flooding, one of the processes studied in this dissertation. In SP flooding, the use of surfactant further improves oil recovery by reducing the capillary pressure between the aqueous and the oil phases and by reducing the residual saturation limits of the rock matrix. ASP flooding

in which Alkali is also used in the SP-laden aqueous phase, is sometimes more effective since the alkali reacts with the napthenic acids present in the oil to produce anionic surfactants thereby replenishing the surfactant lost due to adsorption by the porous matrix during the transport of these chemical components through the porous medium. In recent years, surfactant-polymer flooding has been shown to be preferable to even ASP flooding in highly heterogeneous reservoirs as the elimination of alkali removes undesirable inorganic scale formation, incompatibility with some polymers and demulsification difficulties [5, 6]. Therefore, SP flooding is of significant current interest and is drawing a lot of attention [7, 8, 9, 10, 11].

1.3 Modeling Efforts

In theory, the principle of conservation of momentum could be used to describe the motion of a single fluid phase through the porous medium if the spatial distribution of the pores is known. This system of equations would yield the velocity field after enforcing appropriate boundary conditions at the fluid-pore interface. However, the random nature of the pore distribution makes it nearly impossible to obtain a precise description of the pore geometry and of the pore-scale phenomena. Also, in all domains of practical environmental interest, the characteristic size of the pore structure is much smaller than the extent of the total volume of interest. Thus, even if the spatial distribution were known, the computational power needed to accurately resolve the intricate details and multiscale variations in the microstructure makes this problem intractable. Therefore, traditionally the pore-scale description is reduced to a more manageable macro-scale form by averaging inside a *representative elementary volume* (REV). This transforms the discrete microscopic description to a continuous representation which yields macroscopic field variables that describe the observed phenomena [12]. One of the main challenges of this approach is to accurately capture the fine-scale features of the porous medium inside the macro-

scale averaged quantities like the absolute permeability ($\mathbf{K}$) and the porosity (ϕ). In this dissertation, we have adopted this averaged macro-scale model approach.

The basic law governing single-phase flow of fluids through saturated porous media is Darcy's law [12] given by

$$\mathbf{v} = -\frac{\mathbf{K}}{\mu}\boldsymbol{\nabla} p, \tag{1.1}$$

where $\mathbf{v}$ is the volume-averaged fluid velocity also called the Darcy velocity, $\mathbf{K}$ is the absolute permeability tensor, μ is the fluid viscosity and p is the fluid pressure. This law was originally formulated by Henry Darcy in 1856 on the basis of experimental data on vertical water filtration through sand beds and was subsequently derived theoretically [13].

The model problems in this study are SP flooding and polymer flooding which are examples of immiscible, multicomponent, two-phase flow through porous media. Here the oil and the aqueous solution (containing polymer and/or surfactant) are the two fluid phases while polymer and surfactant are the two dissolved components. For the purpose of modeling such flows we have made the following simplifying assumptions.

1. Mass transfers between the fluids are neglected.

2. The flow is isothermal.

3. The solid structure of the porous medium is rigid and does not react with the pore fluids.

4. All the fluids phases are incompressible.

Under the above assumptions, an empirical extension of the single-phase Darcy equation is used to model two-phase flows. The void space is assumed to be filled with the two immiscible fluid phases such that the porous medium is saturated. At the macroscopic

scale, the motion of these fluid phases is captured using the volume fraction occupied by each phase called the *saturation* (s) of that phase. The aqeuous phase contains one or more components and the concentration (volume fraction) of a component i is denoted by c_i. Details of the extension of Darcy's law and the equations governing the evolution of the fluid phases and the dissolved components will be presented in the next chapter. Here we introduce one more fundamental rock-fluid characteristic associated with multiphase flows in porous media known as the *capillary pressure*.

At the pore-scale, immiscible fluids are separated by a well defined interface. This interface is characterized by some surface energy which arises because the cohesive molecular forces between the fluid molecules is different on the two sides of the interface. Moreover, when two fluids occupy the pore space, one of them is preferentially attracted by the surface of the solid matrix due to the different levels of molecular interaction between the solid and the two fluid phases. This preferentially attracted phase is termed as the wetting phase and the other fluid phase is termed as non-wetting. A combination of the effects of this surface energy and the wettability characteristics determines the shape of the interface. The shape of the interface, in turn, determines the contact angle which is used to define capillary pressure p_c at the pore-scale. Intuitively, capillary pressure can be understood as the excess pressure that the non-wetting phase should have to keep the interface steady between two static fluids [14]. This notion allows us to define capillary pressure in terms of the macroscopic field variables by using a static force balance across the interface in the following way

$$p_c = p_{nw} - p_w, \tag{1.2}$$

where p_{nw} and p_w are the pressures in the non-wetting and the wetting fluid phases respectively. In our study, we have considered only hydrophilic porous media which shows

greater affinity to the aqeuous phase than the oleic phase and is also found more commonly in nature.

Based on the above modeling assumptions, multiphase flow in porous media is studied mainly using two different approaches. The first approach is based on mass conservation laws for each of the fluids [15]. In the second approach, known as the fractional flow approach, these conservation laws are combined to obtain a new set of equations with the introduction of the total velocity, the global pressure and other ancillary functions. The fractional flow approach which is computationally more efficient than the two-pressure approach, has been successfully adopted for numerical simulations in hydrology and petroleum reservoir problems and has also been adopted in this dissertation.

The global pressure was introduced by Chavent and Jaffré [16] for immiscible, incompressible two-phase flow without any components and was later revisited by several others (see for instance [17]). Recently the concept of global pressure has been extended to immiscible, compressible two-phase flows under the assumption of no mass transfer between the phases and taking into account the effects of gravity, capillary pressure and heterogeneity [18, 19]. Some existence results for this new formulation have been presented [20] and its effectiveness in numerical simulations has been demonstrated [21]. This has been further extended to a global pressure formulation for the case of compositional, compressible two-phase flows with mass exchange between the phases [22]. A fully equivalent global pressure formulation for three-phase compressible flows has been established [23] and numerically validated [24]. In this dissertation, a global pressure formulation has been formally derived for immiscible, incompressible two-phase flows in the presence of dissolved components (polymer and surfactant) [25]. Unlike the two-phase flow models discussed above, the fractional flow formulation for multicomponent two-phase flow has a system of transport equations for the wetting phase saturation and the component concentrations which are coupled to the global pressure equation.

1.4 Survey of Numerical Methods

The flow and transport equations describing multicomponent, immiscible, two-phase porous media flow form a system of coupled, highly nonlinear partial differential equations. There has been a significant amount of research directed towards the development of numerical methods capable of efficiently and accurately capturing both the overall trends in the reservoir flow pattern as well as the intricate details. Classical finite difference and finite element methods often give rise to nonphysical oscillations in the numerical solution while classical upwind methods tend to generate excessive numerical diffusion that smears out the fronts. To avoid these issues, various high-order accurate *finite difference methods* [4, 26, 27, 28, 29] and locally mass conservative *finite volume methods* [30, 31] have been developed for constructing numerical solutions of these multiphase multicomponent flows through heterogeneous porous media. Different types of *finite element methods*(FE) such as control volume FE (CVFE -[32, 33]), discontinuous Galerkin (DG -[34, 35, 36, 37]) and mixed FE [38, 39] methods have also become methods of choice for the reservoir simulation because these methods do not suffer from much grid orientation effects, allow local grid refinement and have high order of accuracy. These methods are also versatile and have been applied to other problems such as simulation of faults and fractures [40, 41, 42]. In the recent past, several multiscale FE and FV methods have also been proposed to better account for the variation in the reservoir properties over a large range of computational scales [43, 44, 45]. In problems where advection dominates diffusion, finite element methods have been found to exhibit excessive nonphysical oscillations for non-smooth solutions [46]. When standard upstream weighting approaches are applied to these FE methods to eliminate the nonphysical oscillations, they tend to smear out sharp fronts and suffer from grid orientation problems. While extremely fine mesh refinement can alleviate some of these problems, it has prohibitively high computational expense.

An alternative approach to solve time dependent advection-diffusion problems is given by the class of Eulerian-Lagrangian methods. For instance, the *particle-in-cell* methods [47, 48, 49, 50, 51] have been succesfully applied to the numerical study of plasma physics, dense particle flows and other problems in computational fluid dynamics and fall in this class of methods. When methods in this class are applied in the context of advection-diffusion problems, the advection part is treated in Lagrangian coordinates by propagating the solution along the characteristics for the advection part, while a Eulerian fixed mesh is used for the diffusion part. As the solutions of the advection diffusion PDEs are much smoother along the characteristics than they are in the time direction, these methods usually allow larger time steps to be used in a numerical simulation while still maintaining its stability and accuracy. Also, these methods significantly reduce numerical diffusion and grid-orientation effects observed in upwind schemes, and are very competitive in terms of accuracy and efficiency [52, 53, 54].

The Modified Method Of Characteristics (MMOC) is one of the earliest methods (see [55]) in the class of Eulerian-Lagrangian methods to be widely accepted for numerical simulation of miscible and immiscible displacement problems [56]. Some of the significant subsequent improvements on this method include the modified method of characteristics with adjusted advection (MMOCAA, [52, 57]), the Eulerian-Lagrangian localized adjoint method (ELLAM, [58]), the characteristic mixed finite element method (CMFEM, [59]), the locally conservative Eulerian-Lagrangian method (LCELM, [60]), the characteristic finite volume element method (CFVEM, [61]) and the Eulerian-Lagrangian discontinuous Galerkin method (ELDG, [62]). The MMOCAA is a mass-conserving time discretization procedure which inherits the competitiveness of the MMOC. The conservative modified method of characteristics (CMMOC, [63]) is a variant of the MMOCAA which adjusts the convection implicitly and minimizes the error of the mass balance problem. The ELLAM and CMFEM are some of the other variants of the characteristics based method which also

conserve mass.

Previously, the MMOC and its variants had only been studied in the context of miscible and immiscible, purely two-phase flow problems that lead to a system of coupled equations for solving one of the phase saturations and one of the phase pressures. In this dissertation, the MMOC approach has been applied to solve the system of transport equations arising in the context of multicomponent two-phase flows with one phase saturation and two component concentrations as the primary transport variables [25]. Towards this end, it is worth mentioning here that the front tracking method has been applied to solve a similar system as ours but of less complexity when the surfactant is not present and the effect of capillary pressure is neglected. We direct the readers to Daripa *et al*. [27] and the papers cited therein.

Error estimates and convergence analysis have been carried out previously for the MMOC [55], the MMOCAA [60], the CMFEM [59], the ELLAM [64] and the ELDG [62] methods in the context of miscible flows and immiscible purely two-phase flows without components. In most of these estimates the generic constants are inversely dependent on the vanishing parameter ϵ (coefficient of the diffusion term) and cause difficulties when ϵ approaches 0. The uniformly optimal-order convergence rates that are observed numerically for Eulerian-Lagrangian methods are often not reflected in these estimates. Some, ϵ-uniform estimates for the advection diffusion equations with diffusion of the form $\epsilon D(x,t)$ and with periodic and flux boundary conditions were obtained for the MMOC, the MMOCAA, the ELLAM and the ELDG schemes (see [62] and references therein). Although all of these estimates are ϵ-independent, they depend strongly on the lower and the upper bounds of the diffusion coefficient $D(x,t)$.

We have also performed a convergence analysis of the hybrid numerical method [65]. For the complete analysis of the flow and transport system, we have assumed an optimal order estimate for the L^∞ norm of the pressure gradient obtained by solving the global

pressure equation using the discontinuous finite element method. This estimate has been used to study the convergence behavior of the MMOC method for the system of transport equations. For the analysis of the transport system, we have considered a reduced system of equations in one spatial dimension involving only one component (polymer). This reduced system models chemical EOR by polymer flooding in one-dimension as opposed to polymer flooding in two-dimensions [66, 67]. Previous works [55, 68] on the convergence analysis of the MMOC-based methods have been without components and the present work builds on that work by adding a component which complicates the analysis in a significant way. This is due to the coupling of the coefficients involved in the transport equations, as will be abundantly clear from the analysis to be presented in this dissertation. As will be discussed, the convergence analysis presented here can be extended to the original problem involving two components and in two-dimensions.

The analysis involves estimation of errors introduced by the finite difference discretization of the derivatives, by the linear interpolation to compute solutions at points where the characteristic curves intersect the computational grid and by the linearization of the coefficients. These coefficient functions in the two transport equations depend on both the wetting phase saturation and the component concentration. This coupling creates an additional challenge for the analysis of the multicomponent system. The finite difference discretization errors have been estimated using multivariable Taylor Series. The errors due to the linear interpolation have been estimated using the Peano kernel theorem [55] and the errors due to quasi-linear approximation of the nonlinear coefficients have been estimated using various inequalities including the Cauchy-Schwarz and generalized arithmetic mean-geometric mean (AM-GM) inequalities. The transport equations have been tested against the error variables and some of the resulting inner products were replaced by the estimates mentioned above. The transport equations have then been rewritten in forms that allow us to estimate the discrete L^2 errors in the aqueous phase saturation and

the component concentration. Taking into account the time discretization, finally a discrete Gronwall type inequality has been used to obtain the desired estimates. For the purpose of validating the error estimates obtained from the analysis, we have carried out numerical simulations of polymer flooding (single component two-phase flow) and have computed L^2 and L^∞ error norms for the numerical solutions.

In summary, we have proposed a model that describes the displacement processes during the SP flooding process in the form of a new global pressure formulation. The model has been numerically solved using a hybrid methodology that uses a non-traditional discontinuous finite element method for the global pressure, in combination with the modified method of characteristics (MMOC) and time implicit methods to solve the system of the advection-diffusion equations for the phase saturations and the concentrations of various chemical components. A convergence analysis of the MMOC procedure for the system of transport equations has been performed to obtain error estimates for the numerical solution. These error estimates have been numerically validated using an exact solution. To further validate and demonstrate the accuracy and performance of the method, we have used numerical simulations of two-phase flow, both with and without a component, in different heterogeneous permeability fields and flow geometries. Then, results from numerical simulation studies comparing various flooding schemes for multicomponent flows like SP flooding in heterogeneous permeability fields have been presented.

This dissertation is laid out as follows. In chapter 2, the global pressure formulation of the governing equations for polymer flooding and SP flooding are derived and presented along with the various constitutive relations. These include relevant models of capillary pressure and relative permeability and their dependence on the water saturation and the concentrations of the polymer and the surfactant. In chapter 3, we present the numerical method by giving a detailed description of the computational grids, the non-traditional discontinuous finite element method for the pressure equation and the MMOC for the

transport equations of SP flooding. A concise computational algorithm is also presented along with a pseudocode and a flowchart. Moreover, details of the convergence analysis of the hybrid method is also presented in chapter 3. We present and discuss the numerical results in chapter 4. These include quantitative validation using an exact solution and various qualitative validation studies by comparing with results from existing literature. Details on the construction of multiscale heterogeneity fields suitable for testing the robustness of the method are also provided. Moreover, a brief sketch of a novel technique to test the severity of grid orientation effects is provided.

2. MATHEMATICAL MODEL*

2.1 Polymer Flood

Polymer flooding is one of the popular methods of Enhanced Oil Recovery (EOR) that has been in use for decades and has also been fairly successful, especially in China [69]. Such a tertiary recovery process consists of injecting an aqueous phase containing a water-soluble polymer into the porous medium (possibly after the reservoir has been preflooded with pure water during the secondary recovery process). This process is depicted in Fig. 2.1. The polymer-thickened aqueous phase is more viscous than pure water.

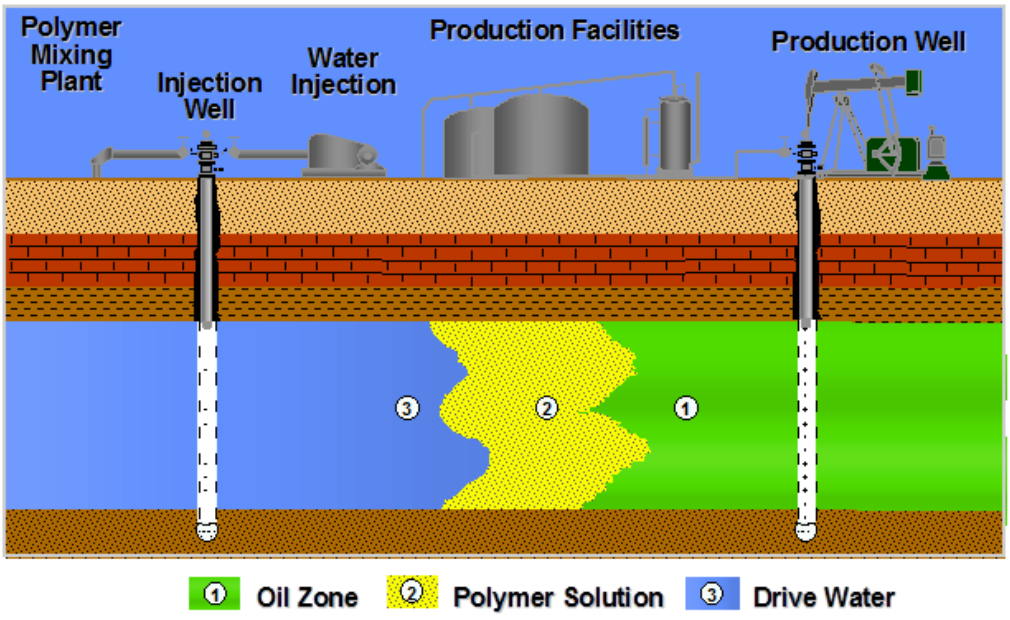

Figure 2.1: Schematic of polymer-flooding process (Source: http://tupeg.ir/polymer-waterflooding/, last accessed 04/11/2017 5:00 PM)

*Part of this chapter is reprinted from Journal of Computational Physics, 335, Prabir Daripa and Sourav Dutta, "Modeling and simulation of surfactant-polymer flooding using a new hybrid method", 249-282, doi: 10.1016/j.jcp.2017.01.038, Copyright (2017) with permission from Elsevier.

Additionally, some polymers decrease the aqueous phase relative permeability. The combination of these two effects result in a reduction of the mobility (permeability/viscosity) of the aqueous phase. This leads to a reduction in the mobility ratio between the injected aqueous phase and the resident oil phase, which in turn increases the efficiency of the flooding process due to two different mechanisms. Firstly, it stabilizes the oil-water interface and partially inhibits the growth of unwanted finger patterns, thus achieving a greater volumetric sweep efficiency. Secondly, it leads to a lower swept-zone oil saturation or in other words an increase of the saturation level behind the polymer treated aqueous bank.

In our study, we have assumed that polymer is solely used to control the viscosity of the injected aqueous phase. The permeability reduction effect is usually less important than the increase in viscosity [14] and hence has been neglected in our model. Below, we will build our model from the fundamental principles of physics and as a natural extension of the problem studied by Daripa *et al*. [70].

Let $\Omega \subset \mathbb{R}^2$ represent a porous medium with boundary $\partial\Omega$. The incompressible and immiscible flow of the wetting phase (water or an aqueous solution of polymer and/or surfactant) and the non-wetting phase (oil) is described by a combination of the multiphase extension of Darcy's law (see [71]) for each phase and transport equations for each component. Let s_j denote the saturation (volume fraction), $\mathbf{v}_j$ denote the velocity, p_j denote the phase pressure and q_j denote the volumetric injection/production rate of phase j where $j = o$ and $j = a$ denote the non-wetting and the wetting phases respectively. The conservation of mass of each fluid phase gives rise to the following transport equations [25]

$$\phi \frac{\partial s_a}{\partial t} + \boldsymbol{\nabla} \cdot \mathbf{v}_a = q_a, \quad (\mathbf{x}, t) \in \Omega \times (0, T], \tag{2.1a}$$

$$\phi \frac{\partial s_o}{\partial t} + \boldsymbol{\nabla} \cdot \mathbf{v}_o = q_o, \quad (\mathbf{x}, t) \in \Omega \times (0, T]. \tag{2.1b}$$

The equation for conservation of mass of the polymer dissolved in the aqueous phase is given by

$$\phi\frac{\partial(cs_a)}{\partial t} + \boldsymbol{\nabla}\cdot(c\mathbf{v}_a) = c^i q_a \delta(\mathbf{x}-\mathbf{x}^i) + cq_a\delta(\mathbf{x}-\mathbf{x}^p), \quad (\mathbf{x},t)\in\Omega\times(0,T], \tag{2.2}$$

where c is the concentration (volume fraction in the aqueous phase) of the dissolved polymer while c^i is the concentration of polymer in the injected fluid. It is assumed that the polymer is getting only passively advected with negligible diffusion and no adsorption losses. Also, $\mathbf{x}^i$ is the location of the injection well and $\mathbf{x}^p$ is the location of the production well, both of which are treated as point source/sink terms and δ is the Dirac-delta function. The conservation of momentum is given by the Darcy-Muskat law for each phase

$$\mathbf{v}_a = -\mathbf{K}(\mathbf{x})\lambda_a\boldsymbol{\nabla}p_a, \quad \mathbf{x}\in\Omega, \tag{2.3a}$$

$$\mathbf{v}_o = -\mathbf{K}(\mathbf{x})\lambda_o\boldsymbol{\nabla}p_o, \quad \mathbf{x}\in\Omega. \tag{2.3b}$$

Here ϕ is the porosity (taken to be constant in the numerical experiments in this study), $\mathbf{K}(\mathbf{x})$ is the absolute permeability tensor of the porous medium, $\lambda = \lambda_a(s_a,c) + \lambda_o(s_a,c)$ is the total mobility and $\lambda_j = k_{rj}/\mu_j$ is the phase mobility where k_{rj} is the relative permeability and μ_j is the viscosity of phase j. In addition to the above, the capillary pressure (p_c) is defined by

$$p_c = p_o - p_a. \tag{2.4}$$

Since the porous medium is initially saturated with the two phases, we have

$$\sum_{j=o,a} s_j = 1. \tag{2.5}$$

Henceforth we will use the notation s for s_a. In [70], Daripa *et al*. studied the polymer flooding problem using a model that combines the conservation laws described above in eqs. (2.1a), (2.1b), (2.2), (2.3a) and (2.3b) and assumes the capillary pressure given in eq. (2.4) to be zero. The resulting system of equations is recalled below.

$$\frac{\partial s}{\partial t} + \boldsymbol{\nabla} \cdot (\mathbf{v} f_a(s,c)) = \text{ source terms}, \tag{2.6a}$$

$$\frac{\partial (sc)}{\partial t} + \boldsymbol{\nabla} \cdot (\mathbf{v} c f_a(s,c)) = \text{ source terms}, \tag{2.6b}$$

$$\boldsymbol{\nabla} \cdot \mathbf{v} \equiv \boldsymbol{\nabla} \cdot (-\lambda(s,c)\boldsymbol{\nabla} p) = \text{ source terms}, \tag{2.6c}$$

Here $\mathbf{v} = \mathbf{v}_a + \mathbf{v}_o$ denotes the total velocity, $p = p_a = p_o$ denotes the pressure and f_a denotes the fractional flow function of the aqueous phase which relates the aqueous phase velocity $\mathbf{v}_a$ to the total velocity $\mathbf{v}$. Also, in the above system of equations (2.6a) - (2.6c) the reservoir is assumed to be homogeneous ($\mathbf{K} = I$) with a constant porosity, but some of the reported numerical simulations were carried out in a heterogeneous reservoir. The phase mobilities were defined as follows

$$\lambda_a(s,c) = \frac{k_{ra}(s)}{\mu_a(c)} = \frac{s^2}{\mu_a(c)}, \qquad \lambda_o(s) = \frac{k_{ro}(s)}{\mu_o} = \frac{(1-s)^2}{\mu_o}. \tag{2.7}$$

The effect of polymer was incorporated into the system by assuming that the aqueous phase viscosity depends linearly on the polymer concentration as given below.

$$\mu_a = \mu_w(1 + \beta c), \tag{2.8}$$

where μ_w denotes the pure water viscosity and β is a parameter that characterizes the particular polymer used.

The nonlinear system of equations given by (2.6a) - (2.6c) is coupled because the

solution of the elliptic pressure equation (2.6c) depends on s and c through the coefficient $\lambda(s, c)$ while the transport equations given by (2.6a) and (2.6b) depend on the total velocity $\mathbf{v}$ that is obtained by solving the pressure equation. However, with $\beta = 0$ the polymer particles are simply advected passively with the background water flow without affecting the overall flow. The transport equations given by eqs. (2.6a) and (2.6b) form a hyperbolic system of conservation laws that can develop discontinuities in finite time from smooth initial data (see [70]). The accurate prediction of the formation and evolution of such types of discontinuous solutions requires a study of the wave structure of the system of hyperbolic equations. In [70], this coupled system of equations was numerically solved using a front tracking algorithm [72, 66, 73] that requires the solution of the Riemann Problem for the hyperbolic system given by eqs. (2.6a) and (2.6b) in order to advance the tracked discontinuities in the solution. The front tracking algorithm allows for a high resolution in the computation of discontinuous solutions of the hyperbolic system with little or no numerical dispersion even on relatively coarse grids. However, this process requires an elaborate and delicate computation to track the propagation of the discontinuity in the solution which becomes progressively more expensive as the system of transport equations becomes more complex.

In our study, we included the capillary effects in the model. The combination of eqs. (2.1a), (2.1b), (2.2), (2.3a), (2.3b), (2.4) and (2.5) produces a new system of strongly coupled nonlinear equations and we will briefly present the derivation here.

Consider the following identity

$$\mathbf{v}_a = \frac{\lambda_o}{\lambda}\mathbf{v}_a - \frac{\lambda_a}{\lambda}\mathbf{v}_o + \frac{\lambda_a}{\lambda}\mathbf{v}. \tag{2.9}$$

Substituting eq. (2.9) in both eq. (2.1a) and eq. (2.2) and then using eq. (2.3a) and eq. (2.3b),

we obtain

$$\phi\frac{\partial s}{\partial t} - \boldsymbol{\nabla}\cdot\left\{\mathbf{K}(\mathbf{x})\frac{\lambda_o}{\lambda}\lambda_a\boldsymbol{\nabla}p_a - \mathbf{K}(\mathbf{x})\frac{\lambda_a}{\lambda}\lambda_o\nabla p_o\right\} + \boldsymbol{\nabla}\cdot\left\{\frac{\lambda_a}{\lambda}\mathbf{v}\right\} = q_a,$$
$$\phi\frac{\partial (sc)}{\partial t} - \boldsymbol{\nabla}\cdot\left\{c\mathbf{K}(\mathbf{x})\frac{\lambda_o}{\lambda}\lambda_a\boldsymbol{\nabla}p_a - c\mathbf{K}(\mathbf{x})\frac{\lambda_a}{\lambda}\lambda_o\nabla p_o\right\} + \boldsymbol{\nabla}\cdot\left\{c\frac{\lambda_a}{\lambda}\mathbf{v}\right\}$$
$$= c^i q_a\delta(\mathbf{x}-\mathbf{x}^i) + cq_a\delta(\mathbf{x}-\mathbf{x}^p).$$

Applying eq. (2.4), the above equations are rewritten as,

$$\phi\frac{\partial s}{\partial t} + \boldsymbol{\nabla}\cdot\{\mathbf{K}(\mathbf{x})f_a(s,c)\lambda_o\boldsymbol{\nabla}p_c(s)\} + \boldsymbol{\nabla}\cdot(f_a(s,c)\,\mathbf{v}) = q_a, \tag{2.10a}$$
$$\phi\frac{\partial (sc)}{\partial t} + \boldsymbol{\nabla}\cdot\{c\mathbf{K}(\mathbf{x})f_a(s,c)\lambda_o\boldsymbol{\nabla}p_c(s)\} + \boldsymbol{\nabla}\cdot(cf_a(s,c)\mathbf{v})$$
$$= c^i q_a\delta(\mathbf{x}-\mathbf{x}^i) + cq_a\delta(\mathbf{x}-\mathbf{x}^p). \tag{2.10b}$$

Equations (2.10a) and (2.10b) are the aqueous phase and the polymer transport equations, respectively, written in the conservative form. Adding eqs. (2.1a) and (2.1b) we obtain,

$$\boldsymbol{\nabla}\cdot(\mathbf{v}_a + \mathbf{v}_o) = q_a + q_o.$$

Substituting eqs. (2.3a) and (2.3b) in the above equation and then using eq. (2.4), we obtain the equation governing the evolution of the aqueous phase pressure as

$$-\boldsymbol{\nabla}\cdot(\mathbf{K}(\mathbf{x})\lambda\boldsymbol{\nabla}p_a) - \boldsymbol{\nabla}\cdot(\mathbf{K}(\mathbf{x})\lambda_o\boldsymbol{\nabla}p_c) = q_a + q_o. \tag{2.11}$$

Combining eqs. (2.10a), (2.10b) and (2.11) we obtain the following system of flow and

transport equations for polymer flooding in phase pressure formulation.

$$\phi\frac{\partial s}{\partial t} + \boldsymbol{\nabla}\cdot(f_a\mathbf{v}) + \boldsymbol{\nabla}\cdot(\boldsymbol{D}_p\,\boldsymbol{\nabla}s) = q_a, \tag{2.12a}$$

$$\phi\frac{\partial (cs)}{\partial t} + \boldsymbol{\nabla}\cdot(c\,f_a\mathbf{v}) + \boldsymbol{\nabla}\cdot(c\,\boldsymbol{D}_p\,\boldsymbol{\nabla}s) = c^i q_a\delta(\mathbf{x}-\mathbf{x}^i) + cq_a\delta(\mathbf{x}-\mathbf{x}^p), \tag{2.12b}$$

$$-\boldsymbol{\nabla}\cdot(\mathbf{K}(\mathbf{x})\lambda\boldsymbol{\nabla}p_a) - \boldsymbol{\nabla}\cdot(\mathbf{K}(\mathbf{x})\lambda_o\boldsymbol{\nabla}p_c) = q_a + q_o. \tag{2.12c}$$

Here $\boldsymbol{D}_p(s,c) = \mathbf{K}(\mathbf{x})\lambda_o(s)f_a(s,c)\frac{dp_c}{ds}$. In the above system, due to the inclusion of the capillary pressure, the elliptic pressure equation given by eq. (2.12c) loses the canonical form of the model without capillary pressure as seen in eq. (2.6c). Moreover, if the aqueous phase pressure p_a (or p_o) is chosen as one of the primary simulation variables, then the system becomes potentially degenerate at all the spatial points in the domain where the aqueous (or respectively oil) phase is absent. In order to avoid these difficulties, we reformulated the problem by using a fictitious pressure p, to be called the global pressure below, for incompressible, immiscible two-phase flows with a single component (see [25]).

The global pressure function p is defined as

$$\begin{aligned} p =& \frac{1}{2}(p_o + p_a) + \frac{1}{2}\int_{s_c}^{s}\left(f_o(\zeta,c) - f_a(\zeta,c)\right)\frac{dp_c}{d\zeta}(\zeta)d\zeta \\ & - \frac{1}{2}\int\left(\int_{s_c}^{s}\frac{\partial}{\partial c}\left(f_o(\zeta,c) - f_a(\zeta,c)\right)\frac{dp_c}{d\zeta}(\zeta)\,d\zeta\right)dc + C, \end{aligned} \tag{2.13}$$

where $f_j = \lambda_j/\lambda$ for $j = a$ and $j = o$ are the aqueous and the oil phase fractional flow functions, respectively. Also, C is an appropriate reference pressure that serves as an integration constant and s_c is the value of the aqueous phase saturation for which $p_c(s_c) = 0$. Usually $p_c = 0$ when the wetting phase is at its maximum saturation or equivalently when the non-wetting phase is at its minimum possible saturation (i.e. residual saturation). Hence, in case of water (or an aqueous solution) displacing oil, $s_c = 1 - s_{ro}$ where s_{ro}

(resp. s_{ra}) is the residual saturation of the oil phase (resp. aqueous phase). Thus, the global pressure is well defined for $s \in [s_{ra}, 1 - s_{ro}]$.

Taking gradients on both sides of eq. (2.13) and simplifying we obtain

$$\boldsymbol{\nabla} p = \frac{1}{2}\boldsymbol{\nabla}(p_o + p_a) + \frac{1}{2}\left(f_o - f_a\right)(s, c)\boldsymbol{\nabla} p_c(s). \tag{2.14}$$

In the absence of the polymer, eq. (2.13) reduces to the global pressure function for incompressible, immiscible two-phase flows (see [16]). Multiplying both sides of eq. (2.14) with $\mathbf{K}(\mathbf{x})\lambda$ and after further manipulation using eqs. (2.3a) and (2.3b) we get

$$-\mathbf{K}(\mathbf{x})\lambda\boldsymbol{\nabla} p = \mathbf{v}. \tag{2.15}$$

Due to the assumption of incompressibility eqs. (2.1a) and (2.1b) can be combined to obtain,

$$\boldsymbol{\nabla} \cdot \mathbf{v} = q_a + q_o. \tag{2.16}$$

Using eq. (2.15) in eq. (2.16) we finally get,

$$-\boldsymbol{\nabla} \cdot (\mathbf{K}(\mathbf{x})\lambda(s, c)\boldsymbol{\nabla} p) = q_a + q_o. \tag{2.17}$$

Equation (2.17) is the global pressure equation for the polymer flood problem. Solving this equation (see below) yields the global pressure p from which the phase pressures p_a and p_o are easily recovered using the definition (2.4) for the capillary pressure and the definition (2.13) for the global pressure. In this formal derivation of the global pressure variable, we have only assumed the following physically realistic functional dependencies, $f_a = f_a(s, c)$, $f_o = f_o(s, c)$ and $p_c = p_c(s)$ and not specific functional forms. However, a similar procedure can be adopted to derive a more general form of global pressure for

any multicomponent two-phase flow system. A specific example of a global pressure function for the two-component two-phase flow system representing SP flooding has been introduced in [25] and will be discussed in Section 2.2.

Using eqs. (2.10a), (2.10b) and (2.17) an equivalent formulation of the polymer flooding problem is obtained in terms of the primary variables (p, s, c) which is written in the non-conservative form as

$$\phi\frac{\partial s}{\partial t} + \frac{\partial f}{\partial s}\mathbf{v}\cdot\boldsymbol{\nabla} s + \boldsymbol{\nabla}\cdot(\boldsymbol{D}_p\boldsymbol{\nabla} s) = G_s - \frac{\partial f}{\partial c}\mathbf{v}\cdot\boldsymbol{\nabla} c, \qquad \mathbf{x}\in\Omega,\ t\in(0,T], \tag{2.18a}$$

$$\phi\frac{\partial c}{\partial t} + \left(\frac{f}{s}\mathbf{v} + \frac{\boldsymbol{D}_p}{s}\boldsymbol{\nabla} s\right)\cdot\boldsymbol{\nabla} c = G_c, \qquad \mathbf{x}\in\Omega,\ t\in(0,T], \tag{2.18b}$$

$$-\boldsymbol{\nabla}\cdot(\mathbf{K}(\mathbf{x})\lambda\boldsymbol{\nabla} p) = q_a + q_o, \qquad \mathbf{x}\in\Omega,\ t\in(0,T], \tag{2.18c}$$

where $\boldsymbol{D}_p(s,c) = \mathbf{K}(\mathbf{x})\lambda_o(s)f(s,c)\frac{dp_c(s)}{ds}$ and $q_a + q_o$ is an appropriate source term for the pressure equation which is modeled by a finite number of point sources and sinks located at isolated points $\mathbf{x}^i$ and $\mathbf{x}^p$ respectively so that $q_a + q_o = \Sigma_{k=\{i,p\}} q^k\delta(\mathbf{x}-\mathbf{x}^k)$. Also, $G_s = (1-f)Q\delta(\mathbf{x}-\mathbf{x}^i)$ and $G_c = (c^i - c)\frac{Q}{s}\delta(\mathbf{x}-\mathbf{x}^i)$ are the source terms for the transport equations where Q is the total volumetric flux at the injection/production points.

The transport equations given by eqs. (2.18a) and (2.18b), written in the non-conservative form, are equivalent to the transport eqs. (2.12a) and (2.12b) which are in the conservative form. The principal advantage of this new formulation is that even with the introduction of the capillary pressure in the model, the global pressure equation given by eq. (2.18c) retains the canonical form of the pressure eq. (2.6c), where the model ignores capillary pressure. As opposed to the pressure eq. (2.12c) in the phase pressure formulation, the simplified canonical form in eq. (2.18c) is more amenable to mathematical and numerical analysis and makes the development of computational algorithms easier.

We also make following practical and physical assumptions to define the source terms

in eqs. (2.1a) and (2.1b),

$$(q_a, q_o) = \begin{cases} (Q, 0) \\ \left(-\dfrac{\lambda_a}{\lambda}\, Q, -\dfrac{\lambda_o}{\lambda}\, Q\right) \\ (0, 0) \end{cases}; \quad \text{at } \mathbf{x} = \begin{cases} \mathbf{x}^i & \text{(Source)} \\ \mathbf{x}^p & \text{(Sink)} \\ \mathbf{x} \in \Omega \setminus \{\mathbf{x}^i \cup \mathbf{x}^p\} & \text{(Elsewhere)} \end{cases}, \tag{2.19}$$

which mean that oil is never injected and the fluid mixture obtained at the production well is proportional to the resident fluid at the point. The following initial and boundary conditions are prescribed.

$$\forall \mathbf{x} \in \Omega : \qquad s(\mathbf{x}, 0) = s_0(\mathbf{x}) \quad \& \quad c(\mathbf{x}, 0) = c_0(\mathbf{x}), \tag{2.20a}$$

$$\forall (\mathbf{x}, t) \in \partial\Omega \times (0, T] : \quad \boldsymbol{\nabla} s \cdot \hat{\mathbf{n}} = 0, \quad \boldsymbol{\nabla} c \cdot \hat{\mathbf{n}} = 0 \quad \& \quad \mathbf{v}_j \cdot \hat{\mathbf{n}} = 0 \, (j = a, o), \tag{2.20b}$$

where $\hat{\mathbf{n}}$ denotes the outward unit normal to $\partial\Omega$. The polymer flooding model given by eqs. (2.18a)–(2.18c) is completed by constitutive relations for aqueous phase viscosity, relative permeabilities and capillary pressure. The viscosity model of [70] given by eq. (2.8) is also adopted in our study. Several models of relative permeability, k_{rj} and capillary pressure are available in the literature (see [74, 75]). For the numerical simulations of polymer flooding presented in this study, we use the following modified van Genuchten model proposed by Parker *et al*. ([76]),

$$k_{ra}(s) = s_e^{1/2} \left(1 - (1 - s_e^{1/m})^m\right)^2, \tag{2.21a}$$

$$k_{ro}(s) = (1 - s_e)^{1/2} \left(1 - s_e^{1/m}\right)^{2m}, \tag{2.21b}$$

$$p_c(s) = \frac{1}{\alpha_0} \left(s_e^{-1/m} - 1\right)^{1-m}, \tag{2.21c}$$

where $s_e = (s - s_{ra})/(1 - s_{ra})$ is the effective saturation. The values of the parameters m and α_0 in the above model are known to depend on the interfacial tension, $\sigma 0$ between the non-wetting and the wetting phases. In our study below we take $m = 2/3$ and $\alpha_0 = 0.125$ (see [77]). Alternatively Corey-type imbibition relations can also be used (see [78, 74]).

$$k_{ra} = \left(\frac{s - s_{ra}^{\sigma 0}}{1 - s_{ro}^{\sigma 0} - s_{ra}^{\sigma 0}} \right)^{\frac{2+3\theta}{\theta}}, \tag{2.22a}$$

$$k_{ro} = \left(1 - \frac{s - s_{ra}^{\sigma 0}}{1 - s_{ra}^{\sigma 0} - s_{ro}^{\sigma 0}} \right)^2 \left[1 - \left(\frac{s - s_{ra}^{\sigma 0}}{1 - s_{ra}^{\sigma 0} - s_{ro}^{\sigma 0}} \right)^{\frac{2+\theta}{\theta}} \right], \tag{2.22b}$$

$$p_c = p_d \left(\frac{s - s_{ra}^{\sigma 0}}{1 - s_{ro}^{\sigma 0} - s_{ra}^{\sigma 0}} \right)^{-0.25}, \tag{2.22c}$$

where $\theta = 2$ has been used in our study. Also, $s_{ra}^{\sigma 0}$ and $s_{ro}^{\sigma 0}$ are the residual saturations of the aqueous phase and the oleic phase respectively when the interfacial tension between the two phases is given by $\sigma 0$, which is constant in polymer flooding. Also, p_d is the displacement pressure or entry pressure, defined as $\omega_2 \, \sigma 0 (\phi/K)^{1/2}$ where ω_2 is a proportionality constant and K is the geometric mean of the horizontal permeabilities in the x and y directions. As discussed later in the context of SP flooding (see eq. (2.29)), the interfacial tension σ which depends on the surfactant concentration may vary and the entry pressure is used to capture the relationship between the capillary pressure and the interfacial tension. The exponents used in eqs. (2.22a)–(2.22c) are usually determined by fitting curves to equilibrium experimental data. Numerical simulations of polymer flooding were also performed using the Corey-type constitutive relations and the results were found to be qualitatively similar to the results obtained with the van Genuchten model.

2.2 Surfactant-Polymer Flood

SP flooding is the process where the reservoir is flooded with the SP laden aqueous solution to displace the resident oil. This can achieve a higher level of oil recovery than the

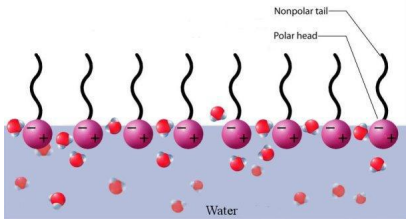

(a) Surfactant molecules arranged on an interface

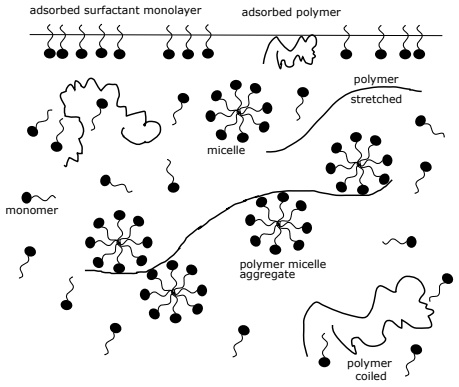

(b) Dynamics of a surfactant polymer solution

Figure 2.2: Pictorial representation of the rheology and behavior of surfactant molecules (a) near an interface and (b) in a solution containing dissolved polymer. (Source of (a): https://commons.wikimedia.org/wiki/File:Surfactant.jpg, last accessed 07/20/2017 6:00 PM)

polymer flood and become more economical if an appropriate combination of surfactant and polymer is used. Surfactants have at least one hydrophobic group (non-polar tail) and one hydrophilic group (polar head) in the same molecule, as shown in Figure 2.2(a). This dual character allows them to sufficiently lower the interfacial tension and also remarkably alter the wetting properties. These factors contribute towards lowering the capillary pressure barrier and increasing the relative permeability of the rock, thereby improving oil recovery. However, the dual character of the surfactant molecule also causes the spontaneous formation of clusters known as micelles. These micelles may interact with the polymer chains to form more complicated aggregates. Depending on the pH level of the system, the polymer can sometimes be lost due to adsorption on the rock surface. Moreover, the thin capillary structure of the rock pores causes the polymer chains to stretch or coil, thus changing the nature of the SP laden aqueous phase. Some of these effects are illustrated in Figure 2.2(b). For the purpose of the current work, some simplifying as-

sumptions have been made that enable us to study the impact of the components (polymer and surfactant) on the aqueous phase viscosity, relative permeability, interfacial tension and capillary pressure.

SP flooding is modeled here as an incompressible, immiscible, multicomponent two-phase flow through porous media. The equation for the conservation of mass of the surfactant dissolved in the aqueous phase is given by

$$\phi\frac{\partial(\Gamma s_a)}{\partial t} + \boldsymbol{\nabla}\cdot(\Gamma\mathbf{v}_a) = \Gamma^i q_a\delta(\mathbf{x}-\mathbf{x}^i) + \Gamma q_a\delta(\mathbf{x}-\mathbf{x}^p), \quad (\mathbf{x},t)\in\Omega\times(0,T], \quad (2.23)$$

where Γ is the concentration of the surfactant in the aqueous phase and Γ^i is the concentration of the surfactant in the injected fluid.

The following initial and boundary conditions are prescribed.

$$s(\mathbf{x}) = s_0(\mathbf{x}), \quad c(\mathbf{x}) = c_0(\mathbf{x}), \quad \Gamma(\mathbf{x}) = \Gamma_0(\mathbf{x}); \quad \mathbf{x}\in\Omega, \quad t=0, \qquad (2.24a)$$

$$\boldsymbol{\nabla}s\cdot\hat{\mathbf{n}} = 0,\ \boldsymbol{\nabla}c\cdot\hat{\mathbf{n}} = 0,\ \boldsymbol{\nabla}\Gamma\cdot\hat{\mathbf{n}} = 0\ \&\ \mathbf{v}_j\cdot\hat{\mathbf{n}} = 0; \qquad \mathbf{x}\in\partial\Omega,\ t>0,\ (j=a,o), \qquad (2.24b)$$

where $\hat{\mathbf{n}}$ is a unit vector normal to $\partial\Omega$.

The combination of eqs. (2.1a), (2.1b), (2.2), (2.3a), (2.3b), (2.4) and (2.23) can be used to describe the SP flooding problem in the phase pressure formulation similar to eqs. (2.12a)–(2.12c), which is a system of strongly coupled non-linear equations. This system is also degenerate because only eq. (2.3b) (eq. (2.3a)) will survive at $s = 0(1)$ where the phase pressure $p_a(p_o)$ has no meaning. For these and many other reasons, mathematical and numerical studies of this problem including numerical simulations are very challenging. In order to avoid this difficulty, we propose a new global pressure formulation for incompressible, immiscible two-phase flows with two dissolved components. For

purposes below, we define

$$\eta^c(s,c,\Gamma) = \int_{s_c}^{s} \frac{\partial}{\partial c}\left(f_o - f_a\right)(\zeta,c,\Gamma)\frac{dp_c}{d\zeta}(\zeta,\Gamma)d\zeta + \int_{\Gamma_c}^{\Gamma} \frac{\partial}{\partial c}\left(f_o - f_a\right)(s,c,\xi)\frac{dp_c}{d\xi}(s,\xi)d\xi, \tag{2.25a}$$

$$\eta^s(s,c,\Gamma) = \int_{\Gamma_c}^{\Gamma} \frac{\partial}{\partial s}\left(f_o - f_a\right)(s,c,\xi)\frac{dp_c}{d\xi}(s,\xi)d\xi, \tag{2.25b}$$

$$\eta^\Gamma(s,c,\Gamma) = \int_{s_c}^{s} \frac{\partial}{\partial \Gamma}\left(f_o - f_a\right)(\zeta,c,\Gamma)\frac{dp_c}{d\zeta}(\zeta,\Gamma)d\zeta, \tag{2.25c}$$

where s_c is the value of the aqueous phase saturation at which $p_c(s_c,\Gamma) = 0$ and Γ_c is the surfactant concentration value defined similarly by $p_c(s,\Gamma_c) = 0$. Using the above relations, we define a function p, called the global pressure, as follows.

$$p = \frac{(p_o + p_a)}{2} + \frac{1}{2}\int_{s_c}^{s}(f_o - f_a)(\zeta,c,\Gamma)\frac{dp_c}{d\zeta}(\zeta,\Gamma)d\zeta + \frac{1}{2}\int_{\Gamma_c}^{\Gamma}(f_o - f_a)(s,c,\xi)\frac{dp_c}{d\xi}(s,\xi)d\xi - \frac{1}{2}\int \eta^s(s,c,\Gamma)\,ds - \frac{1}{2}\int \eta^c(s,c,\Gamma)\,dc - \frac{1}{2}\int \eta^\Gamma(s,c,\Gamma)\,d\Gamma + C, \tag{2.26}$$

where C is a reference pressure which takes the place of an integration constant in the calculations. Using the new definition of eq. (2.26) a new global pressure formulation is obtained for the SP flooding problem in terms of the primary variables (p,s,c,Γ). This

new system of equations in non-conservative form is given by

$$-\boldsymbol{\nabla}\cdot(\mathbf{K}(\mathbf{x})\lambda(s,c,\Gamma)\boldsymbol{\nabla}p) = q_a + q_o, \tag{2.27a}$$

$$\phi\frac{\partial s}{\partial t} + \frac{\partial f_a}{\partial s}\mathbf{v}\cdot\boldsymbol{\nabla}s + \boldsymbol{\nabla}\cdot\left(\boldsymbol{D}\frac{\partial p_c}{\partial s}\boldsymbol{\nabla}s\right) = g_s - \mathbf{v}\cdot\left(\frac{\partial f_a}{\partial c}\boldsymbol{\nabla}c + \frac{\partial f_a}{\partial \Gamma}\boldsymbol{\nabla}\Gamma\right) - \boldsymbol{\nabla}\cdot\left(\boldsymbol{D}\frac{\partial p_c}{\partial \Gamma}\boldsymbol{\nabla}\Gamma\right), \tag{2.27b}$$

$$\phi\frac{\partial c}{\partial t} + \left(\frac{f_a}{s}\mathbf{v} + \frac{\boldsymbol{D}}{s}\frac{\partial p_c}{\partial s}\boldsymbol{\nabla}s + \frac{\boldsymbol{D}}{s}\frac{\partial p_c}{\partial \Gamma}\boldsymbol{\nabla}\Gamma\right)\cdot\boldsymbol{\nabla}c = g_c, \tag{2.27c}$$

$$\phi\frac{\partial \Gamma}{\partial t} + \left(\frac{f_a}{s}\mathbf{v} + \frac{\boldsymbol{D}}{s}\frac{\partial p_c}{\partial s}\boldsymbol{\nabla}s + \frac{\boldsymbol{D}}{s}\frac{\partial p_c}{\partial \Gamma}\boldsymbol{\nabla}\Gamma\right)\cdot\boldsymbol{\nabla}\Gamma = g_\Gamma, \tag{2.27d}$$

where $\boldsymbol{D}(s,c,\Gamma) = \mathbf{K}(\mathbf{x})\lambda_o(s,\Gamma)f_a(s,c,\Gamma)$ and

$$(g_s,\, g_c,\, g_\Gamma) = \begin{cases} \left((1-f_a)Q,\ \dfrac{(c^i-c)Q}{s},\ \dfrac{(\Gamma^i-\Gamma)Q}{s}\right) \\ (0,0,0) \end{cases} \quad \text{at } \mathbf{x} = \begin{cases} \mathbf{x}^i & \text{(Source)} \\ \Omega\setminus\{\mathbf{x}^i\} & \text{(Elsewhere)} \end{cases}.$$

In order to solve the system of eqs. (2.27a)–(2.27d), we need the viscosity relations, and the constitutive relations for the capillary pressure and the relative permeabilities. These relations are given below.

The aqueous phase viscosity is modeled by a linear function of polymer concentration.

$$\mu_a = \mu_w(1+\gamma c). \tag{2.28}$$

Here μ_w is the viscosity of pure water and the coefficient γ characterizes the particular polymer. In the numerical simulations, we study the effect of polymer by varying the viscosity ratio M_μ, defined as $M_\mu = \mu_o/\mu_w$ for waterflooding and $M_\mu = \mu_o/\mu_a$ for polymer flooding, between the values of 1.25 and 10.

Capillary pressure is strongly dependent on the surfactant concentration. It reduces

steadily with increasing surfactant concentration up to the CMC (Critical Micelle Concentration) due to the reduction in interfacial tension (IFT). The relationship of IFT with surfactant concentration has been extensively studied experimentally and is known to be inversely proportional (Fig. 2.3). In order to model this complex dependence of capillary pressure on s as well as on Γ, we adopt the approach (see [79]) that is often followed in SEAR (Surfactant Enhanced Aquifer Remediation) processes. It is given by the following empirical relation.

$$\left(\frac{p_b}{p_c}\right)^{\omega_1} = \left(1 - \frac{s - s_{ra}^{\sigma}}{1 - s_{ra}^{\sigma} - s_{ro}^{\sigma}}\right). \tag{2.29}$$

In the above, s_{ra}^{σ} and s_{ro}^{σ} are the residual saturations for the aqueous and oleic phases respectively at interfacial tension σ, ω_1 is a curve fitting parameter called the pore-size index and p_b is called the entry pressure. The entry pressure changes with the interfacial tension of the system. This effect is captured using a Leverett function scaling procedure in which $p_b = \sigma\omega_2(\phi/K)^{1/2}$ where ω_2 is a proportionality constant and K is the geometric mean of the horizontal permeabilities in the x and y directions. Thus p_b implicitly captures the relationship between capillary pressure p_c and surfactant concentration Γ via the interfacial tension $\sigma = \sigma(\Gamma)$. Hence the capillary pressure is modeled as a function of porosity, permeability, the aqueous phase saturation and the surfactant concentration.

From surface chemistry we know that surfactants improve the mobilization of trapped oil by reducing the interfacial tension forces which in turn leads to the reduction of the capillary pressure between oil and water. But this also leads to a reduction of the residual saturations and hence an increase in the relative permeabilities of the two phases. In fact, for IFT values below 0.1 mN/m (milliNewton per meter) the relative permeabilities of both the phases increase substantially due to a decrease of the residual saturations of the two phases with an increase in IFT (captured through the capillary number, N_c). This effect on the relative permeabilities and the residual saturations can be captured through the relative

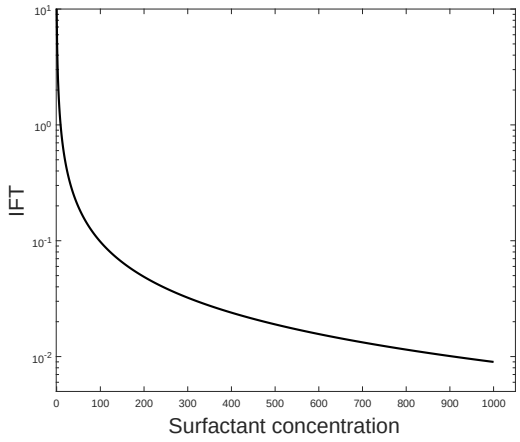

Figure 2.3: Oil-water interfacial tension σ as a function of surfactant concentration Γ.

permeability curves. The relative permeability curves are modeled following the approach of Amaefule and Handy [80] as

$$\begin{aligned} k_{ra}^{\sigma} &= \left(\frac{s - s_{ra}^{\sigma}}{1 - s_{ra}^{\sigma}}\right) \left\{ 2.5 s_{ra}^{\sigma} \left[\left(\frac{s - s_{ra}^{\sigma}}{1 - s_{ra}^{\sigma}}\right)^2 - 1 \right] + 1 \right\}, \\ k_{ro}^{\sigma} &= \left(1 - \frac{s - s_{ra}^{\sigma}}{1 - s_{ra}^{\sigma} - s_{ro}^{\sigma}}\right) \left\{ 5 s_{ro}^{\sigma} \left[\left(1 - \frac{s - s_{ra}^{\sigma}}{1 - s_{ra}^{\sigma} - s_{ro}^{\sigma}}\right) - 1 \right] + 1 \right\}. \end{aligned} \tag{2.30}$$

Here k_{ra}^{σ} and k_{ro}^{σ} are the respective relative permeabilities of the aqueous and the oleic phases at an interfacial tension of σ.

To use the above models for the capillary pressure, eq. (2.29), and the relative permeability, eq. (2.30), we need to be able to determine the variation in the residual saturations of the phases with changes in the interfacial tension. For this purpose, we use the empirical expressions that relate the IFT and the residual saturations using the capillary number (see

[80]) given as follows

$$s_{ro}^{\sigma} = \begin{cases} s_{ro}^{\sigma 0} & N_c < N_{co} \\ s_{ro}^{\sigma 0} \left(\frac{N_{co}}{N_c}\right)^{0.5213} & N_c \geq N_{co} \end{cases}, \qquad s_{ra}^{\sigma} = \begin{cases} s_{ra}^{\sigma 0} & N_c < N_{ca} \\ s_{ra}^{\sigma 0} \left(\frac{N_{ca}}{N_c}\right)^{0.1534} & N_c \geq N_{ca} \end{cases}. \tag{2.31}$$

Here the exponents are obtained through curve fitting on experimental data. $N_c = \frac{\mu|\mathbf{v}|}{\sigma}$ is the capillary number calculated from the displacing fluid viscosity μ, Darcy velocity $\mathbf{v}$ and interfacial tension, σ. The oleic and the aqueous phase capillary numbers at interfacial tension, $\sigma 0$, are N_{co} and N_{ca} respectively. Also, $s_{ra}^{\sigma 0}$ and $s_{ro}^{\sigma 0}$ are the residual saturations of the aqueous and oleic phases respectively at interfacial tension $\sigma 0$. Finally, to complete the model we use the following empirical relationship between the surfactant concentration and the interfacial tension that closely resembles the behavior observed in laboratory experiments (see [81]),

$$\sigma = \frac{10.001}{\Gamma + 1} - 0.001. \tag{2.32}$$

The flow and transport equations given by eqs. (2.27a)–(2.27d) combined with the constitutive relations given by eqs. (2.28)–(2.32) form a complete mathematical model for the SP flooding.

3. NUMERICAL METHODS AND CONVERGENCE ANALYSIS*

In this chapter we introduce the hybrid numerical method and analyze the convergence behavior. In section 3.1 we present the hybrid numerical method by considering the system of equations describing the two-component two-phase flow (SP flooding) problem given by eqs. (2.27a)–(2.27d) as the model problem. The model is composed of an elliptic pressure equation and a system of three transport equations. The numerical procedure for solving the elliptic pressure equation of the two-component flow (SP flooding) problem (see eq. (2.27a)) is identical to that of the one-component two-phase flow (polymer flooding) problem (see eq. (2.12c)). However, the system of transport equations vary for these two flow problems. At the end of section 3.1, we also present the analogous discretized formulation for the system of transport equations of the one-component flow (polymer flooding) problem, given by eqs. (2.12a) and (2.12b). In section 3.3 we discuss the convergence behavior of the method and present error estimates. For the analysis, we consider a reduced system of equations representing the one-component two-phase flow problem (polymer flooding) in a single spatial dimension. Possible extensions of the analysis both to a two-dimensional flow system and also to a two-component two-phase flow (SP floooding) system are also discussed.

3.1 Numerical Method

The governing eqs. (2.27a)–(2.27d) form a coupled system of nonlinear partial differential equations. The total mobility $\lambda(s, c, \Gamma)$ appearing in the pressure eq. (2.27a) depends on the solution of the transport equations. Also, the transport eqs. (2.27b)–(2.27d) depend on the total velocity $\mathbf{v}$, thus introducing a coupling with the elliptic pressure equation. Ad-

*Part of this chapter is reprinted from Journal of Computational Physics, 335, Prabir Daripa and Sourav Dutta, "Modeling and simulation of surfactant-polymer flooding using a new hybrid method", 249-282, doi: 10.1016/j.jcp.2017.01.038, Copyright (2017) with permission from Elsevier.

ditionally, since the phase mobilities λ_a and λ_o (and so the fractional flow functions f_a and f_o) are nonlinear functions of the water saturation s and the species concentrations c and Γ, the equations are nonlinear. For each time step, this coupled system of equations is solved using the following sequential procedure. First, the initial values of s, c and Γ are used as input for solving the elliptic eq. (2.27a) for the global pressure p and the total velocity $\mathbf{v}$ using a discontinuous finite element formulation which is described in section 3.1.2. Next, $\mathbf{v}$ is used as an input in the transport eqs. (2.27b)–(2.27d) to advance the current values of triplet (s, c, Γ) to the next time level by solving these equations using a combination of the MMOC and an implicit-time finite difference scheme. This sequential time-stepping process repeats until a suitable stopping criterion is reached. The numerical treatment of the nonlinearity has been discussed in section 3.1.3 on the finite difference numerical scheme.

Below, section 3.1.1 describes two different computational grids that are used for solving the system of equations. The transport equations are solved on a uniform Cartesian grid that is referred to as the FD (finite difference) grid. The pressure equation is solved using a non-traditional discontinuous finite element formulation on a fixed mesh, composed of triangular elements, that is referred to as the FE (finite element) grid. Section 3.1.2 describes the finite element formulation in detail. The MMOC based finite difference method used for the transport equations is presented in section 3.1.3. Finally, the algorithm, the pseudocode, and the flowchart of the method are presented in section 3.2.

3.1.1 Computational grid

The numerical simulations have been performed in two types of domains: quarter five-spot and rectilinear. The quarter five-spot domain $\Omega = [0, 1]^2$ has an injection well at $(0, 0)$, a production well at $(1, 1)$ and no flow conditions on the rest of the boundary, as shown in Figure 3.1(a). The rectilinear flow domain $\Omega = [0, 1]^2$ has a line source at $x = 0$ and a line sink at $x = 1$. No flow conditions are specified on the remaining top and bottom

horizontal boundaries, as shown in Figure 3.1(b).

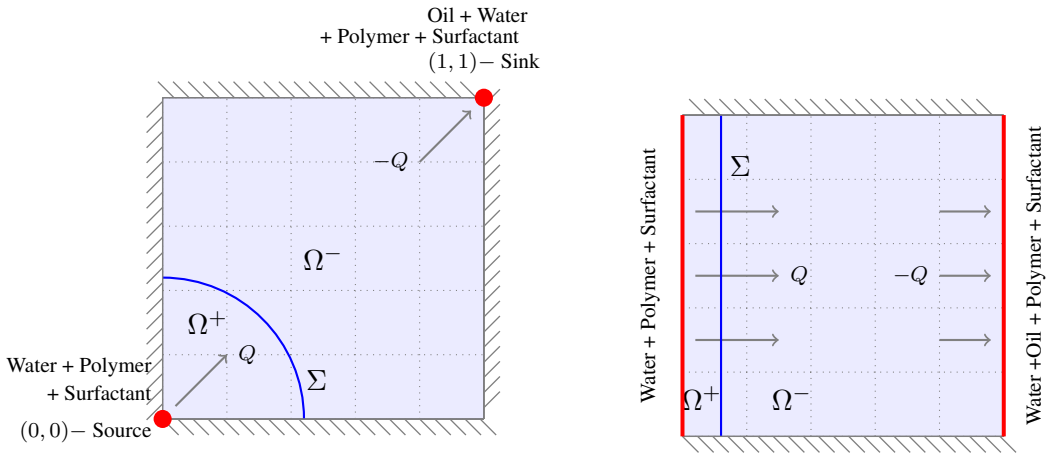

(a) Schematic of a quarter five-spot reservoir

(b) Schematic of a rectilinear flow reservoir

Figure 3.1: Schematic of two different types of simulation domains where Q is the injection/production rate

The FD grid used to solve the system of coupled transport eqs. (2.27b)–(2.27d) is constructed by partitioning the domain Ω into uniform rectangular cells. For positive integers $I, J \in \mathscr{Z}^+$, set $\Delta x = (x^{max} - x^{min})/I = 1/I$ and $\Delta y = (y^{max} - y^{min})/J = 1/J$. A uniform Cartesian grid $(x_i, y_j) = (i\Delta x, j\Delta y)$ is defined for $i = 0, \ldots, I$ and $j = 0, \ldots, J$ where $\mathbf{x} = (x_i, y_j)$ is called a grid point. For any point with $i = 0, I$ or $j = 0, J$, it is called a boundary point, otherwise it is called an interior point. The grid size is defined as $h = max(\Delta x, \Delta y) > 0$, see Figure 3.2(a). In our numerical simulations we have assumed $\Delta x = \Delta y = h$.

The FE grid used to solve the elliptic flow eq. (2.27a) for the global pressure, is constructed by introducing triangulations within the FD grid. This means every rectangular region $[x_i, x_{i+1}] \times [y_j, y_{j+1}]$ is divided into two right triangular regions: one is bounded by $x = x_i, y = y_j$ and $y = \frac{y_{j+1}-y_j}{x_i-x_{i+1}}(x - x_{i+1}) + y_j$, the other is bounded by $x = x_{i+1}, y = y_{j+1}$

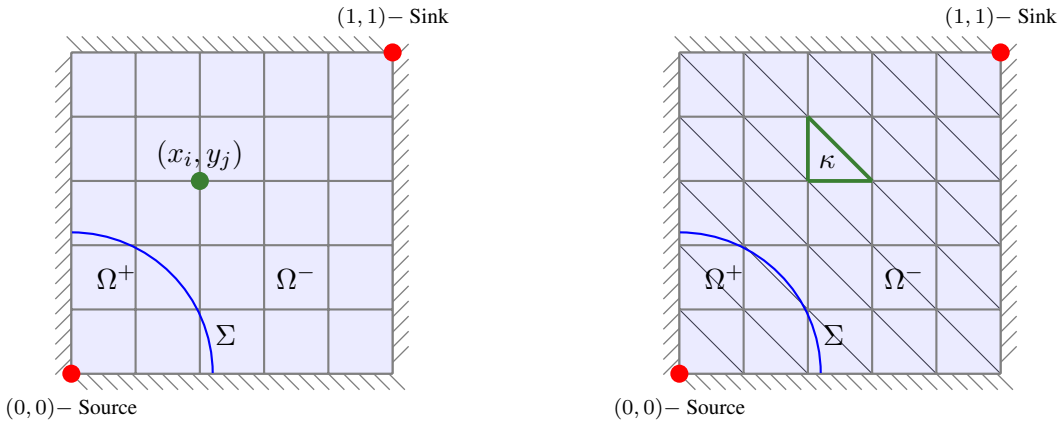

(a) Uniform FD grid for the transport equations

(b) Uniform FE mesh for the pressure equation

Figure 3.2: Discretization of the computational domain for (a) the Transport Equations and (b) the Pressure Equation.

and $y = \frac{y_{j+1}-y_j}{x_i-x_{i+1}}(x-x_{i+1})+y_j$. Union of all those triangular regions gives a uniform triangulation, $L^h = \{\kappa | \kappa \text{ is a triangular element}\}$, see Figure 3.2(b). Alternatively, by choosing the hypotenuse to be $y = \frac{y_{j+1}-y_j}{x_{i+1}-x_i}(x-x_i)+y_j$ we get a different but computationally equivalent uniform triangulation from the same Cartesian grid.

3.1.2 Pressure equation

The elliptic problem for the global pressure is given by

$$-\boldsymbol{\nabla}\cdot(\mathbf{K}(\mathbf{x})\lambda(s,c,\Gamma)\boldsymbol{\nabla}p) = \tilde{q}, \qquad \mathbf{x}\in\Omega\backslash\Sigma, \tag{3.1a}$$

$$(\mathbf{K}(\mathbf{x})\lambda(s,c,\Gamma)\boldsymbol{\nabla}p)\cdot\hat{\mathbf{n}} = 0, \qquad \mathbf{x}\in\partial\Omega, \tag{3.1b}$$

where $\tilde{q} = q_a + q_o$ and Σ denotes the union of the interfaces that separate Ω into several subdomains. These interfaces are a macroscopic averaged picture. Also, at any arbitrary time during the flooding process, there might be many such interfaces in the domain generated dynamically due to the flow and hence there can be several subdomains created

inside Ω. However, for simplicity of exposition, we have taken only two subdomains, Ω^+ and Ω^- separated by an interface Ω which also happens to be the initial configuration of the domain for most of our injection policies in this paper as we will see later.

The above problem is solved using a discontinuous finite element formulation (see [82]) with a uniform triangulated non-body-fitted grid, which is second order accurate in the L^∞ norm for matrix coefficient elliptic equations with discontinuities across interfaces. We prescribe the following kinematic condition at the interface Σ

$$[\mathbf{K}(\mathbf{x})\lambda(s,c,\Gamma)\boldsymbol{\nabla}p\cdot\hat{\mathbf{n}}]_\Sigma = 0, \tag{3.2}$$

where $\hat{\mathbf{n}}$ is the outward unit normal which points from Ω^- to Ω^+. We assume the boundary $\partial\Omega$ and the interface Σ to be Lipschitz continuous. Hence a unit normal vector, $\hat{\mathbf{n}}$ can be defined a.e. on Σ. We generalize the weak formulation for the elliptic equation in the usual Sobolev space $H^1(\Omega)$ with $\psi \in H^1(\Omega)$ as

$$\int_{\Omega^+} \mathbf{K}\lambda\boldsymbol{\nabla}p\boldsymbol{\nabla}\psi + \int_{\Omega^-} \mathbf{K}\lambda\boldsymbol{\nabla}p\boldsymbol{\nabla}\psi - \int_{\partial\Omega} \mathbf{K}\lambda\psi\boldsymbol{\nabla}p.\hat{\mathbf{n}} = \int_{\Omega} \tilde{q}\psi. \tag{3.3}$$

The coefficient of the capillary dissipation term in the water saturation equation, given by $\mathbf{K}\lambda_o f_a \frac{\partial p_c}{\partial s}$, vanishes at extreme values of the water saturation $s = s_{ra}$ and $s = 1 - s_{ro}$ because $f_a(s = s_{ra}) = 0$ and $\lambda_o(s = 1 - s_{ro}) = 0$. This makes it a degenerate diffusion term and the corresponding transport equation becomes nonlinear hyperbolic in nature. This nonlinear hyperbolic equation can develop shocks in finite time in the solution. Also, the initial saturation profile $s(\mathbf{x}, 0) = s_0(\mathbf{x})$ has a discontinuity. For these reasons, the coefficient $\mathbf{K}\lambda(s,c,\Gamma)$ of the elliptic global pressure equation may become discontinuous across the discontinuity in the initial saturation profile and also across the shocks that

may develop. The discontinuous finite element formulation has been adopted as it can efficiently resolve such discontinuities in the elliptic coefficient by incorporating it in the basis functions and redefining the weak formulation. In the region where the coefficient has no discontinuity or when the dissipation introduced by the capillary pressure term smoothens out the the initial discontinuity in the water saturation, the basis functions automatically reduce to the linear basis functions of a traditional finite element formulation. Additionally due to the nonlinearity of the system and the heterogeneous permeability, if discontinuities were to arise in the solution over time then the non-traditional finite element formulation is capable of treating them efficiently. Moreover, this formulation uses a fixed finite element mesh, thus avoiding the expensive computation of generating a mesh every time step as would be necessary for a traditional finite element method that uses a body-fitted grid. The method ensures that the resulting linear system is positive definite and it achieves second order accuracy in the L^∞ norm.

In the numerical results presented in this paper, the degeneracy in the capillary dissipation term has been avoided because of the restriction $0 < s_{ra} < s < 1 - s_{ro} < 1$. This is a realistic physical assumption which means that the initial water saturation in the reservoir (connate water saturation) is not as low as the residual water saturation and during the displacement process the oil saturation does not get reduced to the residual oil saturation in finite time.

The finite element method will be explained in detail below. The elements, κ of triangulation, L^h, introduced in section 3.1.1 are classified into regular cells and interface cells. We call κ a regular cell if its vertices are in the same subdomain and an interface cell when its vertices belong to different subdomains. For an interface cell, $\kappa = \kappa^+ \cup \kappa^-$ where κ^+ and κ^- are separated by a line segment Σ_k^h, obtained by joining the two points where the interface Σ intersects the sides or the vertices of that interface cell. A set of grid functions, $H^{1,h} = \{\omega^h \,|\, \omega^h = \omega_{i,j}\,;\, 0 \le i \le I, 0 \le j \le J\}$ are defined on the grid points

of the mesh L^h. An extension operator $U^h : H^{1,h} \to H^1(\kappa)$ is constructed as follows. For any $\phi^h \in H^{1,h}$, $U^h(\phi^h)$ is a piecewise linear function and matches ϕ^h on the grid points. In a regular cell, it is a linear function that interpolates the values of ϕ^h at the grid points. In an interface cell, it consists of two pieces of linear functions, one each defined on κ^+ and κ^-. The location of the discontinuity of the extended function $U^h(\phi^h)$ in an interface cell is on the line segment Σ_k^h. Hence an interface jump condition on the pressure, p, if there is one, can be imposed on the two end points of this line segment at $\{\partial\kappa\} \cap \{\Sigma_k^h\}$ while the interface jump condition, eq. (3.2), is imposed at the middle point of Σ_k^h. The construction of such extension operators and proof of their uniqueness can be found in the literature [82, 83, 84].

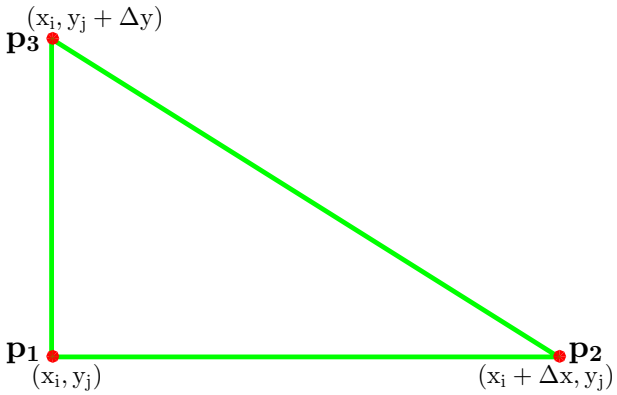

Figure 3.3: Regular cell

For every $\phi^h \in H^{1,h}$, we can define a unique extension $U^h(\phi^h)$ from knowing the position of the interface Σ. For a regular cell, as in Figure 3.3 we construct $U^h(\phi^h)$ as

$$U^h(\phi^h) = \phi(p_1) + \frac{\phi(p_2) - \phi(p_1)}{\Delta x}(x - x_i) + \frac{\phi(p_3) - \phi(p_1)}{\Delta y}(y - y_j). \tag{3.4}$$

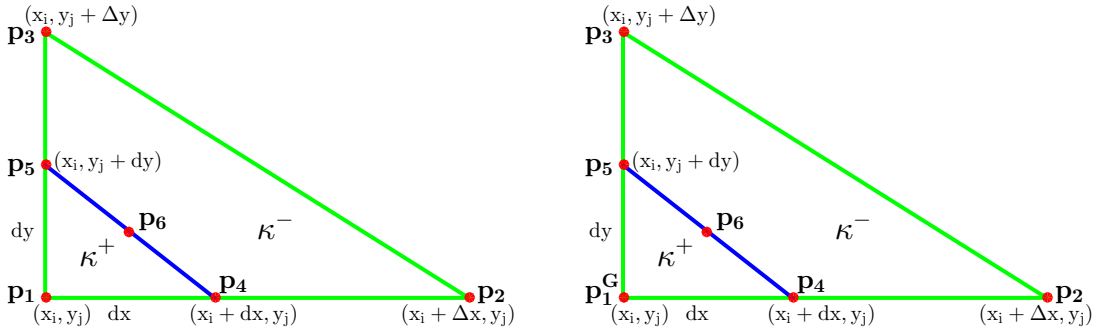

(a) Formulation for κ^+

(b) Ghost point formulation for κ^-

Figure 3.4: Case 1 - the interface cutting through two legs

For an interface cell, κ there are two cases. Case 1 is when the interface cuts through two legs of κ (as in Figure 3.4), and Case 2 is when the interface cuts through one leg and the hypotenuse of κ (as in Figure 3.5). As an example, we construct the extension function for Case 1 and the construction for Case 2 follows similarly. Then for Case 1,

$$U^h(\phi^h) = \begin{cases} \phi(p_1) + \phi_x^+(x - x_i) + \phi_y^+(y - y_j) & \text{for } (x, y) \in \kappa^+, \\ \phi(p_2) + \phi_x^-(x - x_i - \Delta x) + \phi_y^-(y - y_j) & \text{for } (x, y) \in \kappa^-, \end{cases} \tag{3.5}$$

where for $(x, y) \in \kappa^+$ (as in Figure 3.4(a)),

$$\phi_x^+ = \frac{\phi(p_4) - \phi(p_1)}{dx} \quad \& \quad \phi_y^+ = \frac{\phi(p_5) - \phi(p_1)}{dy}, \tag{3.6}$$

and for $(x, y) \in \kappa^-$ (as in Figure 3.4(b)),

$$\phi_x^- = \frac{\phi(p_2) - \phi(p_4)}{\Delta x - dx} \quad \& \quad \phi_y^- = \frac{\phi(p_3) - \phi(p_5)}{\Delta y - dy}. \tag{3.7}$$

For κ^- (as in Figure 3.4(b)) above, it is assumed that the extensions of p_3p_5 and p_2p_4

intersect at a ghost point, p_1^G and hence

$$\frac{\phi(p_1^G) - \phi(p_4)}{dx} = \frac{\phi(p_4) - \phi(p_2)}{\Delta x - dx} \quad \& \quad \frac{\phi(p_1^G) - \phi(p_5)}{dy} = \frac{\phi(p_1^G) - \phi(p_3)}{\Delta y}. \tag{3.8}$$

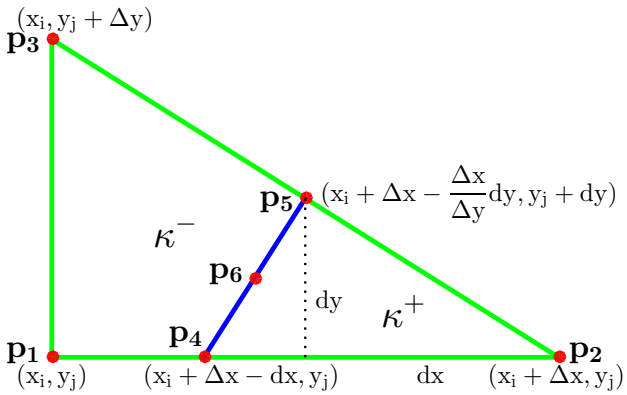

Figure 3.5: Case 2 - the interface cutting through one leg and the hypotenuse

We note that ϕ_x^+ and ϕ_x^- are linear functions of $\phi(p_1), \phi(p_2), \phi(p_3)$ and $\phi(p_4)$ from eq. (3.6) and eq. (3.7). We rewrite eq. (3.8) as

$$\phi(p_5) = \phi(p_1^G) - \frac{dy}{\Delta y}\left(\phi(p_1^G) - \phi(p_3)\right), \tag{3.9}$$

$$\phi(p_1^G) = \phi(p_4) + \frac{dx}{\Delta x - dx}\left(\phi(p_4) - \phi(p_2)\right). \tag{3.10}$$

Using eq. (3.9) and eq. (3.10) in eq. (3.6) and eq. (3.7), ϕ_y^+ and ϕ_y^- respectively can be obtained as linear functions of $\phi(p_1)$, $\phi(p_2)$, $\phi(p_3)$ and $\phi(p_4)$. The kinematic condition, eq. (3.2), is imposed as given below,

$$0 = \mathbf{K}^+\lambda^+\boldsymbol{\nabla}\phi^+ \cdot \hat{\mathbf{n}} - \mathbf{K}^-\lambda^-\boldsymbol{\nabla}\phi^- \cdot \hat{\mathbf{n}}. \tag{3.11}$$

Given $\hat{\mathbf{n}} = (n_1, n_2) = \left(\frac{-dy}{\sqrt{dx^2+dy^2}}, \frac{-dx}{\sqrt{dx^2+dy^2}} \right)$ and the permeability $\mathbf{K} = \left(\begin{smallmatrix} k & 0 \\ 0 & k \end{smallmatrix} \right)$ for an isotropic porous medium, eq. (3.11) reduces to

$$k^+\lambda^+\phi_x^+ n_1 + k^+\lambda^+\phi_y^+ n_2 = k^-\lambda^-\phi_x^- n_1 + k^-\lambda^-\phi_y^- n_2. \tag{3.12}$$

Using eq. (3.12), $\phi(p_4)$ is eliminated so that, ϕ_x^+, ϕ_y^+, ϕ_x^- and ϕ_y^- are obtained uniquely as linear combinations of $\phi(p_1)$, $\phi(p_2)$ and $\phi(p_3)$ in such a way that the coefficients are finite and independent of ϕ^h. Thus the extension operator U^h, given by eq. (3.5), for Case 1 of an interface cell becomes well defined as in the case of a regular cell given by eq. (3.4). Similarly, $U^h(\phi^h)$ can be defined for Case 2 of an interface cell (Figure 3.5) with finite and well defined coefficients in the following way,

$$U^h(\phi^h) = \begin{cases} \phi(p_2) + \phi_x^+(x - x_i - \Delta x) + \phi_y^+(y - y_j) & \text{for } (x,y) \in \kappa^+, \\ \phi(p_1) + \phi_x^-(x - x_i) + \frac{\phi(p_3)-\phi(p_1)}{\Delta y}(y - y_j) & \text{for } (x,y) \in \kappa^-, \end{cases} \tag{3.13}$$

where

$$\phi_x^+ = \frac{\phi(p_2) - \phi(p_4)}{dx} \quad \& \quad \phi_y^+ = \frac{\phi(p_5) - \phi(p_2)}{dy} + \frac{\phi(p_2) - \phi(p_4)}{dx}\frac{\Delta x}{\Delta y}, \tag{3.14}$$

$$\phi_x^- = \frac{\phi(p_4) - \phi(p_1)}{\Delta x - dx}. \tag{3.15}$$

Using the extension functions as defined above, the weak formulation eq. (3.3) reduces to finding a discrete function $\phi^h \in H^{1,h}$ such that it satisfies eq. (3.1b) on the boundary points and so that for all $\psi^h \in H^{1,h}$,

$$\sum_{K\in L^h}\left(\int_{K^+}\mathbf{K}\lambda\,\boldsymbol{\nabla}U^h(\phi^h)\boldsymbol{\nabla}U^h(\psi^h)+\int_{K^-}\mathbf{K}\lambda\,\boldsymbol{\nabla}U^h(\phi^h)\boldsymbol{\nabla}U^h(\psi^h)\right.$$
$$\left.-\int_{\partial K}\mathbf{K}\lambda\,U^h(\psi^h)\boldsymbol{\nabla}U^h(\phi^h)\cdot\hat{\mathbf{n}}\right)=\sum_{K\in L^h}\left(\int_{K^+}\tilde{q}\,U^h(\psi^h)+\int_{K^-}\tilde{q}\,U^h(\psi^h)\right). \tag{3.16}$$

It can be shown that if $\mathbf{K}(\mathbf{x})$ is positive definite, then the matrix obtained for the linear system of the discretized weak form, eq. (3.16), is also positive definite and is therefore invertible.

3.1.3 Transport equations

As mentioned earlier, the transport eqs. (2.27b)–(2.27d), are solved using the MMOC. In convection dominated diffusion problems like these, for any reasonable fluid injection rate and capillary dissipation strength, the flow is essentially along the characteristics. The principal gain from using the MMOC procedure to solve these problems is in the time truncation, as the solution changes much less rapidly in the characteristic τ direction than in the t direction. Larger time steps can be used in these methods, thus improving the efficiency without adversely affecting the accuracy. Additionally there is no stability limitation on the size of Δt if an implicit time marching scheme is adopted as implicit matrix solvers are usually much less sensitive to numerical instability. Next, we present the procedure of MMOC.

The transport term, $\phi s_t + \frac{\partial f_a}{\partial s}\mathbf{v}\cdot\boldsymbol{\nabla}s$ in eq. (2.27b) is replaced by a derivative along its characteristic direction in the following way

$$\frac{\partial}{\partial\tau_s}=\frac{1}{\psi_s}\left(\phi\frac{\partial}{\partial t}+\frac{\partial f_a}{\partial s}\mathbf{v}\cdot\boldsymbol{\nabla}\right), \tag{3.17}$$

where τ_s is used to parametrize the characteristics. Here ψ_s is a suitable normalization that

simplifies the numerical discretization of the characteristic derivative and is defined by

$$\psi_s = \left[\phi^2 + \left(\frac{\partial f_a}{\partial s}\right)^2 |\mathbf{v}|^2\right]^{1/2}. \tag{3.18}$$

Then eq. (2.27b) is equivalently written in the form

$$\psi_s \frac{\partial s}{\partial \tau_s} + \boldsymbol{\nabla} \cdot (\boldsymbol{D} \frac{\partial p_c}{\partial s} \boldsymbol{\nabla} s) = \tilde{g}_s - \frac{\partial f_a}{\partial c} \mathbf{v} \cdot \boldsymbol{\nabla} c - \frac{\partial f_a}{\partial \Gamma} \mathbf{v} \cdot \boldsymbol{\nabla} \Gamma - \boldsymbol{\nabla} \cdot \left(D \frac{\partial p_c}{\partial \Gamma} \boldsymbol{\nabla} \Gamma \right), \tag{3.19}$$

where $\tilde{g}_s = (1 - f_a) Q \delta(\mathbf{x} - \mathbf{x}^i)$ is the point source term.

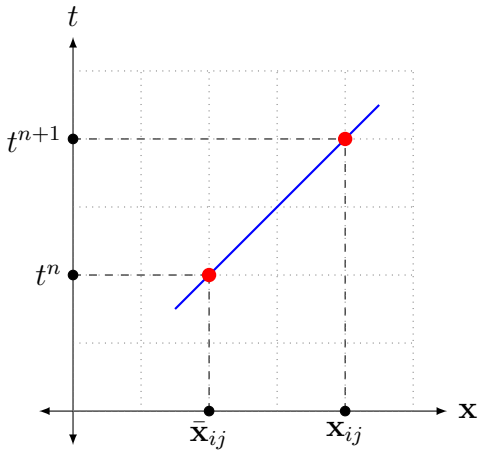

Figure 3.6: Discrete approximation of the characteristic curve from $\bar{\mathbf{x}}_{ij}$ to $\mathbf{x}_{ij}$ in 1D

For numerical computation, we use the spatial grid described in section 3.1.1 and the time interval $[0, T]$ is uniformly divided into N subintervals of length Δt, such that $t^n = n\Delta t$ and $T = N\Delta t$. Then we denote the grid values of the variables by $w_{ij}^n = w(\mathbf{x}_{ij}, t^n)$ where $\mathbf{x}_{ij} = \mathbf{x}(ih, jh)$. Consider that the solution is known at some time t^n and the solution at a subsequent time t^{n+1} needs to be computed. Then starting from any point

$(\mathbf{x}_{ij}, t^{n+1})$ we trace backward along the characteristics to a point $(\bar{\mathbf{x}}_{ij}, t^n)$ where the solution is already known.

Let the characteristics which originate from the point $\bar{\mathbf{x}}_{ij}$ at time t^n reach the point $\mathbf{x}_{ij}$ at time t^{n+1} (see Figure 3.6). From the equation of the characteristic curves given by

$$\frac{d\mathbf{x}}{d\tau_s} = \frac{1}{\phi}\frac{\partial f_a}{\partial s}\mathbf{v},$$

we can use numerical discretization to obtain an approximate value of $\bar{\mathbf{x}}_{ij}$ in the following way

$$\bar{\mathbf{x}}_{ij} = \mathbf{x}_{ij} - \frac{\partial f_a}{\partial s}(s_{ij}^n, c_{ij}^n, \Gamma_{ij}^n)\mathbf{v}_{ij}^n \Delta t/\phi. \tag{3.20}$$

Using eq. (3.20), the derivative in the characteristic direction, defined by eq. (3.17), is approximated by

$$\psi_s \frac{\partial s}{\partial \tau_s} \approx \psi_s \frac{s(\mathbf{x}_{ij}, t^{n+1}) - s(\bar{\mathbf{x}}_{ij}, t^n)}{\left[|\mathbf{x}_{ij} - \bar{\mathbf{x}}_{ij}|^2 + (\Delta t)^2\right]^{1/2}} = \phi \frac{s_{ij}^{n+1} - \bar{s}_{ij}^n}{\Delta t}, \tag{3.21}$$

where $s(\bar{\mathbf{x}}, t^n)$ is evaluated via bilinear interpolation of the approximate solution values at the nearby grid points, at time level $t^n = n\Delta t$. Note that in eq. (3.20), $\frac{\partial f_a}{\partial s}(s, c, \Gamma)\mathbf{v}$ is evaluated approximately as $\left(\frac{\partial f_a}{\partial s}\mathbf{v}\right)^n$ which is essentially a linearization step that freezes the nonlinear coefficient at the previous time step. In order to find a more accurate approximation of the characteristic curve passing through $(\mathbf{x}_{ij}, t^{n+1})$, the following predictor-corrector formulation can also be adopted.

$$\begin{aligned} \bar{\mathbf{x}}_{ij} &= \mathbf{x}_{ij} - \frac{\partial f_a}{\partial s}\left(s\left(\mathbf{x}_{ij} - \frac{\partial f_a}{\partial s}(s_{ij}^n, c_{ij}^n, \Gamma_{ij}^n)\tilde{\mathbf{v}}_{ij}^n \Delta t/\phi\right), c_{ij}^n, \Gamma_{ij}^n\right)\tilde{\mathbf{v}}_{ij}^n \Delta t/\phi, \\ \tilde{\mathbf{v}}_{ij}^n &= 2\mathbf{v}_{ij}^n - \mathbf{v}_{ij}^{n-1}. \end{aligned} \tag{3.22}$$

It has been shown that no essential improvement in accuracy can be expected over this alternative evaluation of $s(\bar{\mathbf{x}}, t^n)$ even if the position $\bar{\mathbf{x}}_{ij}$ and the function $s(\bar{\mathbf{x}}_{ij}, t^n)$ are iterated to convergence (see [68]). In our simulations, both the formulations given by eq. (3.20) and eq. (3.22) have been used interchangeably depending on whether accuracy or speed of computation is desirable. Equation (3.21) leads to the following implicit-time finite difference formulation for the water transport equation given by eq. (3.19)

$$\begin{aligned}\phi\frac{s_{ij}^{n+1}-\bar{s}_{ij}^{n}}{\Delta t}+\boldsymbol{\nabla}_h(\bar{\boldsymbol{D}}\boldsymbol{\nabla}_h s)_{ij}^{n+1}=(\tilde{g}_s)_{ij}^{n}-\left(\frac{\partial f_a}{\partial c}\right)_{ij}^{n}\left(\mathbf{v}_{ij}^{n}\cdot\boldsymbol{\nabla}_h c_{ij}^{n}\right)\\ -\left(\frac{\partial f_a}{\partial \Gamma}\right)_{ij}^{n}\left(\mathbf{v}_{ij}^{n}\cdot\boldsymbol{\nabla}_h \Gamma_{ij}^{n}\right)-\boldsymbol{\nabla}_h(\bar{D}_{ij}^{n}\boldsymbol{\nabla}_h\Gamma_{ij}^{n}),\end{aligned} \tag{3.23}$$

where

$$\bar{s}_{ij}^{n}=s(\bar{\mathbf{x}}_{ij},t^n)\qquad\&\qquad\bar{\boldsymbol{D}}_{ij}^{n}=\boldsymbol{D}(\bar{s}_{ij}^{n},c_{ij}^{n}), \tag{3.24}$$

$$\begin{aligned}\boldsymbol{\nabla}_h(\bar{\boldsymbol{D}}\nabla_h s)_{ij}^{n+1}&=\bar{\boldsymbol{D}}_{i+1/2,j}\frac{s_{i+1,j}^{n+1}-s_{i,j}^{n+1}}{\Delta x^2}-\bar{\boldsymbol{D}}_{i-1/2,j}\frac{s_{i,j}^{n+1}-s_{i-1,j}^{n+1}}{\Delta x^2}\\ &+\bar{\boldsymbol{D}}_{i,j+1/2}\frac{s_{i,j+1}^{n+1}-s_{i,j}^{n+1}}{\Delta y^2}-\bar{\boldsymbol{D}}_{i,j-1/2}\frac{s_{i,j}^{n+1}-s_{i,j-1}^{n+1}}{\Delta y^2},\end{aligned} \tag{3.25}$$

$$\bar{\boldsymbol{D}}_{i\pm1/2,j}=\frac{\boldsymbol{D}(\bar{s}_{i\pm1,j}^{n},c_{i\pm1,j}^{n})+\boldsymbol{D}(\bar{s}_{i,j}^{n},c_{i,j}^{n})}{2} \tag{3.26}$$

$$\bar{\boldsymbol{D}}_{i,j\pm1/2}=\frac{\boldsymbol{D}(\bar{s}_{i,j\pm1}^{n},c_{i,j\pm1}^{n})+\boldsymbol{D}(\bar{s}_{i,j}^{n},c_{i,j}^{n})}{2}. \tag{3.27}$$

In eqs. (3.24) and (3.25), the nonlinearity in the coefficient of the capillary term is approximated in a quasilinear manner by evaluating the coefficient at the previous time step. This is a standard approximation procedure that is usually adopted in many Eulerian-Lagrangian methods (see [85]).

A similar procedure is followed for discretizing the transport equations for polymer

and surfactant, given by eqs. (2.27c) and (2.27d). Let us define the following

$$\mathbf{b} = \frac{f}{s}\mathbf{v} + \frac{\boldsymbol{D}}{s}\frac{\partial p_c}{\partial s}\boldsymbol{\nabla} s + \frac{\boldsymbol{D}}{s}\frac{\partial p_c}{\partial \Gamma}\boldsymbol{\nabla}\Gamma, \qquad \psi = \left(\phi^2 + |\mathbf{b}|^2\right)^{1/2}. \tag{3.28}$$

Also let the characteristic parameters, τ_c and τ_Γ respectively, be associated with the advection terms $\phi c_t + \mathbf{b}\cdot\boldsymbol{\nabla} c$ and $\phi\Gamma_t + \mathbf{b}\cdot\boldsymbol{\nabla}\Gamma$. Even though we use different notations, the characteristic derivatives for both the parameters are defined by,

$$\frac{\partial}{\partial \tau_c} = \frac{\partial}{\partial \tau_\Gamma} = \frac{\phi}{\psi}\frac{\partial}{\partial t} + \frac{1}{\psi}\mathbf{b}\cdot\boldsymbol{\nabla}. \tag{3.29}$$

Then using eqs. (3.28) and (3.29), the polymer and surfactant transport eqs. (2.27c) and (2.27d) are rewritten as

$$\psi\frac{\partial c}{\partial \tau_c} + c\tilde{g} = \tilde{g}_c, \qquad \psi\frac{\partial \Gamma}{\partial \tau_\Gamma} + \Gamma\tilde{g} = \tilde{g}_\Gamma, \tag{3.30}$$

where $\tilde{g_c} = \frac{c^i Q}{s}\delta(\mathbf{x}-\mathbf{x}^i)$, $\tilde{g_\Gamma} = \frac{\Gamma^i Q}{s}\delta(\mathbf{x}-\mathbf{x}^i)$ and $\tilde{g} = \frac{Q}{s}\delta(\mathbf{x}-\mathbf{x}^i)$ are the source terms. All of these lead to the following system of implicit-time finite difference formulations for the SP flooding transport eqs. (2.27b)–(2.27d)

$$\begin{aligned}\phi\frac{s_{ij}^{n+1}-\bar{s}_{ij}^n}{\Delta t} + \boldsymbol{\nabla}_h(\bar{\boldsymbol{D}}_{ij}^n\boldsymbol{\nabla}_h s_{ij}^{n+1}) &= (\tilde{g}_s)_{ij}^n - \left(\frac{\partial f_a}{\partial c}\right)_{ij}^n\left(\mathbf{v}_{ij}^n\cdot\boldsymbol{\nabla}_h c_{ij}^n\right)\\ &\quad - \left(\frac{\partial f_a}{\partial \Gamma}\right)_{ij}^n\left(\mathbf{v}_{ij}^n\cdot\boldsymbol{\nabla}_h \Gamma_{ij}^n\right) - \boldsymbol{\nabla}_h(\bar{\boldsymbol{D}}_{ij}^n\boldsymbol{\nabla}_h\Gamma_{ij}^n), \quad (3.31a)\\ \phi\frac{c_{ij}^{n+1}-\bar{c}_{ij}^n}{\Delta t} + (\tilde{g})_{ij}^n\, c_{ij}^{n+1} &= (\tilde{g_c})_{ij}^n, \quad (3.31b)\\ \phi\frac{\Gamma_{ij}^{n+1}-\bar{\Gamma}_{ij}^n}{\Delta t} + (\tilde{g})_{ij}^n\,\Gamma_{ij}^{n+1} &= (\tilde{g_\Gamma})_{ij}^n. \quad (3.31c)\end{aligned}$$

Equations (3.31a)–(3.31c) give the MMOC based finite difference approximation of the transport system for the two-component two-phase flow problem given by eqs. (2.27b)–

(2.27d).

The MMOC procedure for solving the system of transport equations for the polymer flooding problem given by eqs. (2.18a) and (2.18b) is essentially the same. The advection terms in both the transport equations are replaced by the respective derivatives in the characteristic directions in the following way,

$$\psi_s \frac{\partial}{\partial \tau_s} = \phi \frac{\partial}{\partial t} + \frac{\partial f}{\partial s} \mathbf{v} \cdot \boldsymbol{\nabla}, \tag{3.32a}$$

$$\psi_c \frac{\partial}{\partial \tau_s} = \phi \frac{\partial}{\partial t} + \frac{f}{s} \mathbf{v} \cdot \boldsymbol{\nabla} + \frac{\boldsymbol{D}_p}{s} \boldsymbol{\nabla} s \cdot \boldsymbol{\nabla}, \tag{3.32b}$$

where $\boldsymbol{D}_p = \mathbf{K}(\mathbf{x}) \lambda_o(s) f(s,c) \frac{dp_c}{d\,s}$ and

$$\psi_s = \left[\phi^2 + \left(\frac{\partial f}{\partial s} \right)^2 |\mathbf{v}|^2 \right]^2, \tag{3.33a}$$

$$\psi_c = \left[\phi^2 + \left(\frac{f}{s} \right)^2 |\mathbf{v}|^2 + \left(\frac{\boldsymbol{D}_p}{s} \right)^2 |\nabla s|^2 \right]^{1/2}. \tag{3.33b}$$

The above definitions are used to rewrite the transport eqs. (2.18a) and (2.18b) as

$$\psi_s \frac{\partial s}{\partial \tau_s} + \boldsymbol{\nabla} \cdot (\boldsymbol{D}_p \boldsymbol{\nabla} s) = \tilde{G}_s - \frac{\partial f}{\partial c} \mathbf{v} \cdot \boldsymbol{\nabla} c, \tag{3.34a}$$

$$\psi_c \frac{\partial c}{\partial \tau_c} + c\tilde{G} = \tilde{G}_c. \tag{3.34b}$$

Here $\tilde{G}_s = (1 - f_a) Q\, \delta(\mathbf{x} - \mathbf{x}^i)$, $\tilde{G} = \frac{Q}{s}\, \delta(\mathbf{x} - \mathbf{x}^i)$ and $\tilde{G}_c = \frac{c^i Q}{s}\, \delta(\mathbf{x} - \mathbf{x}^i)$. As shown before, by replacing the characteristic derivatives in eqs. (3.34a) and (3.34b) with their finite difference approximations and discretizing the remaining terms we obtain the following implicit-time finite difference formulation for polymer flooding transport eqs. (3.34a)

and (3.34b)

$$\phi\frac{s_{ij}^{n+1}-\bar{s}_{ij}^{n}}{\Delta t}+\boldsymbol{\nabla}_h(\bar{\boldsymbol{D}}_p\boldsymbol{\nabla}_h s)_{ij}^{n+1}=(\tilde{G}_s)_{ij}-\left(\frac{\partial f}{\partial c}\right)_{ij}^{n}\left(\mathbf{v}_{ij}^{n}\cdot\boldsymbol{\nabla}_h c_{ij}^{n}\right), \tag{3.35a}$$

$$\phi\frac{c_{ij}^{n+1}-\bar{c}_{ij}^{n}}{\Delta t}+(\tilde{G})_{ij}^{n}c_{ij}^{n+1}=(\tilde{G}_c)_{ij}^{n}. \tag{3.35b}$$

Here, $\bar{s}_{ij}^{n}=c(\bar{\mathbf{x}}_{ij}^{s},t^{n})$ and $\bar{c}_{ij}^{n}=c(\bar{\mathbf{x}}_{ij}^{c},t^{n})$ are computed using approximate values of $\bar{\mathbf{x}}_{ij}^{s}$ and $\bar{\mathbf{x}}_{ij}^{c}$ respectively, given by

$$\begin{aligned}\bar{\mathbf{x}}_{ij}^{s}&=\mathbf{x}_{ij}^{s}-\frac{\partial f}{\partial s}(s_{ij}^{n},c_{ij}^{n})\,\mathbf{v}_{ij}^{n}\,\Delta t/\phi,\\ \bar{\mathbf{x}}_{ij}^{c}&=\mathbf{x}_{ij}^{c}-\left(\left(\frac{f}{s}\right)(s_{ij}^{n},c_{ij}^{n})\mathbf{v}+\left(\frac{\boldsymbol{D}_p}{s}\right)(\bar{s}_{ij}^{n},c_{ij}^{n})\boldsymbol{\nabla}s\right)\Delta t/\phi,\end{aligned}$$

where, the superscripts ‘s’ and ‘c’ are used to denote the characteristic curves associated with the water transport eq. (3.34a) and the polymer transport eq. (3.34b) respectively. Also, as before, $(\bar{\mathbf{x}}_{ij}^{s},t^{n})$ and $(\mathbf{x}_{ij}^{s},t^{n+1})$ lie on the same characteristic curve of the water transport equation while $(\bar{\mathbf{x}}_{ij}^{c},t^{n})$ and $(\mathbf{x}_{ij}^{c},t^{n+1})$ lie on the same characteristic curve of the polymer transport equation. Also,

$$\begin{aligned}\bar{\boldsymbol{D}}_{p_{(ij)}}^{\ n}&=\boldsymbol{D}_p(\bar{s}_{ij}^{n},c_{ij}^{n}),\\ \boldsymbol{\nabla}_h(\bar{\boldsymbol{D}}_p\nabla_h s)_{ij}^{n+1}&=\bar{\boldsymbol{D}}_{p_{(i+1/2,j)}}\frac{s_{i+1,j}^{n+1}-s_{i,j}^{n+1}}{\Delta x^2}-\bar{\boldsymbol{D}}_{p_{(i-1/2,j)}}\frac{s_{i,j}^{n+1}-s_{i-1,j}^{n+1}}{\Delta x^2}\\ &\quad+\bar{\boldsymbol{D}}_{p_{(i,j+1/2)}}\frac{s_{i,j+1}^{n+1}-s_{i,j}^{n+1}}{\Delta y^2}-\bar{\boldsymbol{D}}_{p_{(i,j-1/2)}}\frac{s_{i,j}^{n+1}-s_{i,j-1}^{n+1}}{\Delta y^2},\\ \bar{\boldsymbol{D}}_{p_{(i\pm1/2,j)}}&=\frac{\boldsymbol{D}_p(\bar{s}_{i\pm1,j}^{n},c_{i\pm1,j}^{n})+\boldsymbol{D}_p(\bar{s}_{i,j}^{n},c_{i,j}^{n})}{2},\\ \bar{\boldsymbol{D}}_{p_{(i,j\pm1/2)}}&=\frac{\boldsymbol{D}_p(\bar{s}_{i,j\pm1}^{n},c_{i,j\pm1}^{n})+\boldsymbol{D}_p(\bar{s}_{i,j}^{n},c_{i,j}^{n})}{2}.\end{aligned}$$

Hence eqs. (3.35a) and (3.35b) give the MMOC based finite difference approximation of the transport system for the one-component two-phase flow (polymer flooding) problem

given by eqs. (2.18a) and (2.18b).

3.2 Algorithm

Here we outline the algorithm for the SP flood simulation. The algorithm for the polymer flood is essentially a special case of the same. The step-by-step algorithm is given as follows:

1. Define the Cartesian grid in the domain using equal, uniform grid sizes in both the axes. Generate the finite element mesh.

2. Generate a heterogeneity field on this grid.

3. Choose an initial interface separating the injected fluid from the resident fluid.

4. Set the model parameters: μ_o, μ_w, $s_{ro}^{\sigma 0}$, $s_{ra}^{\sigma 0}$.

5. Initialize the state variables s, c and Γ as

$$(s, c, \Gamma)(\mathbf{x}, 0) = \begin{cases} (1 - s_{ro}^{\sigma 0}, c_0, \Gamma_0) & x \in \Omega^+ \\ (s_0^{\sigma 0}, 0, 0) & x \in \Omega^- \end{cases}, \qquad .$$

6. Calculate $\sigma(s^n, \Gamma^n)$, $\mu_a(c^n)$, $s_{ra}(s^n, \Gamma^n)$, $s_{ro}(s^n, \Gamma^n)$, $\lambda_a(s^n, c^n, \Gamma^n)$, $\lambda_o(s^n, \Gamma^n)$, $\lambda(s^n, c^n, \Gamma^n)$ using s^n, c^n, Γ^n which are values of s, c and Γ respectively at the n^{th} time level.

7. Solve the global pressure equation to get p^n and subsequently compute $\mathbf{v}^n$.

8. Use $\mathbf{v}^n$, s^n, c^n, Γ^n and the quantities calculated in Step 6, to solve for s^{n+1}, c^{n+1} and Γ^{n+1}, thus completing a full time step.

9. If breakthrough is achieved: then stop; else update $n = n + 1$ and repeat from Step 6.

In order to speed up computation, sometimes a few iterations of Steps 6 and 8 are done before updating the pressure in Step 7. The pseudocode (see Algorithm 1) and flow-chart (see Figure 3.7) for the procedure are given below.

Algorithm 1: SP flooding simulation

```
/* Set up Cartesian grid, FE Mesh, permeability field and
model parameters                                          */
```

1 Set $i, j = 0, \ldots, M$; $\mathbf{x}_{ij} = \left(\frac{i}{M}, \frac{j}{M}\right)$; /* ($M \times M$ is the grid size) */

2 Set $\Sigma =$ *Initial interface*; /* $\Sigma = \partial\Omega^+ \cap \partial\Omega^-$ */

3 Set $\mathbf{K}(\mathbf{x}) =$ *chosen permeability field data*;

4 Set μ_o, μ_w, $s_{ro}^{\sigma 0}$, $s_{ra}^{\sigma 0}$, $s_0^{\sigma 0}$, $\tilde{q} =$ *values from Table 4.6*;

```
/* Initialization                                            */
```

5 Set $t = 0$; $\Delta t = \frac{1}{N}$; $Tstop = 100N\Delta t$; /* N chosen for accuracy */

6 **for** i = 0, . . . , M **do**

7 **for** j = 0, . . . , M **do**

8 Set $(s,\ c,\ \Gamma)(\mathbf{x}_{ij}, 0) = \begin{cases} (1 - s_{ro}^{\sigma 0}, c_0, \Gamma_0) & \mathbf{x}_{ij} \in \Omega^+ \\ (s_0^{\sigma 0}, 0, 0) & \mathbf{x}_{ij} \in \Omega^- \end{cases}$;

9 **end**

10 **end**

```
/* Computation loop                                          */
```

11 **while** $(s(\mathbf{x}_{M,M}, t) \leq 1 - s_0^{\sigma 0} \ \ and \ \ t < Tstop)$ **do**

12 Compute $\{\sigma,\ \mu_a,\ s_{ra},\ s_{ro},\ \lambda_a,\ \lambda_o,\ \lambda,\ p_c\}$ using $(s^n, c^n, \Gamma^n, \mathbf{v}^{n-1})$;

13 Solve global pressure equation for $p^n, \mathbf{v}^n$;

14 Recompute $\{s_{ra},\ s_{ro},\ \lambda_a,\ \lambda_o,\ \lambda\}$ using $(s^n, c^n, \Gamma^n, \mathbf{v}^n)$;

15 Solve transport equations for s^{n+1}, c^{n+1} and Γ^{n+1};

16 Set $t = t + \Delta t$;

17 **end**

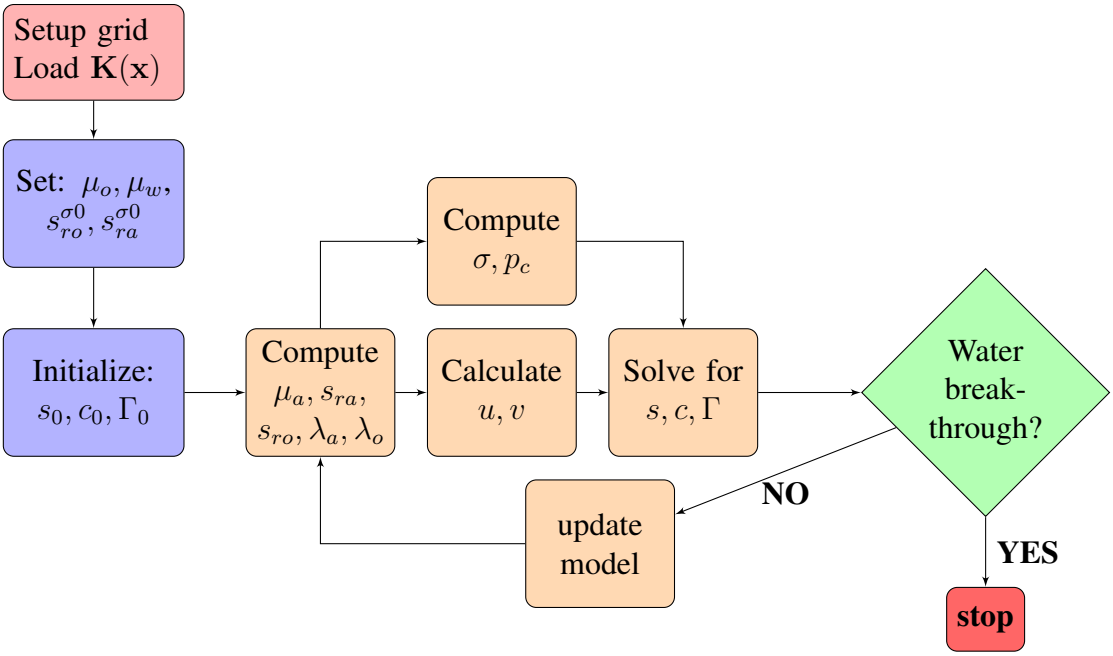

Figure 3.7: Flow-chart for SP flooding simulation

3.3 Convergence Study and Error Analysis

In this section, we present a convergence analysis of the hybrid numerical method introduced in section 3.1 for solving the flow and transport equations governing multi-component, two-phase porous media flows. The hybrid method consists of a discontinuos finite element method and a time implicit finite difference method based on the MMOC. We study the convergence behavior of the MMOC procedure to solve the system of transport equations. For the complete analysis of the flow and transport system, we assume an optimal order estimate for the L^∞ norm of the pressure gradient obtained from the discontinuous finite element method and obtain L^2 error estimates for the individual variables of the multicomponent transport system. The basic analysis has been performed on a one-component two-phase flow model that represents polymer flooding in one spatial dimension. We present the details below.

Let $s_i^n = s(x_i, t^n)$ be the grid values of the actual solution of the saturation equation (2.18a) and $w_i^n = w(x_i, t^n)$ be the grid values of the numerical solution obtained from eq. (3.35a) where $x_i = ih$ and $t^n = n\Delta t$. Similarly, let p_i^n and r_i^n be the grid values of the actual and the numerical solutions respectively obtained from eq. (2.18c) and eq. (3.16). Also, let c_i^n and m_i^n be the grid values of the actual and the numerical solutions respectively of eq. (2.18b) and eq. (3.35b). Finally, let v_i^n and z_i^n be the grid values of the actual and the numerical solutions respectively of the total velocity given by $\mathbf{v} = -\mathbf{K}\lambda\boldsymbol{\nabla}p$. The errors in the numerical approximation are defined as follows.

$$\zeta_i^n = s_i^n - w_i^n, \quad \pi_i^n = p_i^n - r_i^n, \quad \& \quad \theta_i^n = c_i^n - m_i^n.$$

We define the following discrete norms for any $u \in W^{l,p}(\Omega)$, $v \in L^2(\Omega)$ and $w \in L^\infty(\Omega)$ where $\Omega = [0,1]^2$.

$$\|u\|_{l,p} = \left(\sum_{k=0}^{l}\left(\sum_i h\left|\frac{d^k u_i}{dx^k}\right|^p\right)\right)^{1/p}, \quad |u|_{l,p} = \left(\sum_i h\left|\frac{d^l u_i}{dx^l}\right|^p\right)^{1/p}$$
$$\|v\| = \left(\sum_i h|v_i|^2\right)^{1/2}, \qquad \|w\|_\infty = \max_i |w_i|$$

In particular, $\|.\|$ and $\langle .\rangle$ denote the discrete L^2 norm and the associated inner product respectively. With slight abuse of notation we use $\boldsymbol{D}$ instead of $\boldsymbol{D}_p$ and recall the one-component two-phase flow model below

$$\phi\frac{\partial s}{\partial t} + \frac{\partial f}{\partial s}\mathbf{v}\cdot\boldsymbol{\nabla}s + \boldsymbol{\nabla}\cdot(\boldsymbol{D}\boldsymbol{\nabla}s) = \tilde{G}_s - \frac{\partial f}{\partial c}\mathbf{v}\cdot\boldsymbol{\nabla}c, \tag{3.36a}$$
$$\phi\frac{\partial c}{\partial t} + \left(\frac{f}{s}\mathbf{v} + \frac{\boldsymbol{D}}{s}\boldsymbol{\nabla}s\right)\cdot\boldsymbol{\nabla}c + c\tilde{G} = \tilde{G}_c, \tag{3.36b}$$

where $\boldsymbol{D}(s,c) = \mathbf{K}(\mathbf{x})\lambda_o(s)f(s,c)\frac{dp_c(s)}{ds}$, $\tilde{G}_s = (1-f)Q\delta(\mathbf{x}-\mathbf{x}^i)$, $\tilde{G} = \frac{Q}{s}\delta(\mathbf{x}-\mathbf{x}^i)$ and

$\tilde{G}_c = \frac{c^i Q}{s}\delta(\mathbf{x} - \mathbf{x}^i)$. For the analysis, we consider the corresponding system of equations (see eqs. (3.36a) and (3.36b) above) in one spatial dimension as given by

$$\phi\frac{\partial s}{\partial t} + b\frac{\partial s}{\partial x} + \frac{\partial}{\partial x}\left(D\frac{\partial s}{\partial x}\right) = F, \qquad s(x,0) = s_0(x); \quad x \in \Omega \setminus \partial\Omega \tag{3.37a}$$

$$\phi\frac{\partial c}{\partial t} + a\frac{\partial c}{\partial x} + Gc = H, \qquad c(x,0) = c_0(x); \quad x \in \Omega \setminus \partial\Omega \tag{3.37b}$$

where $b(s,c) = \frac{\partial f}{\partial s}v$, $a(s,c) = (\frac{f}{s}v + \frac{D}{s}\frac{\partial s}{\partial x})$, $F = \tilde{G}_s - v\frac{\partial f}{\partial c}\frac{\partial c}{\partial x}$, $G = \tilde{G}$ and $H = \tilde{G}_c$. Then the characteristic finite difference approximation of Eq. (3.37a) and Eq. (3.37b) are given by

$$\phi_i\frac{w_i^n - \bar{w}_i^{n-1}}{\Delta t} + \delta_x(\bar{D}\delta_x w^n)_i = F_i^n \qquad w_i^0 = s_0(x_i), \tag{3.38}$$

$$\phi_i\frac{m_i^n - \bar{m}_i^{n-1}}{\Delta t} + G_i^n m_i^n = H_i^n \qquad m_i^0 = c_0(x_i), \tag{3.39}$$

$$\text{where } \bar{w}_i^{n-1} = w(\tilde{x}_i^s, t^{n-1}), \quad \tilde{x}_i^s = x_i - b(w_i^{n-1}, m_i^{n-1})\Delta t/\phi_i, \tag{3.40}$$

$$\text{and } \bar{m}_i^{n-1} = m(\tilde{x}_i^c, t^{n-1}), \quad \tilde{x}_i^c = x_i - a(w_i^n, m_i^{n-1})\Delta t/\phi_i. \tag{3.41}$$

From Eq. (3.37a) and Eq. (3.38) we have the following

$$\psi_s\frac{\partial s}{\partial \tau} + \frac{\partial}{\partial x}\left(D\frac{\partial s}{\partial x}\right) = F(s^n, c^n), \qquad s(x,0) = s_0(x), \tag{3.42a}$$

$$\phi_i\frac{w_i^n - \bar{w}_i^{n-1}}{\Delta t} + \delta_x(\bar{D}\delta_x w^n)_i = F(w_i^n, m_i^n) \qquad w_i^0 = s_0(x_i). \tag{3.42b}$$

In the following analysis M, $\tilde{M}$, $\hat{M}$, $M_k(k \in \mathbb{Z}^+)$ and C are generic constants independent of the time step and space discretizations Δt and h respectively. We will also assume the following bounds on the porosity, $\phi_* \leq \phi(x) \leq \phi^*$. For the rest of the analysis of the water saturation equation (3.42b), with slight abuse of notation, we will write $\tilde{x}_i^n$ and $\bar{x}_i^n$ to mean $\tilde{x}_i^{s,n}$ and $\bar{x}_i^{s,n}$ respectively. In the next two lemmas we estimate the errors introduced by

approximating the derivative in the characteristic direction and the second order derivative term in eq. (3.42a) with their finite difference discretizations given in eq. (3.42b).

Lemma 3.3.1 *The error in approximating the characteristic derivative in eq.* (3.42a) *is given by*

$$\psi_{s,i}\left(\frac{\partial s}{\partial \tau}\right)_i^n - \phi_i \frac{s_i^n - \bar{s}_i^{n-1}}{\Delta t} = O\left(\left|\frac{\partial^2 s^*}{\partial \tau^2}\right| \Delta\tau\right),$$

where $\bar{s}_i^{n-1} = s(\bar{x}_i, t^{n-1})$ with $\bar{x}_i = x_i - b(s_i^n, c_i^n)\Delta t/\phi_i$.

Proof. Let $p_1 = (x, t^n)$ be a point on the grid (see Figure 3.6) and the characteristic that passes through this point intersects the previous time level at $p_2 = (\bar{x}, t^{n-1})$ where $\bar{x} = x - b(s,c)/\phi(x)\Delta t$ and let $\Delta\tau = \left[(x-\bar{x})^2 + (t^n - t^{n-1})^2\right]^{1/2}$. Hence $\Delta\tau = \frac{\psi_s}{\phi}\Delta t$. Using the Taylor series expansion along the characteristic direction, we write

$$s(p_1 - \Delta\tau) = s(p_1) - \Delta\tau\frac{\partial s}{\partial \tau} + \frac{\Delta\tau^2}{2}\frac{\partial^2 s^*}{\partial \tau^2},$$

where $\frac{\partial^2 s^*}{\partial \tau^2}$ is some evaluation of the second derivative along the characteristic segment between p_2 and p_1. In the convection dominated case, this second derivative is relatively much smaller than $\frac{\partial^2 s}{\partial x^2}$ or $\frac{\partial^2 s}{\partial t^2}$ [55]. This is rewritten as

$$\Delta\tau\frac{\partial s^n}{\partial \tau} = s^n - \bar{s}^{n-1} + \frac{\Delta\tau^2}{2}\frac{\partial^2 s^*}{\partial \tau^2}.$$

Using $\dfrac{\psi_s}{\Delta\tau} = \dfrac{\phi}{\Delta t}$ we obtain

$$\psi_s\frac{\partial s^n}{\partial \tau} - \phi\frac{s^n - \bar{s}^{n-1}}{\Delta t} = \frac{\phi}{\Delta t}\frac{\Delta\tau^2}{2}\frac{1}{2}\frac{\partial^2 s^*}{\partial \tau^2} = \frac{\psi_s}{\Delta\tau}\frac{\Delta\tau^2}{2}\frac{\partial^2 s^*}{\partial \tau^2} = \frac{\psi_s}{2}\Delta\tau\frac{\partial^2 s^*}{\partial \tau^2}.$$

This leads to the final result:

$$\psi_{s,i}\left(\frac{\partial s}{\partial \tau}\right)_i^n - \phi_i\frac{s_i^n - \bar{s}_i^{n-1}}{\Delta t} = O\left(\left|\frac{\partial^2 s^*}{\partial \tau^2}\right| \Delta\tau\right). \quad \blacksquare$$

Using Lemma 3.3.1 in Eq. (3.42a), we estimate the error introduced by numerical dis-

cretization of the characteristic derivative as

$$\phi_i \frac{s_i^n - \bar{s}_i^{n-1}}{\Delta t} + \frac{\partial}{\partial x}\left(D\frac{\partial s^n}{\partial x}\right)_i = F(s_i^n, c_i^n) + O\left(\left|\frac{\partial^2 s^*}{\partial \tau^2}\right| \Delta\tau\right). \tag{3.43}$$

Now we estimate the approximation error for the second order derivative term in the left hand side of Eq. (3.42a). By definition,

$$\begin{aligned}\delta_x(\bar{D}\delta_x w^n)_i &= \frac{1}{h}\left(\bar{D}_{i+1/2}(\delta_x w^n)_{i+1/2} - \bar{D}_{i-1/2}(\delta_x w^n)_{i-1/2}\right) \\ &= \frac{1}{h^2}\left(\bar{D}_{i+1/2}(w_{i+1}^n - w_i^n) - \bar{D}_{i-1/2}(w_i^n - w_{i-1}^n)\right),\end{aligned} \tag{3.44}$$

where

$$\bar{D}_{i+1/2} = \frac{1}{2}\left[D(x_i, \bar{w}_i^{n-1}) + D(x_{i+1}, \bar{w}_{i+1}^{n-1})\right] \quad \& \quad \bar{D}_{i-1/2} = \frac{1}{2}\left[D(x_i, \bar{w}_i^{n-1}) + D(x_{i-1}, \bar{w}_{i-1}^{n-1})\right].$$

The numerical approximation of the second order derivative in Eq. (3.37a) is given by

$$\delta_x(D\delta_x s^n)_i = \frac{1}{h^2}\left[D_{i+1/2}(s_{i+1}^n - s_i^n) - D_{i-1/2}(s_i^n - s_{i-1}^n)\right],$$

where

$$D_{i+1/2} = \frac{1}{2}\left[D(x_i, s_i^n) + D(x_{i+1}, s_{i+1}^n)\right] \quad \& \quad D_{i-1/2} = \frac{1}{2}\left[D(x_i, s_i^n) + D(x_{i-1}, s_{i-1}^n)\right].$$

Lemma 3.3.2 *The finite difference approximation error of the second derivative term in eq.* (3.42a) *is given by*

$$\frac{d}{dx}\left(D\frac{d}{dx}s^n\right)_i - \delta_x(D\delta_x s^n)_i = O(h\|s^n\|_{3,\infty}).$$

Proof. From the Taylor series expansion, we know that

$$\left(\frac{du}{dx}\right) - \frac{u(x+h/2) - u(x-h/2)}{h} = O\left(h^2\|u\|_{3,\infty}\right).$$

This can be rewritten as

$$\left(\frac{du}{dx}\right)_i - \delta_x(u_i) = O(h^2\|u\|_{3,\infty}).$$

Using this estimate for the second derivative term, we obtain

$$\frac{d}{dx}\left(D\frac{d}{dx}s^n\right)_i - \delta_x(D\delta_x s^n)_i = O\left(h^2\left\|D\frac{d}{dx}s^n\right\|_{3,\infty}\right).$$

Using the defintion (3.44), we obtain

$$\frac{d}{dx}\left(D\frac{d}{dx}s^n\right)_i - \frac{1}{h}\left(\left(D\frac{ds^n}{dx}\right)_{i+1/2} - \left(D\frac{ds^n}{dx}\right)_{i-1/2}\right) = O\left(h^2\left\|D\frac{d}{dx}s^n\right\|_{3,\infty}\right).$$

Using $\left(D\frac{ds^n}{dx}\right)_{i+1/2} = D_{i+1/2}\left(\frac{ds^n}{dx}\right)_{i+1/2} = D_{i+1/2}\left(\frac{s^n_{i+1}-s^n_i}{h}\right) + O\left(h^2\|s^n\|_{3,\infty}\right)$,
we continue as

$$\frac{d}{dx}\left(D\frac{d}{dx}s^n\right)_i - \frac{1}{h}\left[D_{i+1/2}\frac{s^n_{i+1}-s^n_i}{h}O(h^2\|s^n\|_{3,\infty})\right] + \frac{1}{h}\left[D_{i-1/2}\frac{s^n_i - s^n_{i-1}}{h} + O(h^2\|s^n\|_{3,\infty})\right] = O\left(h^2\|D\|_\infty\left\|\frac{ds^n}{dx}\right\|_{3,\infty}\right).$$

This leads to the final estimate

$$\frac{d}{dx}\left(D\frac{d}{dx}s^n\right)_i - \frac{1}{h}\left[D_{i+1/2}\frac{s^n_{i+1}-s^n_i}{h} - D_{i-1/2}\frac{s^n_i - s^n_{i-1}}{h}\right] = O(h\|s^n\|_{3,\infty}) + O(h^2\|s^n\|_{4,\infty}) = O(h\|s^n\|_{3,\infty}). \quad \blacksquare$$

Using the result of Lemma 3.3.2, we rewrite Eq. (3.43) as

$$\phi_i\frac{s^n_i - \bar{s}^{n-1}_i}{\Delta t} + \delta_x(D\delta_x s^n)_i = F(s^n_i, c^n_i) + O\left(\left|\frac{\partial^2 s^*}{\partial\tau^2}\right|\Delta\tau\right) + O(h\|s^n\|_{3,\infty}). \tag{3.45}$$

Subtracting Eq. (3.42b) from Eq. (3.45), we obtain

$$\phi_i\frac{s^n_i - \bar{s}^{n-1}_i}{\Delta t} - \phi_i\frac{w^n_i - \bar{w}^{n-1}_i}{\Delta t} + \delta_x(D\delta_x s^n)_i - \delta_x(\bar{D}\delta_x w^n)_i = F(s^n_i, c^n_i) - F(w^n_i, m^n_i) + O\left(\left|\frac{\partial^2 s^*}{\partial\tau^2}\right|\Delta\tau, h\|s^n\|_{3,\infty}\right).$$

Recall that we define the numerical error in saturation as $\zeta_i^n = s_i^n - w_i^n$. Using the definition of ζ_i^n and rearranging terms, we rewrite the above as

$$\phi_i \frac{\zeta_i^n - (\bar{s}_i^{n-1} - \bar{w}_i^{n-1})}{\Delta t} - \delta_x(\bar{\mathscr{D}}\delta_x\zeta^n)_i = F(s_i^n, c_i^n) - F(w_i^n, m_i^n) + O\left(\left|\frac{\partial^2 s^*}{\partial \tau^2}\right| \Delta\tau, h\|s^n\|_{3,\infty}\right) - \delta_x((\bar{\mathscr{D}} - \mathscr{D})\delta_x s^n)_i \,. \quad (3.46)$$

In the above, the capillary dissipation coefficients D and $\bar{D}$ have been replaced with $\mathscr{D}$ and $\bar{\mathscr{D}}$ respectively and the signs associated with the terms have been reversed. This is because the definition of capillary pressure, given in Eq. (2.4), ensures that $\frac{dp_c}{ds} \leq 0$ which implies that $D, \bar{D} \leq 0$. Hence, in Eq. (3.46) and in the rest of the analysis of the water transport equation (3.42b), we will use $\mathscr{D}$ and $\bar{\mathscr{D}}$ to denote the absolute values of the capillary dissipation coefficients D and $\bar{D}$ respectively. We assume that these will be bounded by $D_* \leq \mathscr{D}, \bar{\mathscr{D}} \leq D^*$.

Consider the first term on the left hand side of Eq. (3.46). Let $\zeta^n = \mathscr{I}\zeta_i^n$ be the piecewise linear interpolant of ζ_i^n such that $\bar{\zeta}_i^{n-1} = \mathscr{I}\zeta^{n-1}(\tilde{x}_i) = \mathscr{I}s^{n-1}(\tilde{x}_i) - w^{n-1}(\tilde{x}_i) = \mathscr{I}s^{n-1}(\tilde{x}_i) - \bar{w}_i^{n-1}$. Then,

$$\begin{aligned}\zeta_i^n - (\bar{s}_i^{n-1} - \bar{w}_i^{n-1}) &= (\zeta_i^n - \bar{\zeta}_i^{n-1}) + \mathscr{I}s^{n-1}(\tilde{x}_i) - \bar{w}_i^{n-1} - \bar{s}_i^{n-1} + \bar{w}_i^{n-1} \\ &= (\zeta_i^n - \bar{\zeta}_i^{n-1}) - \underbrace{(s^{n-1}(\bar{x}_i) - s^{n-1}(\tilde{x}_i))}_{\text{A}} - \underbrace{((1 - \mathscr{I})s^{n-1}(\tilde{x}_i))}_{\text{B}} \,. \end{aligned} \quad (3.47)$$

Below, we find estimates for the last two terms, A and B, of the right hand side of Eq. (3.47), followed by the estimate of the source term $(F(s_i^n, c_i^n) - F(w_i^n, m_i^n))$ on the right hand side of Eq. (3.46). Once we have these estimates, we can substitute Eq. (3.47) in Eq. (3.46), take inner products with ζ_i^n and use the estimates to rewrite the equation.

A. Estimate of the term A on the right hand side of Eq. (3.47): This is carried out in

several steps below.

$$
\begin{aligned}
& s^{n-1}(\bar{x}_1) - s^{n-1}(\tilde{x}_i) \\
& \leq \hat{M}\|s^{n-1}\|_{1,\infty} |\bar{x}_i - \tilde{x}_i| \qquad (\hat{M} \text{ is a constant }) \\
& = \hat{M}\|s^{n-1}\|_{1,\infty} \left| \frac{\partial f}{\partial s}(w_i^{n-1}, m_i^{n-1}) z_i^{n-1} - \frac{\partial f}{\partial s}(s_i^n, c_i^n) v_i^n \right| \frac{\Delta t}{\phi_i} \\
& \leq \hat{M}\|s^{n-1}\|_{1,\infty} \left(\left| \frac{\partial f}{\partial s}(w_i^{n-1}, m_i^{n-1}) \right| \underbrace{|z_i^{n-1} - v_i^n|}_{\text{A-1}} \right. \\
& \qquad \left. + |v_i^n| \underbrace{\left| \frac{\partial f}{\partial s}(w_i^{n-1}, m_i^{n-1}) - \frac{\partial f}{\partial s}(s_i^n, c_i^n) \right|}_{\text{A-2}} \right) \frac{\Delta t}{\phi_i}. \qquad (3.48)
\end{aligned}
$$

Next we estimate the terms A-1 and A-2 of the right hand side of (3.48).

A-1. Estimate of the term A-1 on the right hand side of Eq. (3.48):

We rewrite the term A-1 as

$$
|z_i^{n-1} - v_i^n| \leq \underbrace{|z_i^{n-1} - v_i^{n-1}|}_{\text{A-1-1}} + \underbrace{|v_i^n - v_i^{n-1}|}_{\text{A-1-2}} \qquad (3.49)
$$

Recall that $z_i^n = -K\lambda(w_i^n, m_i^n)\frac{\partial r_i^n}{\partial x}$ and $v_i^n = -K\lambda(s_i^n, c_i^n)\frac{\partial p_i^n}{\partial x}$. Then the first term A-1-1 on the right hand side of the above inequality (3.49) is written as

$$
\begin{aligned}
& |z_i^{n-1} - v_i^{n-1}| \\
= & \left| K\lambda(w_i^{n-1}, m_i^{n-1}) \frac{\partial}{\partial x}(p_i^{n-1} - r_i^{n-1}) \quad + K\left(\lambda(s_i^{n-1}, c_i^{n-1}) - \lambda(w_i^{n-1}, m_i^{n-1})\right) \frac{\partial p_i^{n-1}}{\partial x} \right| \\
\leq & \|K\|_\infty \|\lambda\|_\infty \left\| \frac{\partial}{\partial x}(\pi_i^{n-1}) \right\|_\infty \quad + \|K\|_\infty \left|\lambda(s_i^{n-1}, c_i^{n-1}) - \lambda(w_i^{n-1}, m_i^{n-1})\right| \left\| \frac{\partial}{\partial x}(p_i^{n-1}) \right\|_\infty .
\end{aligned} \qquad (3.50)
$$

The non-traditional discontinuous finite element method adopted here for solving the pres-

sure equation gives us the following estimates [82],

$$\left\| \frac{\partial \pi^n}{\partial x} \right\|_\infty = O(h). \tag{3.51}$$

The numerical scheme will still converge if a different finite element formulation is used as long as it preserves or improves upon the above error estimate. Using Taylor series we write,

$$\begin{aligned} &\left|\lambda(s_i^{n-1}, c_i^{n-1}) - \lambda(w_i^{n-1}, m_i^{n-1})\right| && (3.52)\\ &\quad \leq \left|s_i^{n-1} - w_i^{n-1}\right| \left\| \frac{\partial \lambda}{\partial s} \right\|_\infty + \left|c_i^{n-1} - m_i^{n-1}\right| \left\| \frac{\partial \lambda}{\partial c} \right\|_\infty \\ &\quad \leq \bar{M}(\left|\zeta_i^{n-1}\right| + \left|\theta_i^{n-1}\right|). && (3.53) \end{aligned}$$

Using Eq. (3.51) and Eq. (3.53) in Eq. (3.50), we obtain following estimate for the first term A-1-1 of the righthand side of (3.49).

$$|z_i^{n-1} - v_i^{n-1}| \leq M(h + |\zeta_i^{n-1}| + |\theta_i^{n-1}|). \tag{3.54}$$

To estimate the term A-1-2 of the inequality (3.49) we observe

$$|v_i^n - v_i^{n-1}| \leq \Delta t \left\| \frac{\partial v}{\partial t} \right\|_\infty. \tag{3.55}$$

Using Eq. (3.54) and Eq. (3.55) in (3.49), we obtain the following estimate for A-1 (see Eq. (3.48)).

$$|z_i^{n-1} - v_i^n| \leq M(h + \Delta t + |\zeta_i^{n-1}| + |\theta_i^{n-1}|). \tag{3.56}$$

This concludes the estimate for the term A-1 in Eq. (3.48).

A-2. Estimate of the term A-2 on the right hand side of Eq. (3.48):

$$\begin{aligned}
&\left|\frac{\partial f}{\partial s}(w_i^{n-1}, m_i^{n-1}) - \frac{\partial f}{\partial s}(s_i^n, c_i^n)\right| \\
&\leq \left|(w_i^{n-1} - s_i^{n-1})\right| \left\|\frac{\partial^2 f}{\partial s^2}\right\|_\infty + \left|m_i^{n-1} - c_i^{n-1}\right| \left\|\frac{\partial^2 f}{\partial c\, \partial s}\right\|_\infty \\
&\qquad + \left|s_i^{n-1} - s_i^n\right| \left\|\frac{\partial^2 f}{\partial s^2}\right\|_\infty \left\|\frac{\partial s}{\partial t}\right\|_\infty + \left|c_i^{n-1} - c_i^n\right| \left\|\frac{\partial^2 f}{\partial c\, \partial s}\right\|_\infty \left\|\frac{\partial c}{\partial t}\right\|_\infty \\
&\leq M(|\zeta_i^{n-1}| + |\theta_i^{n-1}| + \Delta t). \qquad (3.57)
\end{aligned}$$

Using the estimates for A-1 and A-2, as given by Eq. (3.56) and Eq. (3.57) respectively, in Eq. (3.48) we finally obtain the estimate for the term A of Eq. (3.47) as

$$|s^{n-1}(\bar{x}_i) - s^{n-1}(\tilde{x}_i)| \leq M\Delta t(|\zeta_i^{n-1}| + |\theta_i^{n-1}| + h + \Delta t). \qquad (3.58)$$

B. Estimate of the term B on the right hand side of Eq. (3.47):

Using the Peano kernel Theorem in the spirit of the paper by Douglas and Russel [55], we obtain the following,

$$(1 - \mathscr{I})s^{n-1}(\tilde{x}_i) = O\left(h^2 \left\|s^{n-1}\right\|_{2,\infty}\right). \qquad (3.59)$$

C. Estimate of the source term $(F(s_i^n, c_i^n) - F(w_i^n, m_i^n))$ **in Eq.** (3.46):

$$\begin{aligned}
F(s_i^n, c_i^n) - F(w_i^n, m_i^n) &\leq |s_i^n - w_i^n| \left\|\frac{\partial F}{\partial s}\right\|_\infty + |c_i^n - m_i^n| \left\|\frac{\partial F}{\partial c}\right\|_\infty \\
&\leq M(|\zeta_i^n| + |\theta_i^n|). \qquad (3.60)
\end{aligned}$$

Equation (3.47) is substituted into Eq. (3.46) and the resulting equation is tested against ζ_i^n. Using the estimates (3.58), (3.59) and (3.60) to replace some of the inner products, we

rewrite Eq. (3.46) as

$$\underbrace{\langle \phi_i \frac{\zeta_i^n - \bar{\zeta}_i^{n-1}}{\Delta t}, \zeta_i^n \rangle}_{\text{D-1}} - \underbrace{\langle \delta_x(\bar{\mathscr{D}}\delta_x \zeta^n)_i, \zeta_i^n \rangle}_{\text{D-2}} \leq \langle M\left(h + \Delta t + h^2/\Delta t\right), \zeta_i^n \rangle$$
$$+ \langle M\left(|\zeta_i^{n-1}| + |\theta_i^{n-1}| + |\zeta_i^n| + |\theta_i^n|\right), \zeta_i^n \rangle + \underbrace{\langle \epsilon_i^n, \zeta_i^n \rangle}_{\text{D-3}} - \underbrace{\langle \delta_x((\bar{\mathscr{D}} - \mathscr{D})\delta_x s^n)_i, \zeta_i^n \rangle}_{\text{D-4}} \tag{3.61}$$

where $\epsilon_i^n = O(\|\frac{\partial^2 s}{\partial \tau^2}\|_\infty \Delta\tau, \|s^n\|_{3,\infty} h)$. Below, we obtain the estimates for the terms D-1, D-2, D-3 and D-4 in order to rewrite Eq. (3.61) in terms of only the errors ζ and θ.

D-1. Estimate of the term D-1: The inner product is rewritten as

$$\langle \phi_i \frac{\zeta_i^n - \bar{\zeta}_i^{n-1}}{\Delta t}, \zeta_i^n \rangle = \underbrace{\langle \phi_i \frac{\zeta_i^n - \zeta_i^{n-1}}{\Delta t}, \zeta_i^n \rangle}_{\text{D-1-1}} - \langle \phi_i \frac{\bar{\zeta}_i^{n-1} - \zeta_i^{n-1}}{\Delta t}, \zeta_i^n \rangle$$

Using the inequality $|a-b||a| \geq \frac{|a|^2 - |b|^2}{2}$ we estimate the term D-1-1 as

$$\langle \phi_i \frac{\zeta_i^n - \zeta_i^{n-1}}{\Delta t}, \zeta_i^n \rangle \geq \frac{M}{\Delta t}(\|\zeta^n\|^2 - \|\zeta^{n-1}\|^2)$$

D-2. Estimate of the term D-2 in Eq. (3.61):

Using summation by parts, we write

$$\langle \delta_x(\bar{\mathscr{D}}\delta_x \zeta^n)_i, \zeta_i^n \rangle = -\langle (\bar{\mathscr{D}}\delta_x \zeta^n)_i, (\delta_x \zeta^n)_i \rangle$$

and similarly for D-4, we have

$$\langle \delta_x((\bar{\mathscr{D}} - \mathscr{D})\delta_x s^n)_i, \zeta_i^n \rangle = -\langle ((\bar{\mathscr{D}} - \mathscr{D})\delta_x s^n)_i, (\delta_x \zeta^n)_i \rangle.$$

D-3. Estimate of the term D-3 in Eq. (3.61): Finally testing the term D-3 against ζ_i^n, we get

$$\langle \epsilon_i^n, \zeta_i^n \rangle \leq M(h + \Delta t) \sum_i h|\zeta_i^n| \leq M(h^2 + \Delta t^2 + \|\zeta^n\|^2)$$

Substituting the estimates for the term D-1-1 and replacing the terms D-2, D-3 and D-4 as shown before, we rewrite Eq. (3.61) as

$$\frac{M}{\Delta t}(\|\zeta^n\|^2 - \|\zeta^{n-1}\|^2) + \underbrace{\langle (\bar{\mathscr{D}}\delta_x\zeta^n)_i, (\delta_x\zeta^n)_i \rangle}_{\text{E-1}} \leq \hat{M}\Bigg(\|\zeta^n\|^2 + \underbrace{\langle \theta_i^n, \zeta_i^n \rangle}_{\text{E-2}} + h^2 + \Delta t^2 + \frac{h^4}{\Delta t^2} + \|\zeta^{n-1}\|^2 + \|\theta^{n-1}\|^2 \Bigg) + \underbrace{\langle \big((\bar{\mathscr{D}} - \mathscr{D})\delta_x s^n\big)_i, (\delta_x\zeta^n)_i \rangle}_{\text{E-3}} + \underbrace{\langle \phi_i \frac{\bar{\zeta}_i^{n-1} - \zeta_i^{n-1}}{\Delta t}, \zeta_i^n \rangle}_{\text{E4}} \tag{3.62}$$

We now estimate the remaining inner product terms E-1, E-2, E-3 and E-4 in Eq. (3.62).

E-1 : $\langle (\bar{\mathscr{D}}\delta_x\zeta^n)_i, (\delta_x\zeta^n)_i \rangle \geq D_* |\zeta^n|_{1,2}^2$,

E-2 : $\langle \theta_i^n, \zeta_i^n \rangle \leq M(\|\theta^n\|^2 + \|\zeta^n\|^2)$ (using Cauchy-Schwarz) ,

E-3 : $\langle ((\bar{\mathscr{D}} - \mathscr{D})\delta_x s^n)_i, (\delta_x\zeta^n)_i \rangle = \sum_i h|(\bar{\mathscr{D}} - \mathscr{D})\delta_x s^n|_i |\delta_x\zeta^n|_i$

$$\leq \left\| \frac{\partial s_i^n}{\partial x} \right\|_\infty \sum_i h \left| \mathscr{D}(\bar{w}_i^{n-1}, m_i^{n-1}) - \mathscr{D}(s_i^n, c_i^n) \right| \left| \frac{\partial \zeta_i^n}{\partial x} \right|.$$

Using Taylor series we write

$$\left| \mathscr{D}(\bar{w}_i^{n-1}, m_i^{n-1}) - \mathscr{D}(s_i^n, c_i^n) \right| \leq |s_i^n - \bar{w}_i^{n-1}| \left\| \frac{\partial \mathscr{D}}{\partial s} \right\|_\infty + |c_i^n - m_i^{n-1}| \left\| \frac{\partial \mathscr{D}}{\partial c} \right\|_\infty$$

$$\leq M(\Delta t + h\Delta t + h^2 + \left|\bar{\zeta}_i^{n-1}\right| + |\theta_i^{n-1}|),$$

where we use the estimate $|c_i^n - m_i^{n-1}| \le M(|\theta_i^{n-1}| + \Delta t)$. Also,

$$
\begin{aligned}
|s_i^n - \bar{w}_i^{n-1}| \le |s_i^n - s_i^{n-1}| + |s_i^{n-1} - \bar{w}_i^{n-1}| &\le |s_i^n - s_i^{n-1}| + \left|\mathscr{I} s^{n-1}(\tilde{x}_i) - s_i^{n-1} - \bar{\zeta}_i^{n-1}\right| \\
&\le M\left(\Delta t + |\tilde{x}_i - x_i| \|s^{n-1}\|_{1,\infty} + \left|(1-\mathscr{I})s^{n-1}(\tilde{x}_i)\right| + \left|\bar{\zeta}_i^{n-1}\right|\right) \\
&\le M\left(\Delta t + \left\|\frac{\partial f}{\partial s}\right\|_\infty \|z^{n-1}\|_\infty \frac{\Delta t}{\phi_*} + Ch^2 + \left|\bar{\zeta}_i^{n-1}\right|\right) \\
&\le M\left(\Delta t + h\Delta t + h^2 + \left|\bar{\zeta}_i^{n-1}\right|\right)
\end{aligned}
$$

Above, we have used Eq. (3.59) and that $\|z^{n-1}\|_\infty$ is bounded which has been proved after Eq. (3.72) below. Hence we have an estimate for E-3 as

$$
\begin{aligned}
\left\langle \left((\bar{\mathscr{D}} - \mathscr{D})\delta_x s^n\right)_i, (\delta_x \zeta^n)_i \right\rangle &\le M_1 \|s^n\|_{1,\infty} \sum_i h|\bar{\zeta}_i^{n-1}| \left|\frac{\partial \zeta_i^n}{\partial x}\right| + M_2 \|s^n\|_{1,\infty} \sum_i h|\theta_i^{n-1}| \left|\frac{\partial \zeta_i^n}{\partial x}\right| \\
&\quad + M_3 \|s^n\|_{1,\infty} \sum_i h(\Delta t + h\Delta t + h^2)\left|\frac{\partial \zeta_i^n}{\partial x}\right| \\
&\le M(\|\bar{\zeta}^{n-1}\|^2 + \|\theta^{n-1}\|^2 + |\zeta^n|_{1,2}^2 + \Delta t^2 + h^2\Delta t^2 + h^4).
\end{aligned}
$$

E-4. Estimate of the term E-4 in Eq. (3.62): Using the fundamental theorem of calculus,

$$
\bar{\zeta}_i^{n-1} - \zeta_i^{n-1} = \int_{x_i}^{\tilde{x}_i} \frac{\partial \zeta^{n-1}}{\partial x} \frac{\tilde{x}_i - x_i}{|\tilde{x}_i - x_i|}\, d\sigma
$$

$$
\text{Hence} \quad |\bar{\zeta}_i^{n-1} - \zeta_i^{n-1}| \le \int_{x_i}^{\tilde{x}_i} \left|\frac{\partial \zeta^{n-1}}{\partial x}\right| d\sigma \le \left(\int_{x_i}^{\tilde{x}_i} d\sigma\right)^{1/2} \left(\int_{x_i}^{\tilde{x}_i} \left|\frac{\partial \zeta^{n-1}}{\partial x}\right|^2 d\sigma\right)^{1/2}.
$$

Therefore,

$$\begin{aligned}
\langle \phi_i \frac{\bar{\zeta}_i^{n-1} - \zeta_i^{n-1}}{\Delta t}, \zeta_i^n \rangle &\leq \frac{\phi^*}{\Delta t} \left(\sum_i h |\zeta_i^n|^2 \right)^{1/2} \left(\sum_i h |\bar{\zeta}_i^{n-1} - \zeta_i^{n-1}|^2 \right)^{1/2} \\
&\leq M |\zeta^{n-1}|_{1,2} \, |\zeta^n|_\infty \|z^{n-1}\|_\infty \\
&\leq M |\zeta^{n-1}|_{1,2} \, |\zeta^n|_{1,2} \, (1+h) \, (\log 1/h)^{1/2} \quad [\text{ Using a result from [86]}] \\
&\leq M \, (\log 1/h)^{1/2} \, (1+h) \left(|\zeta^{n-1}|_{1,2}^2 + |\zeta^n|_{1,2}^2 \right).
\end{aligned}$$

Above we have again used that $\|z^{n-1}\|_\infty$ is bounded. Using all of the above estimates for E-1, E-2, E-3, E-4 in Eq. (3.62) we get,

$$\begin{aligned}
& M(\|\zeta^n\|^2 - \|\zeta^{n-1}\|^2) + D_* \Delta t |\zeta^n|_{1,2}^2 \\
& \leq M \Delta t (h^2 + \Delta t^2 + \frac{h^4}{\Delta t^2} + h^2 \Delta t^2 + h^4) \\
& \quad + M \Delta t \left(\|\zeta^n\|^2 + \|\theta^n\|^2 + \|\zeta^{n-1}\|^2 + \|\theta^{n-1}\|^2 \right) \\
& \quad + M \Delta t (1 + (1+h) \, (\log 1/h)^{1/2}) \left(|\zeta^{n-1}|_{1,2}^2 + |\zeta^n|_{1,2}^2 \right).
\end{aligned} \tag{3.63}$$

Summing over $1 \leq n \leq L$ (with $L \Delta t = T$) we get,

$$\begin{aligned}
& M(\|\zeta^L\|^2 - \|\zeta^0\|^2) + D_* \Delta t \sum_{n=1}^{L} |\zeta^n|_{1,2}^2 \\
& \leq MT(h^2 + \Delta t^2 + \frac{h^4}{\Delta t^2} + h^2 \Delta t^2 + h^4) + M \Delta t \sum_{n=1}^{L} \left(\|\zeta^n\|^2 + \|\theta^n\|^2 + \|\zeta^{n-1}\|^2 + \|\theta^{n-1}\|^2 \right) \\
& + M \Delta t \left(1 + (1+h) \, (\log 1/h)^{1/2} \right) \sum_{n=1}^{L} |\zeta^n|_{1,2}^2.
\end{aligned}$$

Using discrete Gronwall's inequality and noting that $\zeta_i^0 = 0$ and $\theta_i^0 = 0$ this can be

rewritten as

$$M\|\zeta^L\|^2 + (D_*\Delta t - \rho_1)\sum_{n=1}^{L}|\zeta^n|_{1,2}^2 \leq M\Delta t\sum_{n=1}^{L}\left(\|\theta^n\|^2\right) + M\ \max(h^2+\Delta t^2, h^4/\Delta t^2) \tag{3.64}$$

where $\rho_1 = M\Delta t(1+(1+h)\left(\log 1/h\right)^{1/2}) \to 0$ faster than $D_*\Delta t$ as $(h,\Delta t)\to 0$. This concludes the analysis of the water transport equation (Eq. (3.37a)).

Next we consider the polymer transport equation (Eq. (3.37b)). Replacing the advective terms with a derivative along the characteristic direction, Eq. (3.37b) becomes

$$\psi_c\frac{\partial c}{\partial \tau} + Gc = H, \tag{3.65}$$

whose finite difference approximation is given by

$$\phi_i\frac{m_i^n - \bar{m}_i^{n-1}}{\Delta t} + G_i^n m_i^n = H_i^n. \tag{3.66}$$

Recall that $\theta_i^n = c_i^n - m_i^n$. Using an analogue of Lemma 3.3.1 for the characteristic derivative of the polymer transport equation in Eq. (3.65) and subtracting Eq. (3.66) from the result we obtain

$$\begin{aligned}\phi_i\frac{\theta_i^n - (\bar{c}_i^{n-1} - \bar{m}_i^{n-1})}{\Delta t} + G_i^n\theta_i^n &= H(s_i^n) - H(w_i^n) + O\left(\left\|\frac{\partial^2 c}{\partial\tau^2}\right\|_\infty \Delta\tau\right)\\ &\leq |H(s_i^n) - H(w_i^n)| + M\Delta t\end{aligned} \tag{3.67}$$

As before the source terms are estimated as

$$|H(s_i^n) - H(w_i^n)| \leq |s_i^n - w_i^n|\left\|\frac{\partial H}{\partial s}\right\|_\infty \leq M|\zeta_i^n| \tag{3.68}$$

In the following, with slight abuse of notation, we suppress the superscript "c" from $\tilde{x}_i^{c,n}$ and $\bar{x}_i^{c,n}$ to denote the points on the characteristic curves of the polymer transport equation. Continuing with the analysis, we rewrite the numerator of the first term on the left side of Eq. (3.67) as

$$\theta_i^n - (\bar{c}_i^{n-1} - \bar{m}_i^{n-1}) = (\theta_i^n - \bar{\theta}_i^{n-1}) - \underbrace{(c^{n-1}(\bar{x}_i) - c^{n-1}(\tilde{x}_i))}_{\text{F}} - \underbrace{(1-\mathscr{I})c^{n-1}(\tilde{x}_i)}_{\text{G}} \tag{3.69}$$

The term G is estimated by the Peano kernel theorem, as was done in Eq. (3.59).

F. Estimate of the term F: This estimate is carried out in a series of steps.

$$\begin{aligned}
&|c^{n-1}(\bar{x}_i) - c^{n-1}(\tilde{x}_i)| \leq \|c^{n-1}\|_{1,\infty} |\tilde{x}_i - \bar{x}_i| \\
&\leq M \frac{\Delta t}{\phi_*} \underbrace{\left| \frac{f}{s}(\bar{w}_i^n, m_i^{n-1}) z_i^{n-1} - \frac{f}{s}(s_i^n, c_i^n) v_i^n \right|}_{\text{F-1}} \\
&\qquad + M \frac{\Delta t}{\phi_*} \underbrace{\left| \frac{D}{s}(\bar{w}_i^n, m_i^{n-1}) \frac{\partial w_i^n}{\partial x} - \frac{D}{s}(s_i^n, c_i^n) \frac{\partial s_i^n}{\partial x} \right|}_{\text{F-2}}
\end{aligned} \tag{3.70}$$

F-1. Estimate of the term F-1:

$$\begin{aligned}
\left| \frac{f}{s}(\bar{w}_i^n, m_i^{n-1}) z_i^{n-1} - \frac{f}{s}(s_i^n, c_i^n) v_i^n \right| &\leq \left| \frac{f}{s} \bar{w}_i^n, m_i^{n-1}) \right| \underbrace{\left| z_i^{n-1} - v_i^n \right|}_{\text{F-1-1}} \\
&\quad + \underbrace{\left| \frac{f}{s}(\bar{w}_i^n, m_i^{n-1}) - \frac{f}{s}(s_i^n, c_i^n) \right|}_{\text{F-1-2}} |v_i^n|
\end{aligned} \tag{3.71}$$

Out of the two pieces F-1-1 and F-1-2 required to obtain an estimate of F-1, we have already estimated the term F-1-1 in Eq. (3.56) which we recall here: $\left| z_i^{n-1} - v_i^n \right| \leq M(h + \Delta t + |\zeta_i^{n-1}| + |\theta_i^{n-1}|)$. We next estimate the term F-1-2 in Eq. (3.56).

F-1-2. Estimate of the term F-1-2 in Eq. (3.71):

$$\begin{aligned}
&\left|\frac{f}{s}(\bar{w}_i^n, m_i^{n-1}) - \frac{f}{s}(s_i^n, c_i^n)\right| \\
&\quad \leq |\bar{w}_i^n - s_i^n| \left\| \frac{\partial}{\partial s}\left(\frac{f}{s}\right)\right\|_\infty + |\theta_i^{n-1}| \left\| \frac{\partial}{\partial c}\left(\frac{f}{s}\right)\right\|_\infty + \Delta t \left\|\frac{\partial c_i^n}{\partial t}\right\|_\infty \left\| \frac{\partial}{\partial c}\left(\frac{f}{s}\right)\right\|_\infty \\
&\quad \leq M\left(\underbrace{|\bar{w}_i^n - s_i^n|}_{\text{F-1-2-a}} + |\theta_i^{n-1}| + \Delta t\right)
\end{aligned}$$

F-1-2-a. Estimate of the term F-1-2-a:

$$\bar{w}_i^n - s_i^n = \mathscr{I} s^n(\tilde{x}_i) - s^n(x_i) - \bar{\zeta}_i^n = (\tilde{x}_i - x_i)\frac{\partial s^{n*}}{\partial x} - (1-\mathscr{I})s^n(\tilde{x}_i) - \bar{\zeta}_i^n$$

Therefore

$$\begin{aligned}
|\bar{w}_i^n - s_i^n| &\leq |\tilde{x}_i - x_i| \left\|s^n\right\|_{1,\infty} + Ch^2 + |\bar{\zeta}_i^n| \quad \text{(Using the Peano-kernel theorem)} \\
&\leq M\Delta t \left\{ \left\|\frac{f}{s}\right\|_\infty \left\|z^{n-1}\right\|_\infty + \left\|\frac{D}{s}\right\|_\infty \left(\left|\frac{\partial s_i^n}{\partial x}\right|_\infty + \left|\frac{\partial \zeta_i^n}{\partial x}\right| \right) \right\} + Ch^2 + |\bar{\zeta}_i^n| \\
&\leq M\Delta t \left\{ h + C + \left|\frac{\partial \zeta_i^n}{\partial x}\right| \right\} + Mh^2 + |\bar{\zeta}_i^n| \qquad (3.72)
\end{aligned}$$

The last step of the above estimate in Eq. (3.72) requires a bound on $\left\|z^{n-1}\right\|_\infty$ which was also used while estimating the term E-4. Before further analysis, we prove this statement here. Note that, even though we prove the result for $\left\|z^n\right\|_\infty$, it is true for any other time t^n with $n \in (0, T)$.

$$\begin{aligned}
z_i^n &= -K\lambda(w_i^n, m_i^n)\frac{\partial r_i^n}{\partial x} = K\lambda(w_i^n, m_i^n)\left[\frac{\partial \pi_i^n}{\partial x} - \frac{\partial p_i^n}{\partial x}\right]. \\
\left\|z^n\right\|_\infty &\leq \|K\|_\infty \|\lambda\|_\infty \left(1 + \left\|\frac{\partial \pi_i^n}{\partial x}\right\|_\infty\right) \leq M(1+\beta h); \quad (\beta \text{ is a constant})
\end{aligned}$$

Using Eq. (3.72) we obtain an estimate for F-1-2 as

$$\left|\frac{f}{s}(\bar{w}_i^n, m_i^{n-1}) - \frac{f}{s}(s_i^n, c_i^n)\right| \leq M\left(h^2 + \Delta t + h\Delta t + \left|\theta_i^{n-1}\right| + \left|\bar{\zeta_i^n}\right| + \Delta t\left|\frac{\partial \zeta^n}{\partial x}\right|\right) \tag{3.73}$$

Using these estimates of F-1-1 and F-1-2 in Eq. (3.71) we obtain an estimate of F-1 as

$$\begin{aligned}\left|\frac{f}{s}(\bar{w}_i^n, m_i^{n-1})z_i^{n-1} - \frac{f}{s}(s_i^n, c_i^n)v_i^n\right| &\leq M\left(h + \Delta t + h^2 + h\Delta t\right) \\ &\quad + M\left(|\zeta_i^{n-1}| + |\theta_i^{n-1}| + |\bar{\zeta_i^n}| + \Delta t\left|\frac{\partial \zeta^n}{\partial x}\right|\right)\end{aligned} \tag{3.74}$$

F-2. Estimate of the term F-2 of Eq. (3.70):

$$\begin{aligned}&\left|\frac{D}{s}(\bar{w}_i^n, m_i^{n-1})\frac{\partial w_i^n}{\partial x} - \frac{D}{s}(s_i^n, c_i^n)\frac{\partial s_i^n}{\partial x}\right| \\ &\quad\leq \left|\frac{D}{s}(\bar{w}_i^n, m_i^{n-1}) - \frac{D}{s}(s_i^n, c_i^n)\right|\left|\frac{\partial s_i^n}{\partial x}\right| + \left|\frac{D}{s}(\bar{w}_i^n, m_i^{n-1})\right|\left|\frac{\partial (w_i^n - s_i^n)}{\partial x}\right| \\ &\quad\leq \left(\underbrace{|\bar{w}_i^n - s_i^n|}_{\text{F-1-2-a}}\left\|\frac{\partial}{\partial s}\left(\frac{D}{s}\right)\right\|_\infty + |m_i^{n-1} - c_i^n|\left\|\frac{\partial}{\partial c}\left(\frac{D}{s}\right)\right\|_\infty\right)\left|\frac{\partial s_i^n}{\partial x}\right| \\ &\qquad + \left\|\frac{D}{s}(\bar{w}_i^n, m_i^{n-1})\right\|_\infty\left|\frac{\partial \zeta_i^n}{\partial x}\right|\end{aligned} \tag{3.75}$$

Using the estimate for F-1-2-a given in Eq. (3.72) in Eq. (3.75), we obtain

$$\begin{aligned}\left|\frac{D}{s}(\bar{w}_i^n, m_i^{n-1})\frac{\partial w_i^n}{\partial x} - \frac{D}{s}(s_i^n, c_i^n)\frac{\partial s_i^n}{\partial x}\right| &\leq M\left(|\bar{w}_i^n - s_i^n| + |\theta_i^{n-1}| + \Delta t + \left|\frac{\partial \zeta_i^n}{\partial x}\right|\right) \\ &\leq M\left(\Delta t\left(C + h + \left|\frac{\partial \zeta_i^n}{\partial x}\right|\right) + h^2 + |\bar{\zeta_i^n}| + |\theta_i^{n-1}| + \Delta t + \left|\frac{\partial \zeta_i^n}{\partial x}\right|\right) \\ &\leq M\left(\Delta t + h^2 + h\Delta t + |\bar{\zeta_i^n}| + |\theta_i^{n-1}| + (1 + \Delta t)\left|\frac{\partial \zeta_i^n}{\partial x}\right|\right).\end{aligned} \tag{3.76}$$

Using Eq. (3.74) and Eq. (3.76) in Eq. (3.70) we obtain the following estimate for the term F in Eq. (3.69).

$$
\begin{aligned}
&|c^{n-1}(\bar{x_i}) - c^{n-1}(\tilde{x_i})| \\
&\quad \leq M\Delta t \left(h + \Delta t + h^2 + h\Delta t + |\zeta_i^{n-1}| + |\theta_i^{n-1}| + |\bar{\zeta_i^n}| + \Delta t \left| \frac{\partial \zeta^n}{\partial x} \right| \right) \\
&\qquad + M\Delta t \left(\Delta t + h^2 + h\Delta t + |\bar{\zeta_i^n}| + |\theta_i^{n-1}| + (1+\Delta t) \left| \frac{\partial \zeta_i^n}{\partial x} \right| \right) \\
&\quad \leq M\Delta t \left(h + \Delta t + h^2 + h\Delta t + |\zeta_i^{n-1}| + |\theta_i^{n-1}| + |\bar{\zeta_i^n}| + (1+\Delta t) \left| \frac{\partial \zeta_i^n}{\partial x} \right| \right).
\end{aligned}
\tag{3.77}
$$

We test Eq. (3.67) against θ_i^n and using Eq. (3.68) and Eq. (3.77), we get

$$
\begin{aligned}
&\langle \phi_* \frac{\theta_i^n - \bar{\theta}_i^{n-1}}{\Delta t}, \theta_i^n \rangle + \langle \hat{M}\theta_i^n, \theta_i^n \rangle \\
&\quad \leq \langle M \left(h + h^2 + \Delta t + h\Delta t + |\zeta_i^{n-1}| + |\theta_i^{n-1}| + |\bar{\zeta_i^n}| + (1+\Delta t) \left| \frac{\partial \zeta_i^n}{\partial x} \right| \right), \theta_i^n \rangle \\
&\qquad + \langle M \left(\frac{h^2}{\Delta t} + \Delta t + |\zeta_i^n| \right), \theta_i^n \rangle.
\end{aligned}
$$

After some simplification, we get

$$
\begin{aligned}
&\phi_* \left(\|\theta^n\|^2 - \|\theta^{n-1}\|^2 \right) \\
&\quad \leq \phi^* \|\theta^n\|^2 + (\phi^* - \phi_*) \left\|\theta^{n-1}\right\|^2 + \bar{M}\Delta t \left(h^4 + \Delta t^2 + h^2 + h^2\Delta t^2 + \frac{h^4}{\Delta t^2} \right) \\
&\qquad + M\Delta t \left(\|\theta^{n-1}\|^2 + \|\zeta^{n-1}\|^2 + \|\theta^n\|^2 + \|\zeta^n\|^2 + (1+\Delta t) \left(|\zeta^n|_{1,2}^2 + \|\theta^n\|^2 \right) \right).
\end{aligned}
\tag{3.78}
$$

Adding Eq. (3.63) and Eq. (3.78), summing over $1 \leq n \leq L$ and after some further

simplification, we get

$$
\begin{aligned}
&M(\left\|\zeta^L\right\|^2 + \left\|\theta^L\right\|^2) + \bar{M}\Delta t \sum_{n=1}^{L} |\zeta^n|_{1,2}^2 \\
&\quad \leq M(1 + \Delta t + \Delta t^2) \sum_{n=0}^{L} \|\theta^n\|^2 + M\Delta t \sum_{n=0}^{L} \|\zeta^n\|^2 \\
&\quad + MT\left(h^2 + \Delta t^2 + h^2\Delta t^2 + h^4 + \frac{h^4}{\Delta t^2}\right) \\
&\quad + M\Delta t\left((1 + \Delta t) + (1 + h)(\log 1/h)^{1/2}\right) \sum_{n=0}^{L} |\zeta^n|_{1,2}^2
\end{aligned} \tag{3.79}
$$

where $T = L\Delta t$. Let $\rho = \left((1 + \Delta t) + (1 + h)(\log 1/h)^{1/2}\right)$ such that $\rho \to 0$. Then using the discrete Gronwall's inequality in Eq. (3.79), we get

$$
\left\|\zeta^L\right\|^2 + \left\|\theta^L\right\|^2 + \Delta t \sum_{n=0}^{L} |\zeta^n|_{1,2}^2 \leq M(h^2 + \Delta t^2), \tag{3.80}
$$

$$
\begin{aligned}
\text{where } M = M\Bigg(&\|s\|_{L^\infty(W^{3,\infty})},\ \|s\|_{W^{1,\infty}(L^\infty)},\ \left\|\frac{\partial^2 s}{\partial \tau^2}\right\|_{L^\infty(L^\infty)},\ \|c\|_{L^\infty(W^{3,\infty})}, \\
&\|c\|_{W^{1,\infty}(L^\infty)},\ \left\|\frac{\partial^2 c}{\partial \tau^2}\right\|_{L^\infty(L^\infty)},\ \|p\|_{L^\infty(W^{1,\infty})},\ \|p\|_{W^{1,\infty}(W^{1,\infty})}\Bigg).
\end{aligned}
$$

It is also assumed that the auxiliary functions $f(s,c), \lambda(s,c), D(s,c)$ have sufficient regularity in the discrete Sobolev norms. We anticipate an L^2 error of the order $O(h)$ and consequently, we assume that $\Delta t = O(h)$ as $h \to 0$ which implies $\max(h^2 + \Delta t^2, h^4/\Delta t^2) = h^2 + \Delta t^2$. In particular, it follows that

$$
\left\|\zeta^L\right\|_{L^2} \leq Mh, \quad \left\|\theta^L\right\|_{L^2} \leq Mh. \tag{3.81}
$$

Note that $\Delta t = O(h)$ hypothesis is very reasonable since in the case of a one-dimensional parabolic equation the basic method can only be expected to have an $O(h + \Delta t)$ estimate.

Also, with a less stringent restriction like $\Delta t = O(h^{\gamma})$ for some $\gamma < 2$, we will have an L^2 error estimate of the order $O(h^{1-\gamma/2})$. The final error estimate is summarized in the following theorem.

Theorem 3.3.3 *Let s and c be the solutions of Eq.* (3.37a) *and Eq.* (3.37b) *respectively. Let w and m be the solutions of Eq.* (3.42b) *and Eq.* (3.39) *respectively where $\bar{w}_i^{n-1}$ is given by Eq.* (3.40) *and $\bar{m}_i^{n-1}$ is given by Eq.* (3.41)*. Then, the errors $\zeta = s - w$ and $\theta = c - m$ satisfy the inequalities given in Eq.* (3.81) *and the convergence result given in Eq.* (3.80)*.*

3.3.1 Extension to two dimensions in space

Here we discuss how to extend the analysis of Eq. (3.39) and Eq. (3.42b) to two spatial dimensions. The error estimates for the discretization of the characteristic derivatives and the capillary dissipation terms, obtained in Lemma 3.3.1 and Lemma 3.3.2 respectively, can be easily extended to two spatial dimensions without changing the order of the estimates. The various inequalities and tools used at various stages of the analysis like the Cauchy-Schwarz inequality, discrete Gronwall's inequality and the Taylor series have multidimensional analogues. The Peano kernel theorem can also be used in a similar manner for estimating the error introduced due to the bilinear interpolation required in the two-dimensional analysis. The $\left\| \frac{\partial \pi}{\partial x} \right\|_{\infty}$ estimate obtained from the finite element solution of the elliptic pressure equation is also available in two or higher spatial dimensions [82]. The L^{∞} estimate of a mesh function [86], that has been used to estimate the term E4, is also applicable for a two-dimensional domain. In the analysis of the one dimensional system, the spatial grid has been taken to be uniform with a fixed spatial grid size h. In the two dimensional system, the grid can be taken to be uniform in each spatial dimension with constant $h_x = \Delta x$ and $h_y = \Delta y$. The quasilinear treatment of the nonlinearity in the functions f, D, λ will allow us to obtain analogous estimates of the two-dimensional inner

products involving these terms without affecting the convergence results. Hence, a similar analytical calculation can be made to obtain an $O(h_x + h_y + \Delta t)$ error estimate for the two dimensional problem.

3.3.2 Extension to two component systems

Here we discuss the possibility of extending this analysis to the case of two-component two-phase flows like SP flooding. We recall the system of equations below.

$$-\boldsymbol{\nabla}\cdot(\mathbf{K}(\mathbf{x})\lambda(s,c,\Gamma)\boldsymbol{\nabla}p) = q_a + q_o, \tag{3.82a}$$

$$\phi\frac{\partial s}{\partial t} + \frac{\partial f_a}{\partial s}\mathbf{v}\cdot\boldsymbol{\nabla}s + \boldsymbol{\nabla}\cdot\left(\boldsymbol{D}\frac{\partial p_c}{\partial s}\boldsymbol{\nabla}s\right) = g_s - \frac{\partial f_a}{\partial c}\mathbf{v}\cdot\boldsymbol{\nabla}c - \frac{\partial f_a}{\partial \Gamma}\mathbf{v}\cdot\boldsymbol{\nabla}\Gamma - \boldsymbol{\nabla}\cdot\left(\boldsymbol{D}\frac{\partial p_c}{\partial \Gamma}\boldsymbol{\nabla}\Gamma\right), \tag{3.82b}$$

$$\phi\frac{\partial c}{\partial t} + \left(\frac{f_a}{s}\mathbf{v} + \frac{\boldsymbol{D}}{s}\frac{\partial p_c}{\partial s}\boldsymbol{\nabla}s + \frac{\boldsymbol{D}}{s}\frac{\partial p_c}{\partial \Gamma}\boldsymbol{\nabla}\Gamma\right)\cdot\boldsymbol{\nabla}c = g_c, \tag{3.82c}$$

$$\phi\frac{\partial \Gamma}{\partial t} + \left(\frac{f_a}{s}\mathbf{v} + \frac{\boldsymbol{D}}{s}\frac{\partial p_c}{\partial s}\boldsymbol{\nabla}s + \frac{\boldsymbol{D}}{s}\frac{\partial p_c}{\partial \Gamma}\boldsymbol{\nabla}\Gamma\right)\cdot\boldsymbol{\nabla}\Gamma = g_\Gamma, \tag{3.82d}$$

where $D(s,c,\Gamma) = \mathbf{K}(\mathbf{x})\lambda_o(s,\Gamma)f_a(s,c,\Gamma)$, Γ is the surfactant concentration and the source terms q_a, q_o, g_s, g_c, g_Γ are defined similar to the one-component flow model. As seen from the above model, the transport equations for polymer and surfactant have a similar structure. Hence the surfactant transport equation can be analyzed in a similar fashion to obtain error estimates for this two-component two-phase flow system. However, such an exercise also poses certain challenges. The functions p_c and $D, f, \lambda, \lambda_a, \lambda_o$ are not always dependent on all three components s, c, Γ. For instance, the capillary pressure $p_c = p_c(s,\Gamma)$ is only affected by changes in water saturation s and surfactant concentration Γ, whereas the fractional flow functions $f_a = f_a(s,c,\Gamma)$ and $f_o = f_o(s,c,\Gamma)$, depend on all three. Similarly, $\lambda_a = \lambda_a(s,c,\Gamma)$ but $\lambda_o = \lambda_o(s,\Gamma)$. This means that the estimates are not always symmetric with respect to the two transport variables c and Γ.

Hence, an analogous error estimate for the two-component system is difficult to obtain as a direct extension of the one-component system and it needs further non-trivial analysis. However, due to the similarity in the structure of the transport equations for c and Γ and because the numerical method for the two-component system is a direct extension of the one-component system, we anticipate an equivalent L^2 estimate of the order $O(h + \Delta t)$ even for the error in surfactant concentration.

4. NUMERICAL RESULTS AND DISCUSSION*

In this chapter we present various numerical simulation results that are aimed towards not only validating the method but also studying the effects of the chemical species in improving overall recovery. In section 4.1 we present the numerical errors and orders of accuracy of the method obtained with an exact solution as well as with a realistic polymer flood simulation. In section 4.2 we investigate whether the method suffers from significant grid orientation effects. In section 4.3, waterflooding simulation results are presented to qualitatively validate the method against some known results in the literature and also with physically expected flow behavior. For all these waterflooding simulations the viscosity ratio, $M_\mu = \mu_o/\mu_w$ is kept fixed at $M_\mu = 10$. In section 4.4 and section 4.5, we present simulation studies of polymer flood and surfactant-polymer flood respectively. These simulations are designed to explore and identify the favorable aspects of various complex chemical enhanced flooding strategies and have been carried out by varying either the viscosity ratio, M_μ or the endpoint mobility ratio, $M_\lambda = \lambda_a(1-s^\sigma_{ro}, c_0, \Gamma_0)/\lambda_o(s^{\sigma 0}_0, \Gamma_0)$ of the flooding schemes. In the endpoint mobility ratio calculations, the numerator is evaluated at the saturation level ($s = 1 - s^\sigma_{ro}$) far behind the front of the displacing phase while the denominator is evaluated at the connate water saturation $s = s^{\sigma 0}_0$ which is the saturation level in the region not yet reached by the displacing phase. Besides M_λ, the shock front mobility ratio M_s is also commonly used to study two-phase displacement problems and

*Part of this chapter is reprinted from Journal of Computational Physics, 335, Prabir Daripa and Sourav Dutta, "Modeling and simulation of surfactant-polymer flooding using a new hybrid method", 249-282, doi: 10.1016/j.jcp.2017.01.038, Copyright (2017) with permission from Elsevier.

is defined as

$$M_s = \frac{\dfrac{k_{ro}(s^*, \Gamma_0)}{\mu_o} + \dfrac{k_{ra}(s^*, \Gamma_0)}{\mu_a(c_0)}}{\dfrac{k_{ro}(s_0^{\sigma 0}, \Gamma = 0)}{\mu_o} + \dfrac{k_{ra}(s_0^{\sigma 0}, \Gamma = 0)}{\mu_a(c = 0)}}, \tag{4.1}$$

where the relative permeabilities in the numerator are evaluated at the shock front water saturation, s^*. In an ideal situation, the purely two-phase flow of water displacing oil, also termed as Buckley-Leverett flow, is a piston-like displacement process with a sharp interface between the fluids. Ahead of this sharp interface, oil flows in the presence of connate water ($s = s_0^{\sigma 0}$) while behind the interface water alone flows in the presence of residual oil with the maximum possible water saturation of $s = 1 - s_{ro}^{\sigma}$. In such an ideal situation the endpoint mobility ratio M_λ is equal to the shock front mobility ratio M_s and the displacement process is stable and favorable if $M_\lambda < 1$. Unfortunately, the non-ideal displacement is more common in nature and it occurs when $M_\lambda > 1$. In this case, the discontinuity in the water saturation at the waterfront or shock front is usually followed by a gradual transition between the shock front saturation s^* and the maximum water saturation $1 - s_{ro}^{\sigma}$. Since the shock front mobility ratio M_s is calculated using the shock front saturation s^* it usually captures the local instability at the water front better than the endpoint mobility ratio M_λ. Hagoort [87] has shown, using a theoretical argument backed by experiment, that Buckley-Leverett displacement can be regarded as stable for the condition $M_s < 1$ which is usually less restrictive than the condition $M_\lambda < 1$. Therefore, M_s is also a significant parameter for characterizing the stability of such Buckley-Leverett type two-phase displacements. In all of the two-phase flow models studied in this dissertation, we have assumed a non-zero capillary pressure which effectively diffuses the shock front that normally appears in a purely Buckley-Leverett flow. Hence, we have calculated approximate shock front mobility ratios by taking s^* to be the saturation value at which the saturation

gradient is the highest. In the rest of this dissertation mobility ratio will be used to refer to endpoint mobility ratios unless explicitly specified as shock front mobility ratios.

We have used the viscosity ratio as well as both the mobility ratios to study the efficiency of different chemical floods in this study. This is because, while the polymer in the aqueous phase exclusively affects the viscosity of the displacing phase, the surfactant in SP flood also affects the relative permeabilities. Hence in the presence of surfactant, it makes sense to compare the effective change in the mobilities of the phases, while polymer floods can be studied by simply comparing the change in viscosities.

The simulations in sections 4.3–4.5 have been performed on a variety of homogeneous and heterogeneous spatial permeability field data that have been either generated numerically or are based on the dataset provided by the SPE10 benchmark problem [106]. All other input parameters are listed in Table 4.6. We use two different sets of values for injection rates Q and time step sizes Δt while running simulations in a quarter five-spot geometry and in a rectilinear geometry. As reported in Table 4.6, $Q = 200$ and $\Delta t = 1/50$ for a quarter five-spot geometry and $Q = 1/50$ and $\Delta t = 1/100$ for a rectilinear geometry.

The simulations have been carried out in MATLAB 2015b on a desktop computer with an Intel(R) Core(TM)2 Quad (Q9650) CPU with a clock speed of 3.00GHz, 4 GB of RAM, a GeForce GT 430/PCIe/SSE2 graphics card and running Linux Mint 13 Maya. A typical quarter five-spot flooding simulation on a 30×30 heterogeneous permeability field (SPE10) has a runtime of about 48 minutes until water breakthrough.

4.1 Error Analysis

4.1.1 Errors with an exact solution

We consider the waterflooding problem in $\Omega = [0,1]^2$ and we impose the following analytical solutions

$$p(x,y,t) = \left(C + \frac{x^3+y^3}{3} - \frac{x^2+y^2}{2}\right) e^{\pi t/2}, \tag{4.2a}$$

$$s(x,y,t) = 0.3 + 0.7\sin^2\left(\frac{\pi t}{2}\right)\left(\frac{\sin^2(2\pi x) + \cos^2(2\pi y)}{2}\right), \tag{4.2b}$$

with $\mathbf{K}(\mathbf{x}) = I$, $\phi(\mathbf{x}) = 1$, $\mu_w = \mu_o = 1$ and C is an arbitrary constant. We take $p_c(s) = \frac{1}{s-0.2}$, $k_{rw} = s_e^2$, and $k_{ro} = s_e(1-s_e)$ where s_e is the normalized saturation defined by $s_e = \frac{s-0.2}{1-0.4}$. Using the solutions for pressure and saturation given by eq. (4.2), the source terms and the initial data are calculated for the system which in turn are used to compute the numerical solution. The numerical errors are defined as follows

$$e_{s,max} = \max_{ij} |s(\mathbf{x}_{ij}) - w_{ij}| \approx \|s - w\|_{L^\infty}, \tag{4.3a}$$

$$e_{s,2} = \sqrt{\sum_{ij} |s(\mathbf{x}_{ij}) - w_{ij}|^2 \Delta x \Delta y} \approx \|s - w\|_{L^2}. \tag{4.3b}$$

Here, w_{ij} is the numerical solution w evaluated at the grid point $(x_i, y_j) = \mathbf{x}_{ij}$ whereas $s(\mathbf{x}_{ij})$ is the exact solution for saturation. The errors for the pressure and the velocity are computed in a similar fashion. The order of accuracy is computed using the formula $\log_2\left(e_\alpha(h)/e_\alpha(h/2)\right)$, $(\alpha = 2, \infty)$.

The exact solution, given above, has been carefully chosen to ensure that the coefficient matrices of the resulting linear algebraic systems are well conditioned. The simulations have been carried out with different values of the constant C but the results presented below are for $C = 0$. The errors between the exact and the numerical solutions for the

saturation, pressure and velocity in the L^2 norm and the L^∞ norm and the respective orders of accuracy are presented in Table 4.1. These have been computed at the final time $T = 0.5$ with a time-step of 0.005. We observe the following approximate order of accuracy in space.

$$\|p - r\|_{L^2} = O(h^2) \quad \& \quad \|\mathbf{v} - \boldsymbol{z}\|_{L^2} = O(h^2).$$

Table 4.1 shows that for a given fixed time-step, the errors decrease with refinement of the spatial mesh. However, for larger time steps (larger than 0.05) we find (data not shown here) that the time discretization errors dominate the spatial discretization errors. This leads to an increase in the L^2 and L^∞ error norms and a reduction in the order of accuracy. For example, the poor order of accuracy in the L^2 norm of the error in velocity seen in the last row of Table 4.1 has been found to improve significantly when a smaller time step is used for the entire simulation. The order of accuracy in the L^∞ norm of the error in saturation, presented in the upper part of the last column of Table 4.1, can also be seen to reduce significantly with reduction in spatial grid size. This is because the numerical solution attains a high accuracy, to the order of 10^{-5}, even at the largest spatial grid size used ($h = 1/8$). The error between the actual solution and the numerical solution does not improve much further and causes the loss in the order of accuracy.

The L^2 error in saturation has been shown to be of the order $O(h)$. This is consistent with the estimate obtained from our one-dimensional analysis presented in chapter 3 and, as discussed in section 3.3.1, is expected to be true in two-dimensional case. Moreover, the $O(h)$ error in the L^∞ norm of the gradient of pressure can also be observed Table 4.1.

The non-symmetric algebraic system obtained by assembling the stiffness matrix of the finite element weak formulation, given by eq. (3.16), and the symmetric but sparse algebraic system obtained by discretizing the transport equation, given by eq. (3.31a),

Table 4.1: Error and order for saturation, pressure and velocity using the analytic solution at the final time $T = 0.5$ with $\Delta t = 0.005$.

	h	$\|s - w\|_{L^2}$	Order	$\|s - w\|_{L^\infty}$	Order
Saturation	$1/8$	3.69e−5	–	4.97e−5	–
	$1/16$	1.36e−5	1.442	5.38e−5	0.891
	$1/32$	6.27e−6	1.116	4.33e−5	0.313
	$1/64$	3.07e−6	1.027	4.08e−5	0.087
	$1/128$	1.53e−6	1.006	4.02e−5	0.021
	h	$\|p - r\|_{L^2}$	Order	$\|p - r\|_{L^\infty}$	Order
Pressure	$1/8$	3.35e−3	–	1.20e−2	–
	$1/16$	1.04e−3	1.688	3.92e−3	1.611
	$1/32$	3.16e−4	1.720	1.23e−3	1.668
	$1/64$	9.36e−5	1.754	3.73e−4	1.725
	$1/128$	2.72e−5	1.784	1.10e−4	1.768
	h	$\|\mathbf{v} - \mathbf{z}\|_{L^2}$	Order	$\|\mathbf{v} - \mathbf{z}\|_{L^\infty}$	Order
Velocity	$1/8$	1.59e−3	–	3.27e−3	–
	$1/16$	4.13e−4	1.943	1.51e−3	1.118
	$1/32$	1.07e−4	1.950	7.17e−4	1.069
	$1/64$	2.82e−5	1.923	3.50e−4	1.036
	$1/128$	9.21e−6	1.614	1.75e−4	1.018

have been solved by a BICGstab iterative method with tolerance values in the range $10^{-6} - 10^{-9}$ and without any preconditioners. Apart from achieving high accuracy, there is one more important significance of choosing such ultra-low values of tolerance, specifically for solving the transport equations. It has been observed that the BICGstab solver converges to a solution with a relative residual of about 10^{-6} within the first two iterations for even moderately fine spatial resolution of $h = 1/32$. Hence, it becomes necessary to choose much lower levels of tolerance in order to compute the order of accuracy with respect

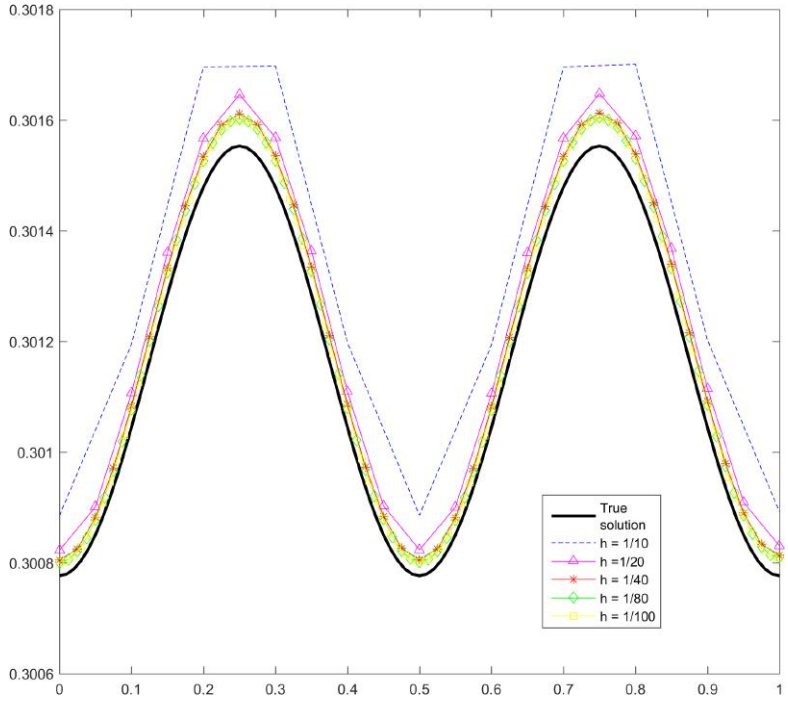

Figure 4.1: Comparison between the saturation profiles of the exact solution and the numerical solutions at various spatial resolutions. The profiles are plotted along the horizontal center line ($y = 0.5$) of the domain, $\Omega = [0, 1]^2$ at $t = 0.1$.

to spatial discretization for the water saturation. However, it is worth pointing out that there is a delicate balance involved in such a choice. If the tolerance is reduced even further from 10^{-9}, then the BICGstab iteration process may stagnate and fail to achieve the desired relative residuals. Although these observations were made in the context of the exact solution of waterflooding, these are also valid in the context of the transport equations for the polymer and the surfactant, given by eqs. (3.31b) and (3.31c).

In Figure 4.1 we plot the water saturation profiles along the center line, $y = 0.5$ at an intermediate time $t = 0.1$. The true solution is plotted with the solid black line while the numerical solution obtained on a sequence of successively refined grid sizes, $h = 1/10, 1/20, 1/40, 1/80, 1/100$ are plotted in different colors and line markers. This figure shows that the numerical solution monotonically improves with reduction in spatial grid

Table 4.2: Error and rates for saturation with time step refinement, computed at $T = 1$ using the analytical solution.

h	Δt	$\|s - w\|_{L^2}$	Rate	$\|s - w\|_{L^\infty}$	Rate
$\frac{1}{16}$	$1/20$	1.57e−4	–	1.00e−3	–
	$1/40$	3.58e−5	1.670	3.36e−4	1.588
	$1/80$	8.49e−6	1.625	1.10e−4	1.610
	$1/160$	2.15e−6	1.509	3.88e−5	1.505
	$1/320$	5.51e−7	1.464	1.41e−5	1.462
$\frac{1}{32}$	$1/20$	6.82e−5	–	4.20e−4	–
	$1/40$	1.99e−5	1.297	1.76e−4	1.253
	$1/80$	5.75e−6	1.319	7.14e−5	1.302
	$1/160$	1.69e−6	1.260	2.99e−5	1.253
	$1/320$	4.73e−7	1.299	1.22e−5	1.296
$\frac{1}{64}$	$1/20$	4.91e−5	–	3.12e−4	–
	$1/40$	1.62e−5	1.077	1.37e−4	1.184
	$1/80$	5.08e−6	1.168	6.22e−5	1.144
	$1/160$	1.56e−6	1.165	2.78e−5	1.162
	$1/320$	4.50e−7	1.247	1.17e−5	1.244

size and converges toward the exact solution.

Table 4.2 shows the numerical errors and the order of accuracy for the saturation equation with respect to time for three choices of fixed spatial grid sizes, namely $h = 1/16, 1/32$ and $1/64$. The errors are computed at the final time $T = 1$. The results confirm that at least a first-order convergence rate in time can be obtained using this method. This compares favorably with results obtained by others (see [88]) on similar types of problems. Additionally, we expect that with higher order time-stepping methods, the method will be able to preserve the accuracy and the expected second or third order convergence rates. It

is also important to note that with a fixed time step, the accuracy of the method increases with decreasing spatial grid size which can also serve as a quick validation of the results presented in Table 4.1. Moreover, Table 4.2 shows a higher than expected convergence rate with respect to time. This is because the reduction in the error norm associated with a time step size refinement increases as the spatial grid size increases.

From Table 4.1 and Table 4.2 we can also infer that the method suffers from very minimal numerical diffusion. The L^2 error in the water saturation values lies in the range of $10^{-5} - 10^{-7}$ when spatial grid sizes lie in the range of $10^{-2} - 10^{-3}$. This indicates that the amount of numerical diffusion is negligible and does not dominate over the capillary pressure induced physical diffusion.

4.1.2 Errors with two-dimensional polymer flood simulations

In this section, we present numerical results obtained from solving the two-phase single component system of equations (polymer flooding), given by eqs. (2.18a)–(2.18c), subject to realistic initial and boundary data. In section 4.3, the input data is given in table 4.3. The numerical errors are measured in the discrete norms.

$$e_{s,max} = \max_{ij} |s(\mathbf{x}_{ij}) - w_{ij}| \equiv \|s - w\|_{L^\infty}, \tag{4.4a}$$

$$e_{s,2} = \sqrt{\sum_{ij} |s(\mathbf{x}_{ij}) - w_{ij}|^2 \Delta x \Delta y} \equiv \|s - w\|_{L^2}. \tag{4.4b}$$

Here, w_{ij} is the numerical solution w evaluated at the grid point $(x_i, y_j) = \mathbf{x}_{ij}$ whereas $s(\mathbf{x}_{ij})$ is the finest grid numerical solution. The errors for the pressure and the velocity are computed in a similar fashion. The order of accuracy is computed using the formula $\log_2 \left(e_\alpha(h)/e_\alpha(h/2)\right)$ $(\alpha = 2, \infty)$.

We perform simulation of polymer flooding on a quarter five-spot homogeneous geometry $\Omega = [0, 1]^2$ with absolute permeability, $\mathbf{K} = 1$ and input parameters listed in

Table 4.3. The transport source terms in eqs. (2.18a) and (2.18b) for a quarter-five spot flow geometry are taken as

$$g_s = \begin{cases} (1-f_a)Q \\ 0 \end{cases} \quad g_c = \begin{cases} (c^i - c)Q/s \\ 0 \end{cases} \quad \text{at } \mathbf{x} = \begin{cases} \mathbf{x}^i \equiv (0,0) & \text{(source)} \\ \Omega \setminus \{\mathbf{x}^i\} & \text{(elsewhere)} \end{cases}.$$

The source terms for the pressure eq. (2.18c) are taken as

$$q_a = \begin{cases} Q \\ -(\lambda_a/\lambda)\, Q\,; \\ 0 \end{cases} \quad q_o = \begin{cases} 0 \\ -(\lambda_o/\lambda)\, Q \\ 0 \end{cases} \quad \text{at } \begin{cases} \mathbf{x}^i = (0,0) & \text{(Source)} \\ \mathbf{x}^p = (1,1) & \text{(Sink)} \\ \mathbf{x} \in \Omega \setminus \{(0,0) \cup (1,1)\} & \text{(Elsewhere)} \end{cases}.$$

We compute the L^∞ and L^2 error norms of the numerical solutions for the saturation on a

Table 4.3: Simulation input data

Model parameter	Symbol	Value
Spatial grid size	$h \times k$	variable
Porosity	ϕ	1
Initial resident water saturation	$s_0^{\sigma 0}$	0.21
Oil viscosity	μ_o	12.6
Pure water viscosity	μ_w	1.26
Residual aqueous phase saturation	s_{ra}	0.1
Residual oleic phase saturation	s_{ro}	0.2
Parameters of capillary pressure relation [eq. (2.21c)]	α_0, m	0.125, $2/3$
Concentration of polymer in injected fluid	c_0	0.1
Injection rate	Q	200
Time step size	Δt	$1/50$

sequence of uniformly refined meshes $h = 1/8, 1/16, 1/32, 1/64$ using eq. (4.3), but with $s(\mathbf{x}_{ij})$ representing the solution on the finest grid size $h = 1/128$. A similar procedure

is applied to estimate the error norms and the order of accuracy for the pressure and the velocity. The numerical errors and the order of accuracy are presented in Table 4.4. In Table 4.5 we present the numerical errors and convergence rates with respect to time step size refinement $\Delta t = 1/20, \ldots, 1/160$ by keeping the spatial grid size fixed at three different levels $h = 1/16, 1/32$ and $1/64$ for the quarter five-spot flooding problem. The error calculations for both the tables have been performed at the time of water breakthrough which is given by the time at which the water saturation at $\mathbf{x}^p$ reaches a chosen threshold value. We observe (see Table 4.4) the following approximate orders of accuracy in space.

$$\|s - w\|_{L^2} = O(h), \quad \|p - r\|_{L^2} = O(h^2) \quad \& \quad \|\mathbf{v} - \boldsymbol{z}\|_{L^2} = O(h^2)$$

The $O(h)$ error in the L^2 norm for saturation s directly matches with the estimate obtained from our one-dimensional analysis in eq. (3.81). The $O(h)$ error in the gradient of the pressure p (as seen in eq. (3.51)) is also observed in the L^∞ norm $\|\mathbf{v} - \boldsymbol{z}\|_{L^\infty}$ for the velocity in Table 4.4. Moreover, the orders of accuracy in Table 4.4 for the L^2 and L^∞ errors of all the three variables s, p and $\mathbf{v}$ are consistent with the orders of accuracy obtained using an exact solution (see Table 4.1).

The order of accuracy in the L^∞ norm of the error in saturation, as presented in the upper part of the last column of Table 4.4 can be seen to reduce significantly with reduction in spatial grid size. This is the because the saturation and its L^∞ norm are both highly sensitive to minor changes in the flow and domain parameters, especially the ones whose L^∞ bounds enter the generic coefficient M used in Eq. (3.80) and in various other intermediate estimates obtained in Section 3.3. Hence the L^∞ error norms of saturation in Table 4.4 are at least an order higher than the corresponding norms for pressure and velocity, both of which are less sensitive to minor changes in the parameter space. To overcome this, much finer spatial grid size and time step size (data not shown here) need to be adopted for the

numerical solution of the transport equations.

Table 4.5 shows the L^2 error in saturation and the rate of convergence with respect to time. The results confirm that approximately a first order convergence rate in time can be obtained using this method. This compares favorably with results obtained using an exact solution (see Table 4.2) and also with the convergence rate expected from a first order time discretization scheme. We believe that with higher order time-stepping methods, the method will be able to preserve the accuracy and the expected second or third order convergence rates.

Table 4.4: Error and order for saturation, pressure and velocity at water breakthrough of a quarter five-spot polymer flooding simulation

	h	$\|s-w\|_{L^2}$	Order	$\|s-w\|_{L^\infty}$	Order
Saturation	$1/8$	4.39e−3	–	3.64e−2	–
	$1/16$	1.85e−3	1.247	1.76e−2	1.048
	$1/32$	7.84e−4	1.239	1.08e−2	0.704
	$1/64$	3.22e−4	1.284	6.86e−3	0.656
	h	$\|p-r\|_{L^2}$	Order	$\|p-r\|_{L^\infty}$	Order
Pressure	$1/8$	4.12e−3	–	1.61e−3	–
	$1/16$	9.30e−4	2.147	4.75e−4	1.761
	$1/32$	2.10e−4	2.147	1.35e−4	1.815
	$1/64$	3.85e−5	2.448	3.10e−5	2.123
	h	$\|\mathbf{v}-\mathbf{z}\|_{L^2}$	Order	$\|\mathbf{v}-\mathbf{z}\|_{L^\infty}$	Order
Velocity	$1/8$	1.18e−3	–	6.94e−3	–
	$1/16$	2.94e−4	2.005	2.98e−3	1.220
	$1/32$	7.46e−5	1.979	1.39e−3	1.110
	$1/64$	1.96e−5	1.928	6.89e−4	1.002

Table 4.5: Error and rates for saturation with time step refinement at water breakthrough of a quarter five-spot polymer flooding simulation.

Δt	$h = 1/16$		$h = 1/32$		$h = 1/64$	
	$\|s - w\|_{L^2}$	Rate	$\|s - w\|_{L^2}$	Rate	$\|s - w\|_{L^2}$	Rate
$1/20$	9.34e−3	–	8.93e−3	–	6.50e−3	–
$1/40$	4.36e−3	1.100	4.69e−3	0.923	3.48e−3	0.901
$1/80$	2.27e−3	0.941	2.51e−3	0.899	1.94e−3	0.846
$1/160$	1.25e−3	0.867	1.48e−3	0.762	1.17e−3	0.722

4.2 Study of Grid Orientation Effects[†]

4.2.1 Background

Many of these waterflooding simulations involve adverse viscosity ratio ($M_\mu = \mu_o/\mu_w$) displacement as the displacing aqueous phase usually flows more easily through the porous medium than the displaced oil phase. Such adverse mobility ratio displacements also occur during miscible injection of gas or steam into a reservoir. The adverse mobility ratio makes the displacement process hydrodynamically unstable. Any minor perturbation of the fluid fronts caused either by input data or by numerical errors triggers the formation of fingers of the more mobile displacing fluid and the physical instability causes these fingers to grow. Numerical errors are usually dependent on the orientation of the underlying computational grid and hence the solutions to these unstable displacement processes are found to be extremely sensitive to the alignment of the grid. This phenomenon is known as the grid orientation effect (GOE).

[†]Part of this section is reprinted with permission from "Robust multi-D transport schemes with reduced grid orientation effects" by Jeremy Kozdon *et al*. 2009. Transport in Porous Media, 78, 1, 47-75, doi: 10.1007/s11242-008-9281-1. Copyright by Springer Science + Business Media B.V. 2008.

Table 4.6: Simulation input data

Model parameter	Symbol	Value
Spatial grid size	$h \times k$	variable
Porosity	ϕ	1
Permeability	$\mathbf{K}$	variable
Initial resident water saturation	$s_0^{\sigma 0}$	0.21
Polymer injection concentration	c_0	variable
Surfactant injection concentration	Γ_0	variable
Oil viscosity	μ_o	12.6
Pure water viscosity	μ_w	1.26
Residual aqueous phase saturation	$s_{ra}^{\sigma 0}$	0.1
Residual oleic phase saturation	$s_{ro}^{\sigma 0}$	0.2
Critical capillary number of aqueous phase	N_{ca}	10^{-5}
Critical capillary number of oleic phase	N_{co}	10^{-5}
Parameters of capillary pressure relation [eq. (2.29)]	ω_1, ω_2	$0.1, 0.4$
Injection rate	Q	$200, 50$
Time step size	Δt	$1/50, 1/100$

This was first reported by Todd *et al*. [89]. They observed that quarter five spot simulations have two different principal axes of symmetry and accordingly the simulation grid can be aligned in two different ways. At an adverse mobility ratio, the simulations were found to converge to different solutions on these two different grid alignments. In Figure 4.2(a) the two possible grid alignments of a quarter five-spot domain with 50×50 and 71×71 grids respectively are shown inside a periodically repeating five-spot reservoir geometry. Figure 4.2(b) shows the solution level sets during a miscible displacement with an adverse mobility ratio of $M = 30$ in a quarter five-spot geometry with the two different grid alignments. The solution fronts in Figure 4.2(b) have been reprinted with permission from [90]. In order to reduce the effects seen in Figure 4.2(b), a lot of efforts have been

made to devise effective strategies. Some of these will be briefly discussed below.

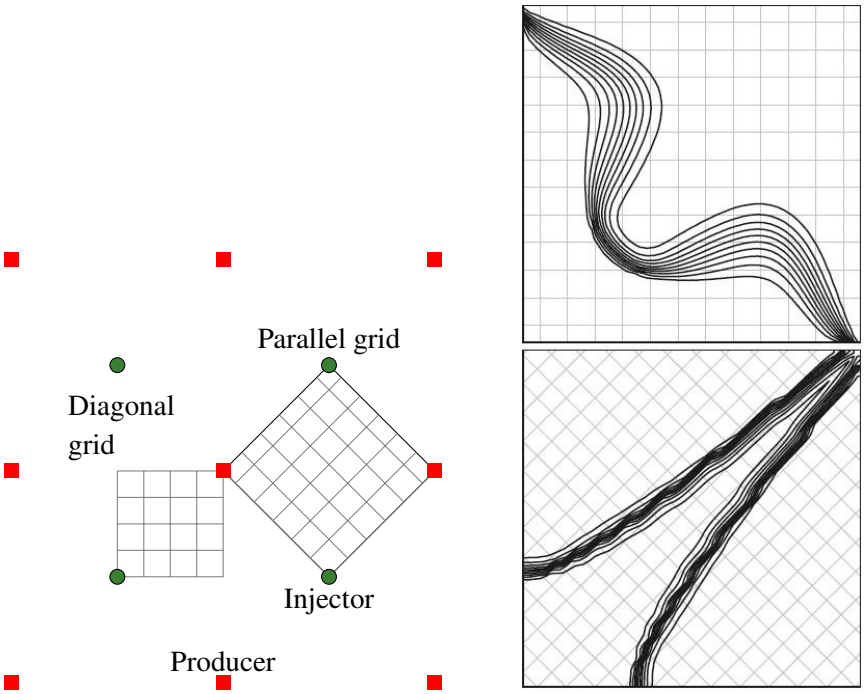

(a) Periodically repeating five spot pattern with two quarter-five spot domains

(b) Displacement fronts on diagonal and parallel grids

Figure 4.2: Flow domains with diagonal and parallel grid alignments and miscible displacement fronts in each of those grids. The subfigure (b) is reprinted with permission from [90]. Here, the effect of grid orientation on the displacement fronts is shown by simulating an adverse mobility ratio, $M = 30$, miscible displacement in a quarter five-spot geometry using a 50×50 diagonal and 71×71 parallel grid. An injector is located at the lower left corner while a producer is located at the upper right corner in both the flow domains shown in (b).

Many numerical schemes introduce some amount of numerical diffusion which can stabilize the equations of these unstable displacement processes. However, numerical diffusion is dependent on the alignment of the computational grid and hence the numerical solutions also depend on the orientation of the grid. Many of these flows also involve

molecular diffusion and physically dispersive effects induced by capillary pressure and mechanical dispersion. These physical processes have stabilizing effects and tend to reduce GOE. Unfortunately, the numerical diffusion introduced by the discretization of the convective terms using first order finite difference methods may dominate the physically dispersive terms and the stabilizing effects of these terms are not accurately modeled. There is a competition between the growth of viscous fingers due to instability and the diffusive effects (physical and numerical) that tend to smear out the sharp fronts. For the standard first order five-point finite difference methods used in reservoir simulation, discretization of the convective terms at any reasonable spatial resolution creates enough numerical diffusion to damp out viscous fingers and instead allows the growth of non-physical "numerical fingers". This effect persists even with grid refinement as long as numerical diffusion dominates over physical dispersion and diffusion. Hence it is crucial to accurately model these physical and numerical diffusive terms and develop methods that can reduce numerical diffusion in order to remove GOE.

A second order TVD (total variation diminishing) scheme and a third order ENO (essentially non-oscillatory) scheme were shown to reduce numerical diffusion and either minimize or eliminate GOE [91]. Several other higher order methods with a stabilizing diffusion term were proposed [92]. Another general approach to minimize the GOE required the use of numerical stencils explicitly chosen to remove the directional dependence of the scheme (see for example [93, 94]). In a different approach, the problem was solved on unstructured or flow aligned grids to remove apparent preferred flow directions [95, 96]. A number of nine-point difference schemes [97, 98] were developed to yield a numerical diffusion tensor that does not depend on the orientation of the computational grid (rotationally invariant) and these were found to be effective in reducing GOE. However, most of these nine-point methods do not necessarily reduce numerical diffusion and hence do not accurately resolve the stabilization caused by physically dispersive effects

with reasonable levels of spatial resolution.

In an effort to reduce GOE through accurate modeling of physically stabilizing effects, several advanced techniques like the front tracking approach [70], the finite element based schemes [85] and the modified method of characteristics approach [60, 54] were introduced. However, many of these methods are more involved and are not readily available in commercial reservoir simulation codes. In [99], linear stability analysis was used to show that the magnitude of the miscible diffusion coefficient controls the strength of the instability or the growth rate. In [100], it was deduced that transverse dispersion stabilizes perturbations and longitudinal dispersion has a critical impact on the finger growth but does not trigger actual finger formation. Some of these results were used to propose extended injection well models which reduce GOE by removing near-well perturbations that trigger unstable modes in the solution [101]. In a later work [90], some robust positive multi-D transport schemes that use conservative finite difference and finite volume methods were introduced to reduce GOE.

As explained above, the severity of GOE is an important factor to be considered in the development of any numerical method for miscible and immiscible displacement problems with adverse mobility ratio flows. Modern reservoir simulators are expected to accurately capture the effect of physical parameters such as multiscale rock permeability and porosity; effectively model the dependence of the flow on capillary pressure, relative permeability and residual saturation data; and also model the effect of dissolved chemical agents like polymer and surfactant while reducing numerical diffusion, preventing nonphysical oscillations and maintaining the speed and accuracy of computations at an acceptable level. Under the circumstances, it is often undesirable to carry out elaborate computations in order to demonstrate how a new method reduces GOE. Most of the existing techniques that test GOE, as discussed in section 4.2.2, usually involve the solution of the problem on a symmetry element of a five-spot problem by using two different orientations of a

square Cartesian grid. This can be computationally intensive for numerical methods using special grid design techniques like unstructured grids or adaptive refinement. Even with methods using regular Cartesian grids, there are often critical considerations based on efficiency, accuracy and stability of the method that direct the choice and construction of computational grids. Hence changing the orientation of the grid might adversely impact the performance of the method. Keeping these in mind, we propose a novel technique to investigate GOE for numerical methods. In this approach, GOE is studied using a fixed Cartesian grid in a five-spot reservoir by rotating the network of injector-producers wells by 45° and generating two equivalent simulation domains with parallel and diagonal grids.

4.2.2 Past approaches

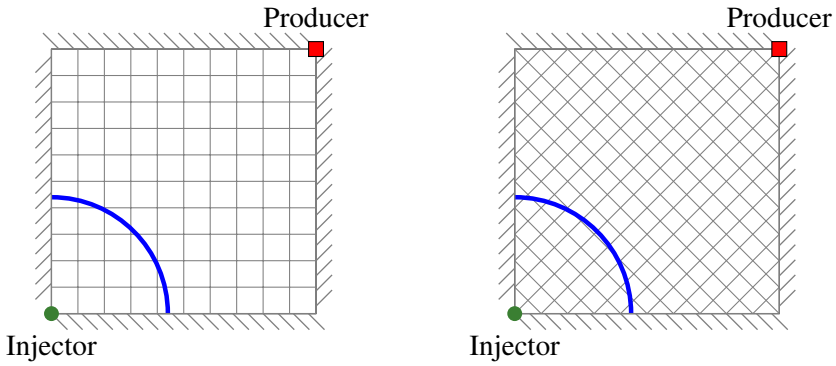

(a) Diagonal grid (b) Parallel grid

Figure 4.3: Simulation domain designs for study of grid orientation effects using existing approaches. An injector is located at the lower left corner and a producer at the upper right corner creating a quarter five-spot flood geometry. The computational grid is diagonal to the line joining the injector-producer pair in (a) and parallel to it in (b).

Most of the past studies [94, 102, 103, 91, 92, 101, 90] involving GOE have used a particular computational domain design to numerically study this phenomenon. These two

configurations have been shown in Figure 4.3(a) and Figure 4.3(b). Both the configurations comprise of a square domain that has an injection well (source) at the lower left vertex and a production well (sink) at the upper right vertex which resembles the quarter five-spot geometry as shown in Figure 3.1(a). In the first setup, depicted in Figure 4.3(a), the grid is aligned diagonal to the line joining the injector-producer pair and in the second setup, depicted in Figure 4.3(b), the grid is aligned parallely to the line joining the injector-producer pair. The construction of these two different grids requires an extra computational step to construct the mesh in addition to the numerical procedure being used, especially if a finite element method is involved. In the case of finite difference or finite volume based numerical techniques, the computational nodes are different for the two configurations. Hence the discretized equations need to be correctly formulated for each setup. This introduces an additional non-trivial calculation if non-uniform grids or unstructured meshes are employed by the numerical method being tested. It also complicates the design of grids based on stability consideration or desired accuracy of the method and might adversely affect any adaptive refinement algorithm that is being used by the numerical method.

4.2.3 New approach

In Figure 4.4, we introduce the two new configurations of five-spot flow geometries that are used in our method. We consider a square domain with an injection well or source at the center and four production wells or sinks placed in two different but symmetrically equivalent configurations. In Figure 4.4(a) and Figure 4.4(b) the dotted lines depict the largest circle that can be inscribed in the square domain and that has a diameter equal to the length of the sides of the square domain. In Figure 4.4(a) the four producers are located at the intersection of the inscribed circle and the four lines that connect the injector with the four vertices of the square domain. In Figure 4.4(b) the four producers are located on the four points where the inscribed circle intersects the sides of the square domain. Such a

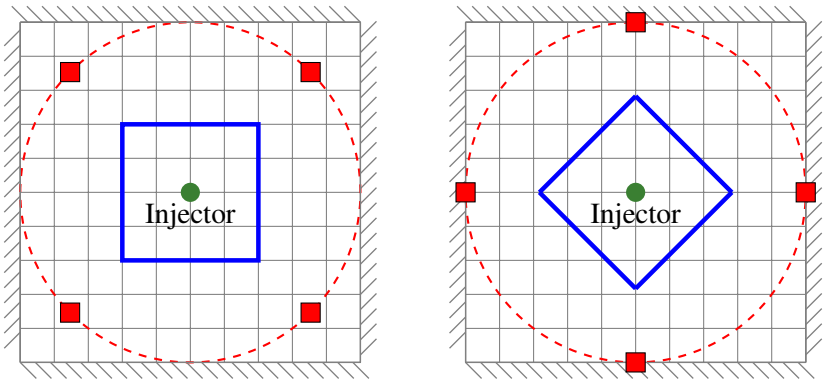

(a) Diagonal grid (b) Parallel grid

Figure 4.4: Proposed simulation domain designs for study of grid orientation effects using new approach. The flow direction is parallel to the computational grid in part (a) and diagonal to the computational grid in part (b).

design ensures that the distance between each injector-producer pair is the same and equal to half the length of the side of the square. Also, it implies that in Figure 4.4(a) the line joining the injector with any one of the producers is diagonal to the computational grid, while in Figure 4.4(b) the producers are placed in such a way that the line joining any injector-producer pair is parallel to the computational grid. In order to make these two configurations equivalent, we choose the boundary of a square as the initial position of the interface separating the displacing phase from the displaced phase. In both the configurations, each vertex of this square is located on the line connecting the injector with one of the producers. The producers are also placed in such a way that they are at the same distance from the source in both the cases. Alternatively, a circular profile can be chosen as the initial position of the separating interface. However, the discretized version of the circular profile gives rise to many irregular features on the circular boundary unless an extremely high resolution grid is used. These features may act as asymmetrical perturbations for the diagonal and parallel grid simulations causing spurious fingers which make

their comparison difficult. The square initial interface allows us to avoid this numerical difficulty and effectively, generates two equivalent configurations for a five-spot flow. The only difference is in the alignment of the computational grid.

4.2.4 GOE simulation results

In the next set of simulations we investigate if our method suffers from significant grid orientation effects. In Figure 4.5 we compare the diagonal grid solutions obtained using the geometry in Figure 4.4(a) with the parallel grid solutions obtained using the geometry in Figure 4.4(b). A homogeneous permeability field is considered. The source strength is kept fixed at $Q = 10$ with a spatial resolution of 40×40 and a time step size of $\Delta t = 1/80$. The simulations were done at a mobility ratio of $M_\mu = 20$ in order to trigger any grid alignment effects induced by the adverse mobility ratio. The water saturation contours at two different times during the simulation on both the grids are presented in Figure 4.5. The parallel flood contours are rotated counterclockwise by an angle of 45° to facilitate the comparison with the diagonal flood contours. It can be clearly seen that there are very minor differences in the features of the contours and they are qualitatively very similar. Some of the minor differences can be attributed to a graphical issue that comes up while rotating the image counterclockwise by 45° using the Image Processing toolbox of MATLAB. Rotating the matrix of water saturation values in Ω by $n\pi/2$ where n is a non-integral value produces a new matrix of water saturation values. In this process, some data points are lost while some new data points are introduced which need to be evaluated by a linear or spline interpolation process. This adjustment causes some of the minor changes observed in the parallel flood figures. For instance, four fine black lines lying diagonally across the four corners of the domain are introduced in the contour map. Also, the rotated data matrix is plotted using 4 contour lines as opposed to the 5 contour lines used in the diagonal flood figures (which are not rotated). In spite of these graphical changes, the

development of the saturation contours can be seen to follow a very similar trend in both the grid configurations. This leads us to conclude that our method suffers from negligible grid orientation effects and hence can be used reliably as a predictive numerical model.

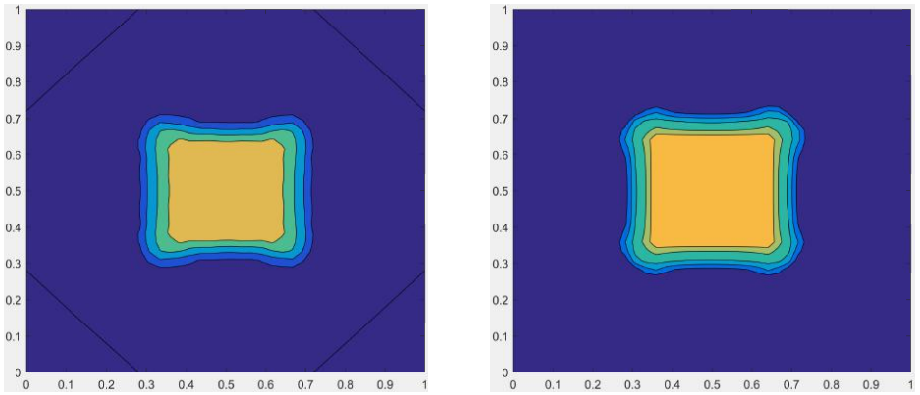

(a) $t = 200$, parallel flood

(b) $t = 200$, diagonal flood

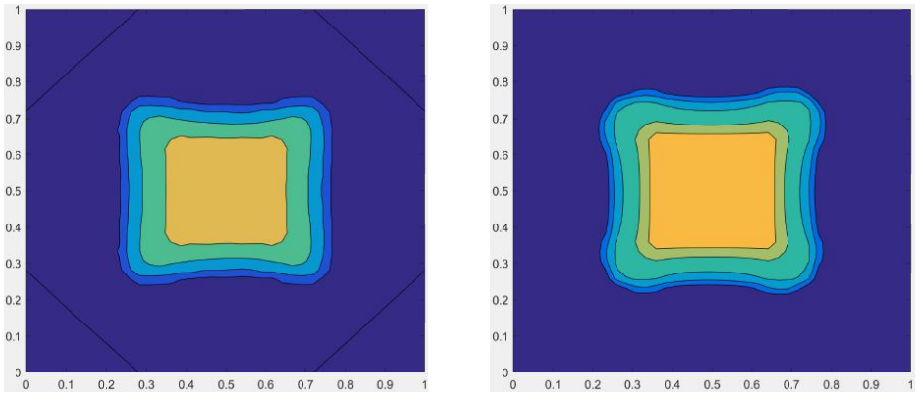

(c) $t = 400$, parallel flood

(d) $t = 400$, diagonal flood

Figure 4.5: Comparison of water saturation contours for parallel and diagonal flow simulations in a five-spot geometry with a spatial resolution of 40×40 to study the grid orientation effects. The left column corresponds to the parallel flow and the right column corresponds to the diagonal flow simulations at two different time levels, $t = 200$ and $t = 400$. Some of the minor differences are explained in the discussion in section 4.2.

4.3 Waterflood Simulations

4.3.1 Waterflooding in a quarter five-spot geometry with one block inclusion in permeability

Here we consider a special case of a porous medium that has a square block inclusion with lower permeability. We set the permeability of the shaded block (Figure 4.6(a)) to be 1000 times smaller than in the rest of the domain. We simulate the displacement of the resident oil with a waterflood using a 30×30 grid on a quarter five-spot domain, Ω. The water saturation contours inside the domain are compared at four different time levels during the displacement process (Figure 4.7). We observe that the numerical method captures the region of discontinuity of the permeability very well and the results are in excellent qualitative agreement with similar simulation studies found in the literature (see [88]). It has been shown [104, 105] that the equations for immiscible two phase displacement and the equations for miscible displacement are mathematically equivalent under certain conditions. Chavent [104] showed that the global pressure formulation for immiscible displacement is identical in form to the miscible displacement equations. Yortsos [105] used a different non-physical pressure variable to show the equivalence between two-phase immiscible displacement and single-phase miscible displacement in the presence of equilibrium adsorption. This analogy allows us to compare the evolution of saturation contours in our simulation to the evolution of concentration contours in an equivalent miscible flooding simulation [88].

4.3.2 Waterflooding in a quarter five-spot geometry with two block inclusions in permeability

Next, we consider a permeability field with two rectangular block inclusions inside the domain. As before, the permeability of the shaded blocks (Figure 4.6(b)) is set to be 1000 times smaller than in the rest of the domain. A waterflood is simulated on a

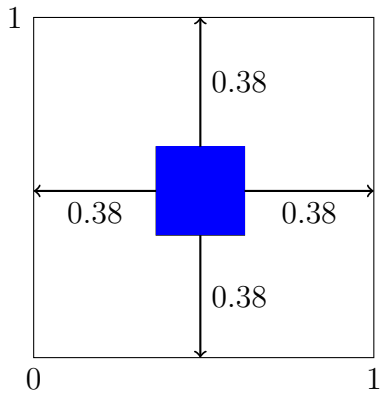

(a) Piecewise continuous permeability field with one block inclusion

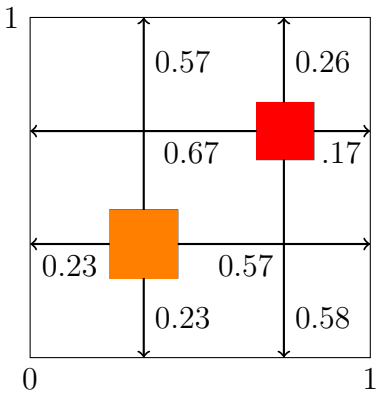

(b) Piecewise continuous permeability field with two block inclusions

Figure 4.6: Piecewise continuous permeability fields generated for qualitative validation studies

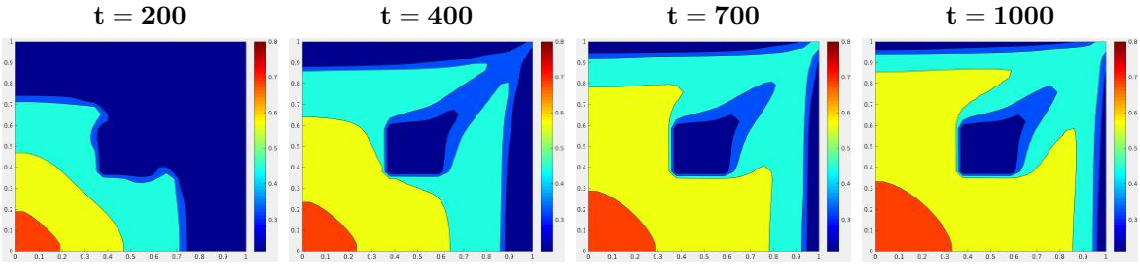

Figure 4.7: Saturation contours during a waterflood in a quarter five-spot reservoir with a spatial resolution of 30×30. The permeability field is piecewise continuous with a block inclusion at the center, as shown in Figure 4.6(a). The contours are plotted at four different time levels, $t = 200, 400, 700, 1000$.

30×30 grid and the water saturation contours inside the domain at different points of time during the flooding process are compared (Figure 4.8). We observe that the numerical method is successful in qualitatively capturing the discontinuity in the permeability data very well and the saturation contours appear to be in good qualitative agreement with what is expected based on physics.

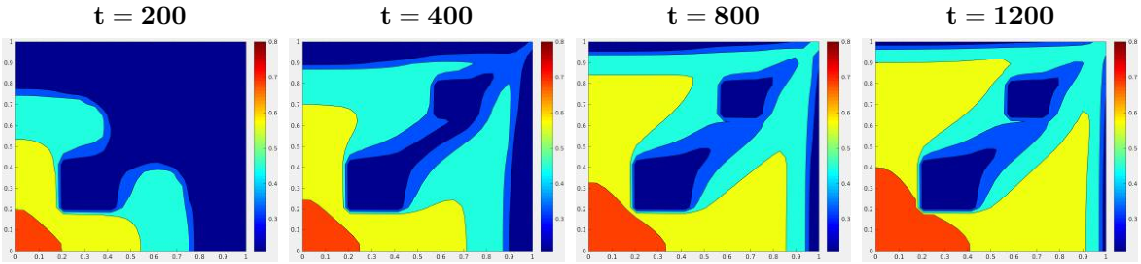

Figure 4.8: Saturation contours during a waterflood in a quarter five-spot reservoir with a spatial resolution of 30×30. The permeability field is piecewise continuous with two block inclusions, as shown in Figure 4.6(b). The contours are plotted at four different time levels, $t = 200, 400, 800, 1200$.

4.3.3 Waterflooding in a rectilinear geometry with a heterogeneous permeability field

In this simulation we consider the rectilinear flow reservoir design, as shown in Figure 3.1(b), in which the left boundary is treated as an injection well (line source) and the right boundary is treated as a production well (line sink). We consider a heterogeneous porous medium and choose the permeability function $\mathbf{K}(\mathbf{x})$ as given in [1]. The permeability function is given by

$$\mathbf{K}(\mathbf{x}) = 50\left[0.5(1-10^{-7})(\sin(6\pi\cos x)\cos(4\pi\sin(3y))-1)+1\right], \qquad (4.5)$$

and it is shown in the leftmost plot of Figure 4.9 on a 60×60 spatial grid. As shown in Figure 4.9, the more mobile fluid (water) moves along the pathways formed by interconnected zones of higher permeability. These heterogeneity driven finger formations are in agreement with the results obtained in [1] and provide further validation of our method. It is clear from the saturation contours that the regions of higher water saturation (shown in red) are trailing behind the rapidly advancing fingers. This causes premature water

breakthrough (production well starts to produce water), much before a significant amount of the residual oil has been pushed out. One of the important uses of adding polymer to the displacing phase is to inhibit the formation and growth of these fingers at an early stage by stabilizing the initial oil-water interface. This effect has been studied in more detail in one of the following simulation studies (see Figure 4.22).

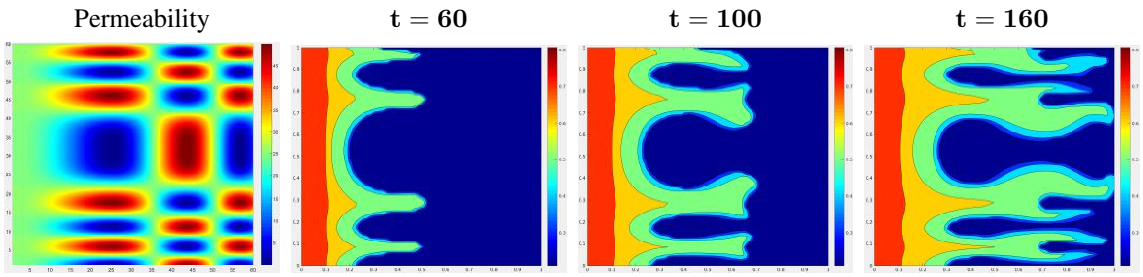

Figure 4.9: Saturation contours during a waterflood in a rectilinear geometry with 60×60 spatial resolution at three different time levels, $t = 60, 100, 160$. The heterogeneous permeability field from [1] (plotted in the leftmost figure) has been used. In the permeability plot, the red regions represent higher permeability while the blue regions represent lower permeability.

4.3.4 Waterflooding in a rectilinear geometry with a channelized permeability field

We again use a rectilinear flow domain for this study. We consider a heterogeneous porous medium and choose $\mathbf{K}(\mathbf{x})$ as in [2] in the shape of a region of high permeability that meanders from the left to the right. The permeability function is given by

$$\mathbf{K}(\mathbf{x}) = \max\left[\exp\left(-\left(\frac{y - 0.5 - 0.1\sin(10x)}{0.1}\right)^2\right), 0.01\right],$$

and it is shown in the leftmost plot of Figure 4.10 on a 60×60 spatial grid. The water saturation contours plotted at three different time levels are in good agreement with those

in [2] and provide additional validation of the method. Moreover, this simulation study demonstrates the ability of the model and the method to accurately capture flow behavior in highly channelized reservoirs or in rocks with natural faults and cracks.

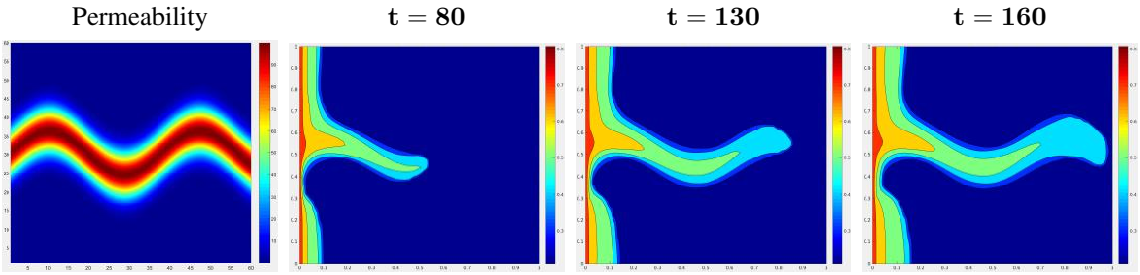

Figure 4.10: Saturation contours during a waterflood in a rectilinear geometry with 60×60 spatial resolution at three different time levels, $t = 80, 130, 160$. The permeability field from [2] (plotted in the leftmost figure), which represents a single crack porous medium, has been used. In the permeability plot, the red regions represent higher permeability while the blue regions represent lower permeability.

4.3.5 Waterflooding in a quarter five-spot geometry with the Upper-Ness (SPE10) permeability field

In this simulation we use a 30×30 block of permeability field data from the Upper-Ness region of the SPE10 benchmark problem dataset (see [106]). The original dataset is described on a regular Cartesian grid with $60 \times 220 \times 85$ $(1,122,000)$ cells. The model consists of two types of formations: a shallow-marine Tarbert formation in the top 35 layers which represents a prograding near-shore environment with relatively smooth permeability, and a fluvial Upper-Ness permeability in the bottom 50 layers. Both formations (Figure 4.11) are characterized by large permeability variations (8 to 12 orders of magnitude), but are different qualitatively. The Upper-Ness formation has more rapid variability while the Tarbert formation has a higher contrast in the permeability values. In this work,

we present results obtained using both types of permeability field data. A 30×30 Upper-Ness type permeability field (shown in Figure 4.11(a) and Figure 4.11(c)) is extracted from layer 60 of the dataset and a 30×30 Tarbert type permeability field (shown in Figure 4.11(b) and Figure 4.11(d)) is extracted from layer 5 of the dataset.

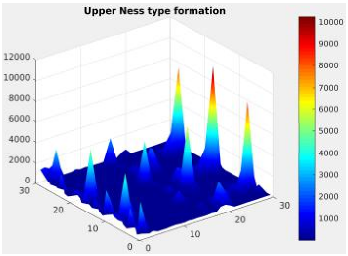

(a) Upper-Ness type permeability

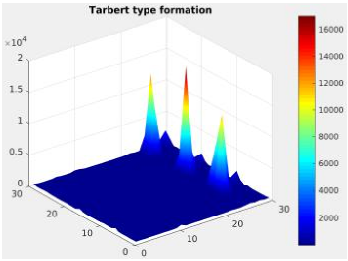

(b) Tarbert type permeability

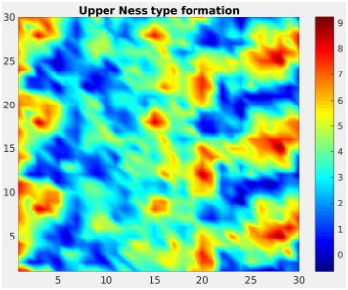

(c) Logarithmic permeability plot

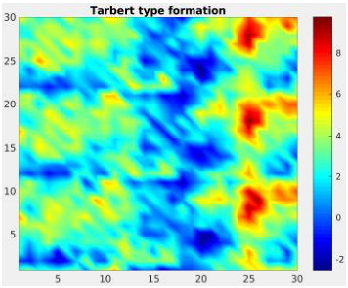

(d) Logarithmic permeability plot

Figure 4.11: Permeability plots from the SPE10 benchmark dataset on a 30×30 grid.

The simulation results are shown in Figure 4.12. As expected, the highly heterogeneous rock matrix leads to development of undesirable finger formations while the high viscosity ratio ($M_\mu = \mu_o/\mu_w = 10$) between the displaced and displacing phase leads to the growth of these viscous fingers. We observe that the displacing phase progresses towards the production well (located at $(x, y) = (1, 1)$) by sweeping through the regions of higher permeability values. The method captures the expected features of fluid flow

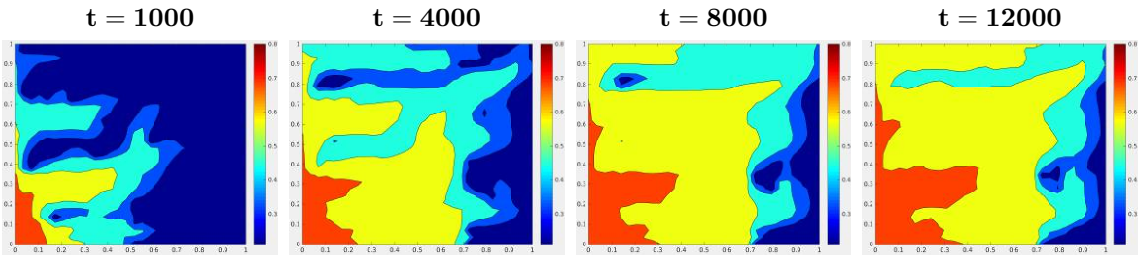

Figure 4.12: Saturation contours during a waterflood in a quarter five-spot reservoir with 30×30 spatial resolution. The permeability field is of Upper-Ness formation type (see Figure 4.11(a) and Figure 4.11(c)). The contours are plotted at four different time levels, $t = 1000, 4000, 8000, 12000$.

through the regions of high and low permeability very well and the fronts are well resolved. This provides qualitative validation of the model and the numerical method as it is able to capture the expected physical phenomenon like viscous finger formations in fully developed flows.

4.4 Polymer Flood Simulations

The displacement processes involved in tertiary oil recovery methods like polymer flooding and SP flooding are usually unstable to begin with. Hence one of the fundamental fluid dynamical mechanisms that is employed to improve oil recovery is to delay and slow down the development of these instabilities that lead to development of these nonlinear fingers since there is always a finite reservoir area that needs to be swept. The growth of these initial disturbances can be controlled by various means including the use of optimal values of the viscosity ratio [107, 108, 109]. The following set of simulations has been performed to compare the flow characteristics of a waterflood with that of a polymer flood.

4.4.1 Polymer flooding in a quarter five-spot domain with the Tarbert permeability field

In this simulation, we use the Tarbert permeability field data, shown in Figure 4.11(b) and Figure 4.11(d) on a 30×30 grid. We compare the flow patterns of two different waterflood scenarios with that of two different polymer floods. As shown in Figure 4.13, the change in viscosity ratio from $M_\mu = \mu_o/\mu_w = 10$ and $M_\mu = 5$ in the waterfloods to $M_\mu = \mu_o/\mu_a = 1.82$ and $M_\mu = 1.25$ in the two polymer floods causes a marked change in the sweeping pattern of the process. We see that in the case of waterfloods, the water phase advances through the heterogeneous formation much faster compared to the polymer floods. This is due to the fact that pure water being less viscous is more mobile. On the other hand, the polymer floods are able to achieve a much more efficient sweep of the domain. Figure 4.13 shows that the higher water saturation contours (plotted in yellow and red colors) have advanced further in the polymer floods than in the waterfloods, at the same time point. Although this makes polymer flooding a slower recovery process compared to waterflooding, the net oil recovery can be substantially more in polymer flood. This claim is supported by the last row of plots in Figure 4.13 where the saturation contours have been plotted at the time of water breakthrough in each flooding process. The polymer flood results clearly show that a larger area has been swept and also the higher water saturation levels (yellow contour) have penetrated deeper into the domain compared to the waterflood results. Between the first two columns, both showing waterfloods, the difference in mobility ratios has a significant effect in controlling the growth of the most advanced saturation contour. This is evident in the fact that the waterflood with a mobility ratio of $M_\mu = 5$ takes longer time ($t = 2418$) for water breakthrough than the time taken ($t = 1673$) by the waterflood with a higher mobility ratio of $M_\mu = 10$. However, there is little difference in the water saturation contours between the two polymer floods (see

Columns 3 and 4 in Figure 4.13) because the mobility ratios ($M_\mu = 1.82$ and $M_\mu = 1.25$) are very close.

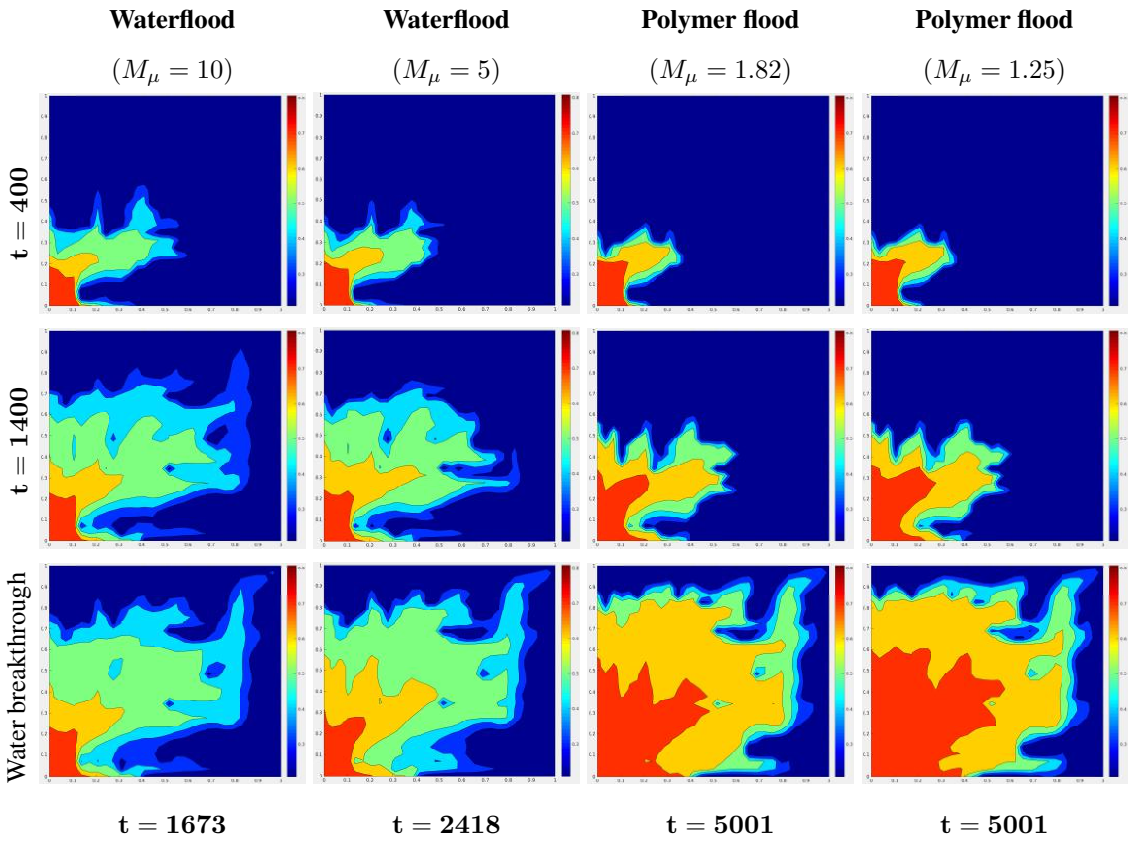

Figure 4.13: Saturation contours comparing waterfloods with polymer floods in a quarter five-spot reservoir with spatial resolution of 30×30. The simulations were carried out on the Tarbert formation type permeability field (see Figure 4.11(b)). The first two columns correspond to waterfloods with viscosity ratios of $M_\mu = 10$ and $M_\mu = 5$ while the third and the fourth columns correspond to polymer floods with viscosity ratios given by $M_\mu = 1.82$ and $M_\mu = 1.25$ respectively. The contours are plotted at three different time levels, $t = 400, 1400$ and water breakthrough. The t values below the last row of plots indicate the time levels at which water breakthrough occurs in each flood.

4.4.2 Grid refinement study with polymer flooding

In the next simulation of polymer flooding in a quarter five-spot geometry, we refine the grid over three steps - 15×15, 30×30 and 60×60. The domain has two rectangular inclusions in the permeability field such that the permeability of the shaded blocks (see Figure 4.6(b)) is 1000 times smaller than that in the rest of the domain. The viscosity ratio is kept fixed at $M_\mu = 1.67$. The water saturation contours for the polymer flooding process with three different grid sizes are given in Figure 4.14. We observe that even over the wide range of grid sizes the evolution of the fronts near the region of discontinuous permeability is captured accurately. The details in the high gradient region of the saturation contours become more prominent with the reduction in mesh size due to the additional computational points added to the domain. The qualitative agreement between the saturation contours at the same time levels but with different grid sizes provide further validation of the numerical convergence of the method.

4.5 Surfactant-Polymer Flood Simulations

In the following simulations we investigate the effect of using surfactant as a chemical flooding agent. This is done by comparing the effectiveness of surfactant and SP floods as compared to polymer flood and waterflood on the basis of the change in mobility ratio, M_λ values. The goals of these simulations are: (a) to demonstrate the robustness of the method in performing simulations of various different types of chemical flooding processes and (b) to compare the effect of these different flooding schemes on the oil recovery, the sweeping efficiency, and on controlling the growth of fingers.

4.5.1 Multiscale heterogeneity

Numerical simulations have been performed so far using several types of permeability fields to study the effect of heterogeneity and also to test the capability of the numeri-

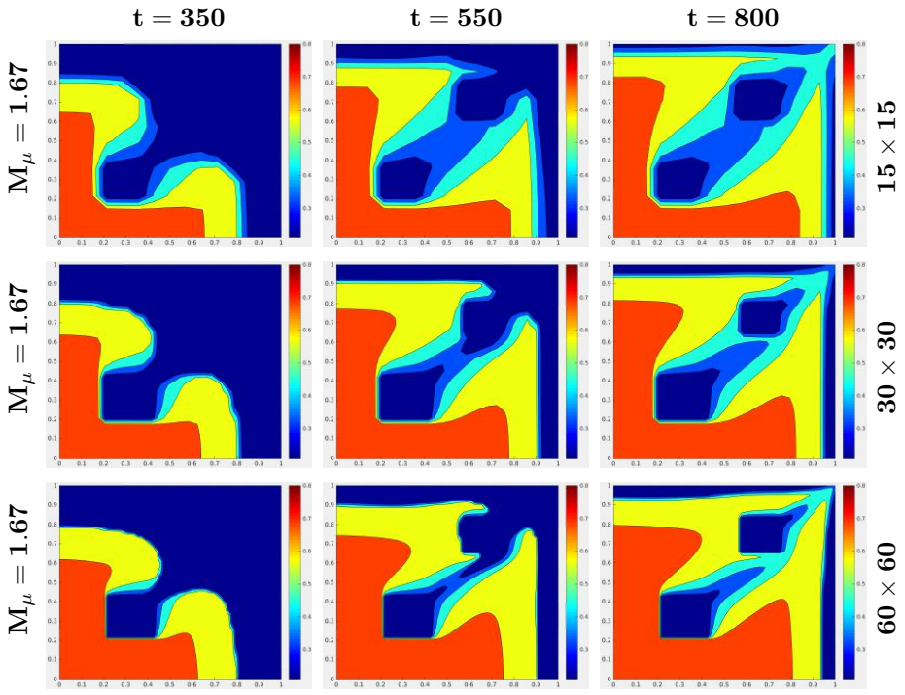

Figure 4.14: Water saturation contours during a polymer flood (viscosity ratio, $M_\mu = 1.67$) in a quarter five-spot geometry with a piecewise continuous permeability field containing two block inclusions (see Figure 4.6(b)). The contours have been plotted at three different time levels, $t = 350, 550, 800$. The simulations were performed on three different spatial resolutions : Row 1 - 15×15, Row 2 - 30×30 and Row 3 - 60×60.

cal method to produce accurate solutions. These include homogeneous fields, piecewise discontinuous fields and also sections of the well known SPE10 permeability field data which model the Upper Ness type and the Tarbert type rock formations. In this section, we have also used a scalar log-normal absolute permeability field, $\mathbf{K}(\mathbf{x})$ as a model for multiscale rock heterogeneity. First we generate a Gaussian random field, $\xi(\mathbf{x})$ which we assume to be stationary (translational invariance of covariance function), isotropic (rotational invariance of covariance function) and fractal (self-similar). Hence, the distribution

is characterized by a zero mean and a covariance function of the form

$$cov(\xi(\mathbf{x_1}), \xi(\mathbf{x_2})) = \chi \, |\mathbf{x_1} - \mathbf{x_2}|^{-\beta}, \; 0 < \beta < \infty, \tag{4.6}$$

where χ is an appropriate proportionality constant and the scaling exponent β, called the Hurst coefficient, controls the nature of heterogeneity. With an increase in β the covariance function decays faster and hence heterogeneities in the shorter length scales become pronounced. The LABTRAN-GEO methods, [110] are computationally efficient methods to generate Gaussian fields with a covariance function given by the power law, eq. (4.6). From this multiscale Gaussian field, we construct an absolute permeability field and a porosity field as

$$\mathbf{K}(\mathbf{x}) = k_0 \exp\left(\varpi \xi(\mathbf{x})\right), \tag{4.7}$$

$$\phi(\mathbf{x}) = \phi_0 + \bar{\varphi}\xi(\mathbf{x}), \; \bar{\varphi} > 0, \tag{4.8}$$

where k_0 is a chosen threshold, $0 < \varpi \leq 1$ is a chosen scaling exponent, ϕ_0 is the cutoff value and $\bar{\varphi}$ is a normalizing factor that is chosen to ensure that the porosity lies in the following range, $0.05 \leq \phi(\mathbf{x}) \leq 0.35$. The mean $\langle \mathbf{K} \rangle$ and variance σ_k^2 of the log-normal field $\mathbf{K}$ are set by the coefficients k_0 and ϖ. With change in ϖ we get different values for the Coefficient of Variation CV for permeability, (CV_k), and porosity, (CV_ϕ). For the permeability field $\mathbf{K}$, this is defined by $CV_k = \sigma_k / \langle \mathbf{K} \rangle$. This dimensionless number CV_k can be thought of as a measure of the heterogeneity of the field. Similar formulations have been adopted in [111, 112, 113].

In Figure 4.15(a) we present an example of such a stationary, isotropic and multiscale Gaussian field calculated with zero mean, $\beta = 0.5$ and $\chi = 1/(1 - 2^{-\beta})$. In Figure 4.15(b) we present a lognormal permeability field generated from this Gaussian field with $k_0 =$

3.4253 and $\varpi = 1$. In our studies here, uniform porosity has been used.

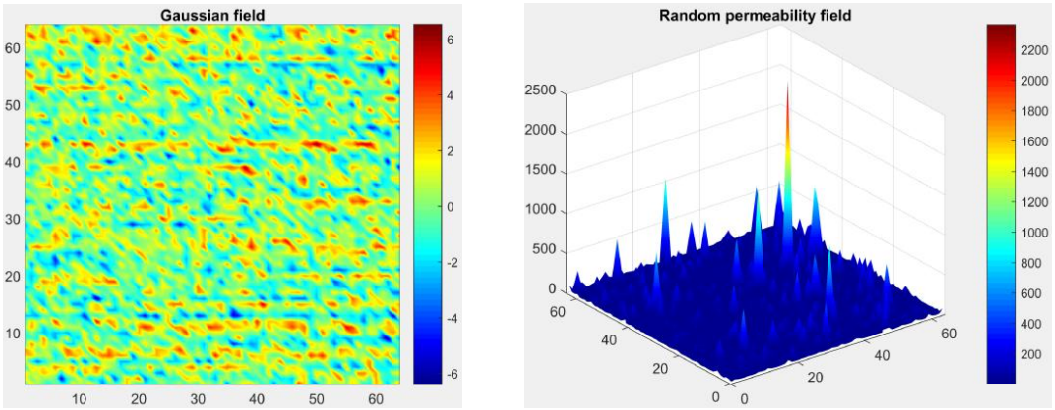

(a) Gaussian field (b) Log-normal permeability

Figure 4.15: Stationary, isotropic, fractal Gaussian field, $\xi(\mathbf{x})$ [shown in (a)] used for generating a log-normal permeability, $\mathbf{K}(\mathbf{x})$ [shown in (b)] using eq. (4.7). Both fields are of size 64×64. Higher values are plotted in red and lower values in blue.

4.5.2 Surfactant-polymer flooding in a quarter five-spot geometry

The first two sets of simulations for surfactant-polymer flooding are performed in a quarter five-spot reservoir fitted with a 32×32 grid. A multiscale, stationary, isotropic Gaussian permeability field (Figure 4.16(a)) generated using the method outlined in Section 4.5.1 has been used to construct a scalar, log-normal permeability field (Figure 4.16(b)) with $k_0 = 3.44253$, $\varpi = 1.0$ ($CV_k = 0.5$).

The first set of simulations, presented in Figure 4.17, provides a comparison of water saturation surface plots between four different types of flooding schemes at three different time levels. The first column represents waterflooding ($M_\lambda = 2.89$), the second represents surfactant flooding ($M_\lambda = 3.12$), the third and fourth columns represent two different schemes of SP flooding ($M_\lambda = 3.06$ and $M_\lambda = 1.96$) which differ only in the amount

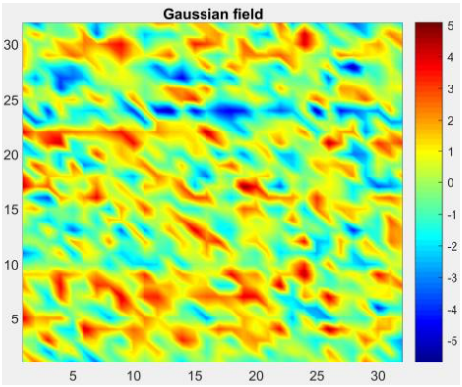

(a) Gaussian field

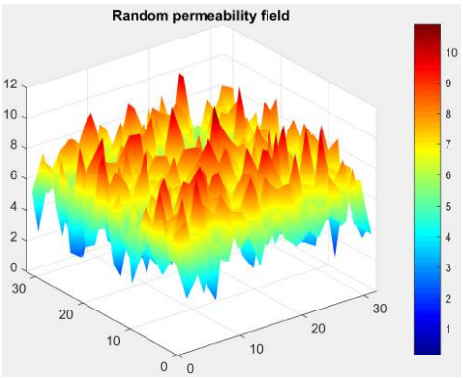

(b) Logarithmic plot of the permeability field

Figure 4.16: Multi-scale, stationary, isotropic Gaussian distribution [shown in (a)] which is used to generate a scalar log-normal permeability field [shown in (b)] of spatial resolution 32×32.

of polymer present in the displacing phase. In Figure 4.18, we compare the surfactant concentration surface plots and the polymer concentration surface plots for these floods. Specifically, the first and the second columns show the surfactant concentration plots during the surfactant flood and the second SP flood ($M_\lambda = 1.96$) while the third and fourth columns present the polymer concentration surface plots between the two different SP floods.

The difference in the surface plots between the waterflood and the surfactant flood simulations is explained by the combined effect of the surfactant on the interfacial tension and the relative permeability of the aqueous phase. This allows more resident oil to be swept out as seen in the first two columns. We see that the regions with higher water saturation values (i.e. regions where most of the oil has been pushed out), indicated in the darker shades of red, have advanced further into the domain for the surfactant flood than for the waterflood at comparable times. There is not much difference between the saturation surface plots of the surfactant flood (2nd column) and the first SP flood (3rd

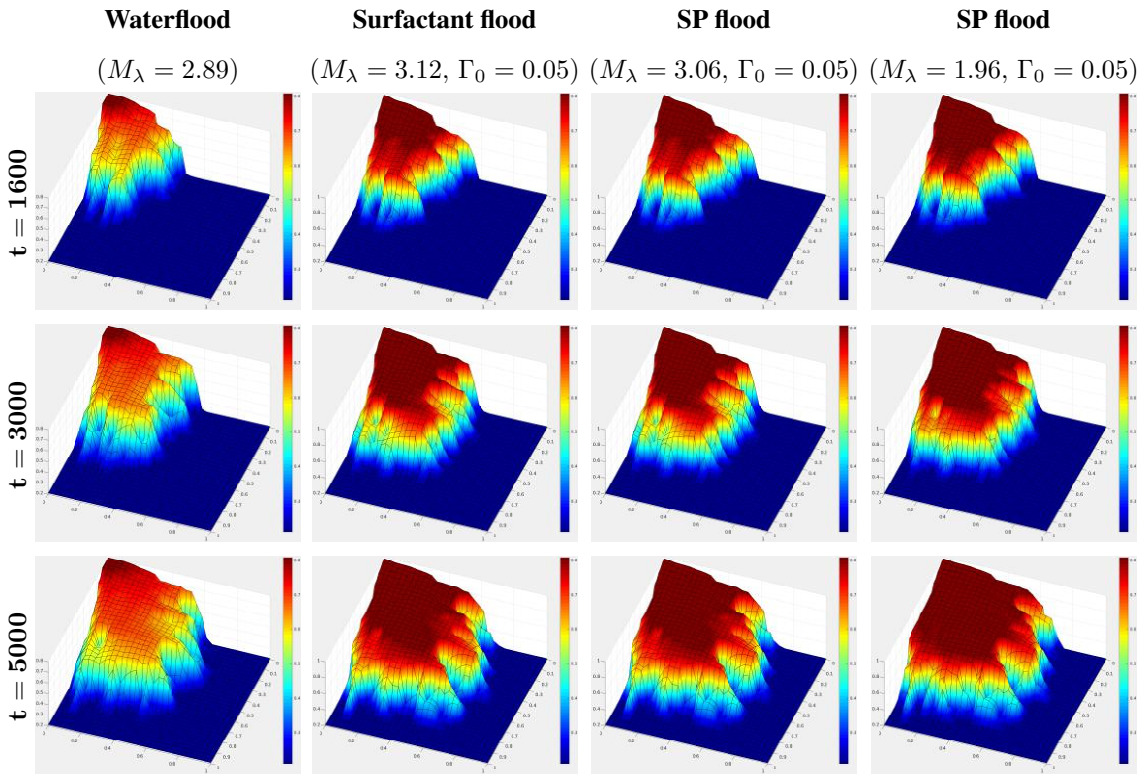

Figure 4.17: Comparison of water saturation surface plots in a quarter five-spot reservoir with spatial resolution of 32×32 during four different floods - waterflood, surfactant flood and two SP floods. The mobility ratios are $M_\lambda = 2.89, 3.12, 3.06$ and 1.96, respectively for the four floods. $\Gamma_0 = 0$ for the waterflood and $\Gamma_0 = 0.05$ for the other three floods. The permeability field used is given in Figure 4.16. The surface plots are shown at three different time levels, $t = 1600, 3000, 5000$.

column), in spite of the fact that polymer is added to the system in the SP flooding. This is because, the addition of polymer does not cause an appreciable change in the mobility ratio ($M_\lambda = 3.12$ and $M_\lambda = 3.06$ respectively) between these two flooding schemes. Hence these two flooding schemes produce very similar results and this serves as an additional validation of the robustness of the model. The difference in the saturation surface plots between the two SP floods is primarily observable in the features near the advancing fronts (i.e. near the edges of the surface plots). The higher water saturation values can be seen to

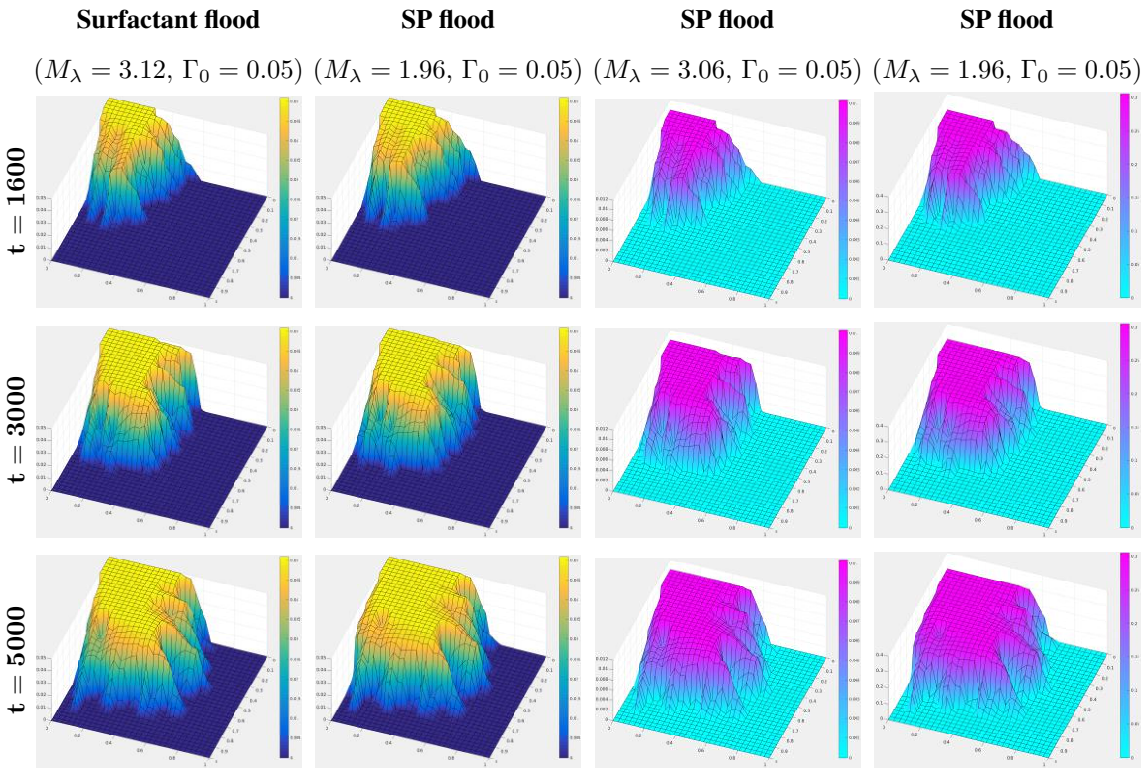

Figure 4.18: Comparison of surfactant (Columns 1 & 2) and polymer (Columns 3 & 4) concentration surface plots in a quarter five-spot reservoir with spatial resolution of 32×32 during three different floods. The mobility ratio $M_\lambda = 3.12, 1.96$ for the first two columns while $M_\lambda = 3.06, 1.96$ for the third and fourth columns, respectively. $\Gamma_0 = 0.05$ is fixed for all the simulations. The permeability field given in Figure 4.16 has been used. The surface plots are shown at three different time levels, $t = 1600, 3000, 5000$.

have spread wider in the second SP flood (fourth column) than in any of the other floods. This means that the gradient of the water saturation is the largest in the second SP flood as the frontal region is spread over the thinnest area among all the four floods. Even in Figure 4.18, the surfactant and polymer concentration surface plots of the second SP flood, as seen in the second and fourth columns respectively, have a higher gradient near the frontal region as compared to the surfactant flood or the first SP flood. This is expected as the combination of polymer and surfactant used in this particular flood gives rise to the lowest mobility ratio ($M_\lambda = 1.96$). As a result, the progress of the finger formations is

arrested to a higher extent and also a higher percentage of the resident oil is mobilized.

Some of the effects, discussed above, seem to be marginally observable in the surface plots, but the differences in the oil recovery efficiency and the change in the water cut at the production well with time, as presented in Figure 4.19, strongly support these claims. The oil recovery efficiency, E_R (in $\%$) is defined as the fraction of resident oil that is recovered in a flooding process. Figure 4.19(a) shows the recovery efficiency of four types of chemical flooding schemes with different endpoint mobility ratios M_λ and shock front mobility ratios M_s : (a) waterflood ($M_\lambda = 14.43$, $M_s = 3.78$), (b) surfactant flood ($M_\lambda = 14.77$, $M_s = 3.90$), (c) SP flood ($M_\lambda = 2.35$, $M_s = 0.72$) and (d) SP flood ($M_\lambda = 2.98$, $M_s = 0.93$). The large drop in mobility ratios between the first two ($M_\lambda = 14.43$ and 14.77) and the last two ($M_\lambda = 2.35$ and 2.98) floods is used in order to enhance the difference in their efficiencies. As expected, in Figure 4.19(a) we see that the oil recovery efficiency increases with the decrease in the mobility ratio of the scheme. The curves coincide initially and start to diverge as soon as water breakthrough is achieved in each flood. The respective breakthrough times are directly influenced by the mobility ratio of each flood, thus causing the flooding scheme with a higher M_λ to breakthrough earlier. Additionally, the distinct bimodal trend in the efficiency curves can be easily explained by studying the shock front mobility ratios M_s. The M_s values of the waterflood ($M_s = 3.78$) and the surfactant flood ($M_s = 3.90$) can be used to categorize them as dynamically unstable ($M_s > 1$) displacement processes which explains the abrupt drop in their respective recovery efficiency curves. On the other hand, the M_s values of the two SP floods ($M_s = 0.72, 0.93$ respectively) clearly classify them as dynamically stable ($M_s < 1$) displacement processes which explains their superior recovery efficiencies.

Figure 4.19(b) shows the time dependence of the water cut or the aqueous phase saturation (s_a) at the production well for the same four chemical floods. In Figure 4.19(b), the water cut curves follow the same trend. The water cut is constant and the same for

each flood until breakthrough happens. The surfactant flood, with the highest mobility ratio, achieves breakthrough earlier than all the other floods, and also produces the highest fraction of water for almost the entire time. This can be attributed to the dual effect of the surfactant. It increases the relative permeabilities and reduces the capillary pressure barrier, thus facilitating the fluid flow. It can also be seen that the SP flood with the lower mobility ratio ($M_\lambda = 2.35$) always has a lower water cut in comparison to the SP flood with a higher mobility ratio ($M_\lambda = 2.98$), which supports the trend in their relative oil recovery efficiencies as well.

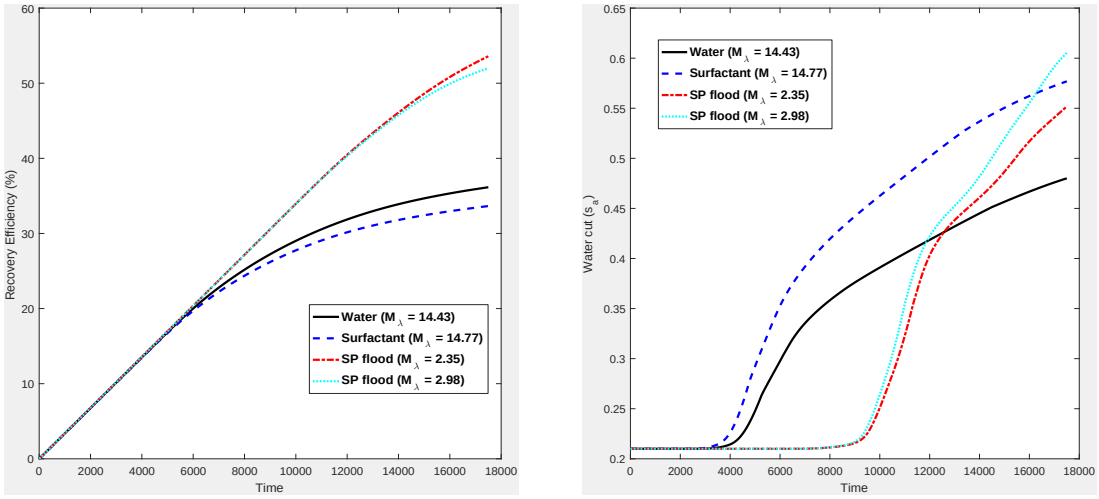

(a) Recovery efficiency versus time

(b) Water cut versus time

Figure 4.19: Effect of the different flooding schemes on oil recovery efficiency and water cut in a quarter five-spot geometry with a heterogeneous permeability field given by Figure 4.16.

In Figure 4.20, the second set of simulations is presented which compares water saturation surface plots between four different types of flooding schemes at three different time levels. The first column represents waterflooding ($M_\lambda = 2.89, \Gamma_0 = 0$), the second column represents surfactant flooding ($M_\lambda = 3.04, \Gamma_0 = 0.1$), the third and fourth

columns represent two different configurations of SP flooding ($M_\lambda = 1.91, \Gamma_0 = 0.01$ and $M_\lambda = 1.92, \Gamma_0 = 0.1$). In Figure 4.17 we study the effect of polymer by changing the mobility ratios while keeping Γ_0 fixed. Here, we study the effect of surfactant by varying Γ_0 between the two SP floods. In Figure 4.21 we compare the surfactant concentration surface plots for three floods. Specifically, the first column represents a surfactant flood ($M_\lambda = 3.04, \Gamma_0 = 0.01$) while the second and the third columns show the surfactant concentration plots during the two SP floods.

As observed in Figure 4.20, the surfactant flood and both the SP floods perform better than the waterflood in recovering oil from the reservoir. This is reflected in the saturation surface plots of all the three floods where the region of higher saturation values (shown in the darker shade of red) have advanced further than that in the waterflood at comparable time levels. Even at water breakthrough, this is clearly visible. The other striking observation is that the surfactant flood and the two SP floods take somewhat comparable times while the waterflood takes significantly longer for water breakthrough. The surfactant flood is expected to achieve a quicker breakthrough as it has a higher mobility ratio than the waterflood, but the two SP floods achieve breakthrough earlier in spite of having lower mobility ratios than waterflood. This is because the surfactant mobilizes a larger percentage of the resident oil (by lowering capillary pressure and increasing relative permeabilities) and hence in Figure 4.20, the interaction of the heterogeneity field used and the flood configuration allows the water saturation surfaces with higher values ($s_a \geq 0.5$) to breakthrough earlier than in the waterflood. This kind of flow behavior is possible partly because the difference in mobility ratios between the floods in Figure 4.20 is not very high.

The addition of polymer arrests the progress of the displacing phase along the heterogeneity induced "fingers" and this is visible near the advancing fronts (i.e. along the edges of the surface plots) if we compare the surfactant flood figures with any of the two SP flood figures. It is also confirmed by comparing the surfactant concentration surface

plots, given in Figure 4.21, especially at $t = 6000$ and at water breakthrough. On the other hand, addition of surfactant while keeping the amount of polymer fixed does not have a significant impact, as seen in the last two columns of Figure 4.20. The saturation surface plots are almost indistinguishable and these two floods also take very similar times to reach water breakthrough. Similarly, the second and the third columns of Figure 4.21 show that the surfactant concentration surface plots for these two SP floods are almost the same indicating that they depend weakly on the concentration of the surfactant for this particular simulation. Overall, in the last two sets of simulations we observe that, even in the presence of both polymer and surfactant, the method is able to produce qualitatively accurate water saturation, polymer concentration and surfactant concentration plots through the heterogeneous permeability field while capturing the intricate details of the advancing fronts.

4.5.3 Surfactant-polymer flooding in a rectilinear geometry

In the final simulation, we compare four different types of floods in a rectilinear geometry with a spatial resolution of 60×60. These are waterflood ($M_\lambda = 14.43, M_s = 3.78, \Gamma_0 = 0$), polymer flood ($M_\lambda = 2.60, M_s = 0.90, \Gamma_0 = 0$), surfactant flood ($M_\lambda = 15.27, M_s = 4.03, \Gamma_0 = 0.05$) and SP flood ($M_\lambda = 3.06, M_s = 0.92, \Gamma_0 = 0.05$). The heterogeneous permeability field given by eq. (4.5) has been used. Figure 4.22 shows the water saturation contours at three different time levels. Figure 4.23(a) shows the oil recovery efficiency with time for all the four floods and Figure 4.23(b) shows the water recovery efficiency versus time.

The first important point to notice is the difference in time required to achieve water breakthrough for each of these floods. These time levels are provided below each of the water breakthrough contours in Figure 4.22. The addition of polymer increases the viscosity of the displacing aqueous phase making it slower. For the purpose of demonstration,

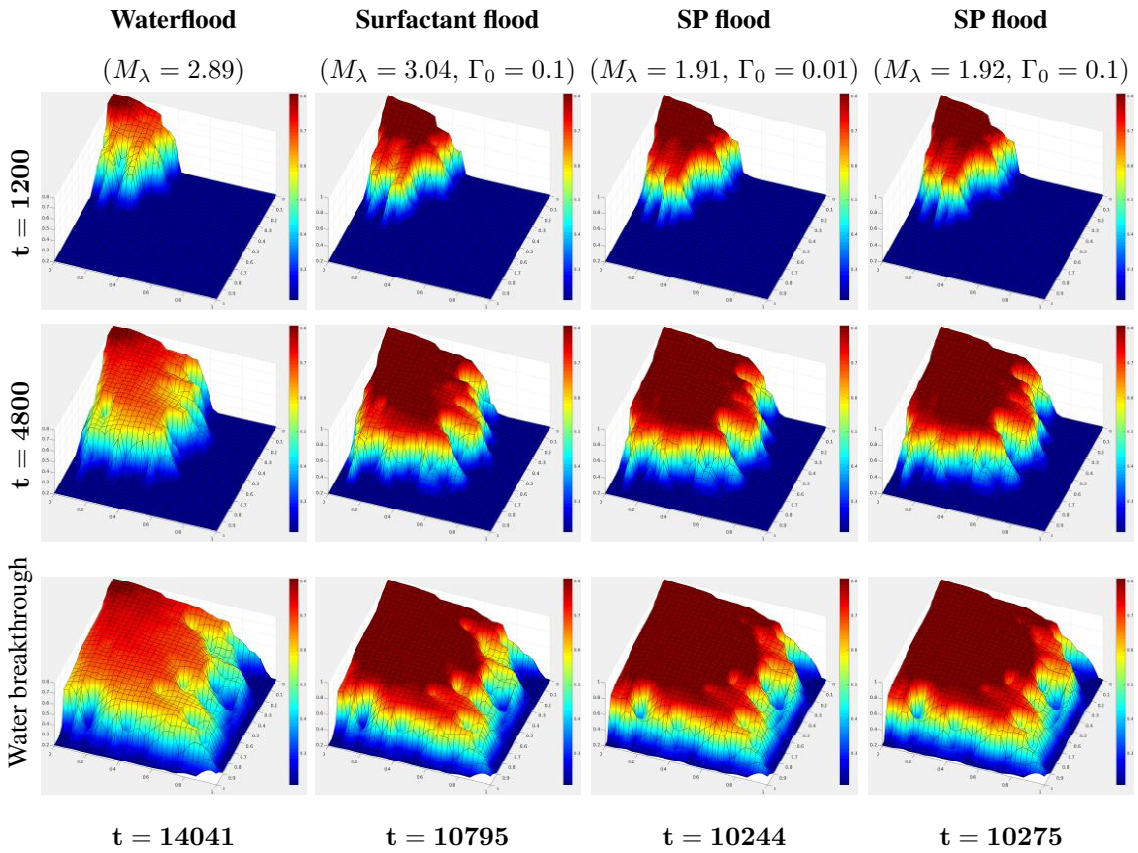

Figure 4.20: Comparison of water saturation surface plots in a quarter five-spot reservoir with spatial resolution of 32×32 during four different floods - waterflood, surfactant flood and two SP floods. The mobility ratio for the four floods were $M_\lambda = 2.89, 3.04, 1.91, 1.92$. $\Gamma_0 = 0.1$ for the surfactant flood (second column) and the second SP flood (fourth column) and $\Gamma_0 = 0.01$ for the first SP flood (third column). The permeability field used is given in Figure 4.16. The surface plots are shown at three different time levels including the plots at water breakthrough for each flood in the last row. The respective times at which water breakthrough happens for each flood is given below the last row of plots.

a very large drop in the mobility ratio from $M_\lambda = 14.43, 15.27$ (waterflood and the surfactant flood) to $M_\lambda = 2.60, 3.06$ (polymer and the SP flood) has been used to capture this effect. Hence the polymer flood takes the longest time to achieve water breakthrough as the polymer laden displacing phase becomes highly viscous. The addition of surfactant has the twin effect of lowering the capillary pressure barrier and increasing the relative per-

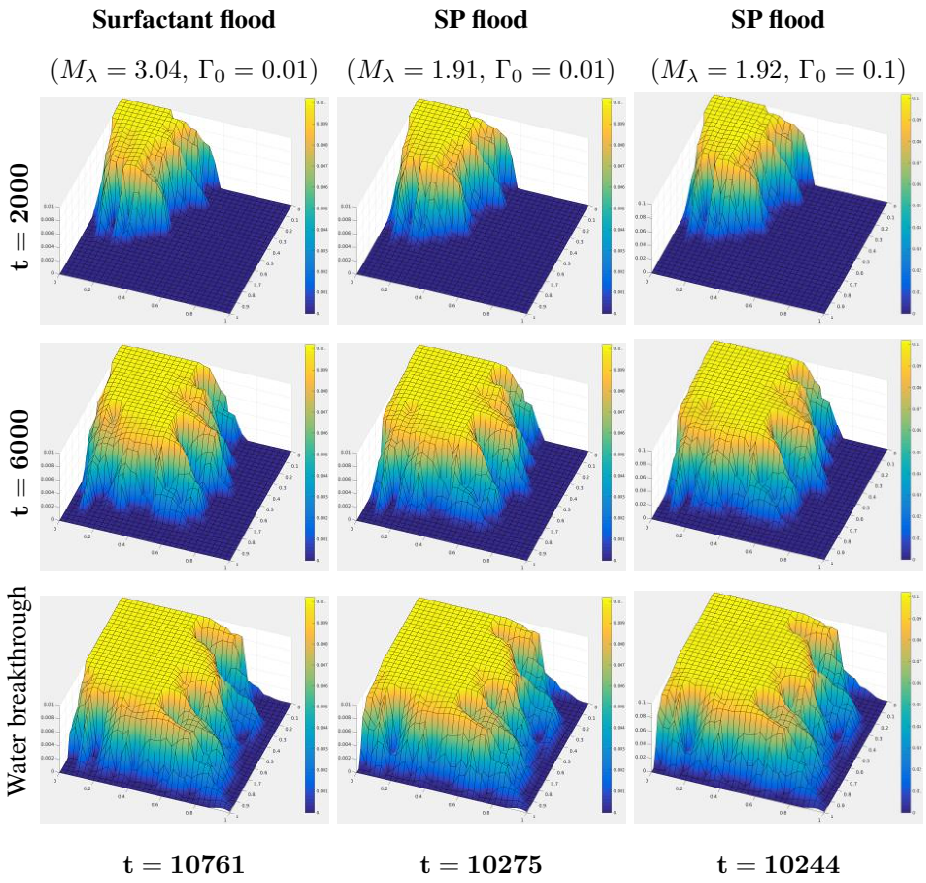

Figure 4.21: Comparison of surfactant concentration surface plots in a quarter five-spot reservoir with spatial resolution of 32×32 during three different floods. The mobility ratio was $M_\lambda = 3.04$ for the surfactant flood (Column 1) and $M_\lambda = 1.91, 1.92$ for the two SP floods (Columns 2 and 3). $\Gamma_0 = 0.01$ for the first two columns and $\Gamma_0 = 0.1$ for the third column. The permeability field given in Figure 4.16 has been used. The surface plots are shown at three different time levels including the plots at water breakthrough for each flood in the last row. The respective times at which water breakthrough happens for each flood is given below the last row of plots.

meability for the displacing phase and hence this makes it easier for the displacing phase to penetrate into the reservoir. In the SP flood, the dual effect of polymer and surfactant compete with each other and hence this flood achieves water breakthrough earlier than the polymer flood. However, for the particular setup chosen in this experiment, the surfactant in the system cannot completely overcome the slowdown caused by the polymer and hence

pure waterflooding achieves water breakthrough earlier than both the polymer and the SP flooding. As expected intuitively, the surfactant flooding is the fastest. This is because the aqueous solution of surfactant is more mobile compared to pure water.

The effect of polymer in stabilizing the oil-water interface and thus reducing the growth of fingers can be seen as well in Figure 4.22. From the first two rows in Figure 4.22, it is evident that the growth of fingers slows down the most in the polymer flood, followed by the SP flood, the waterflood and the surfactant flood, at the same time level. This in turn ensures that by the time water breaks through a polymer flood achieves an improved sweep compared to the waterflood. As seen in the first two columns of the last row of Figure 4.22, at water breakthrough the contours with higher levels of water saturation (shown in yellow and red) are trailing in the case of the waterflood to those of the polymer flood. In Figure 4.23(a), the oil recovery curves for the waterflood and the polymer flood also support this observation. The oil recovery efficiency of the polymer flood is more than that of the waterflood and hence the water recovery efficiency of the polymer flood is lower as well (in Figure 4.23). The water breakthrough times of all the floods can be clearly identified from the points in Figure 4.23 where the curves abruptly depart from their steady coincidental trajectory. These times are also in agreement with the data obtained from the water saturation contour plots given in Figure 4.22.

The effect of surfactant can be observed in the surfactant flood and the SP flood simulations shown in the last two columns of Figure 4.22. The surfactant flood seems to enhance the finger formation, as can be seen by comparing the first and the third columns of Figure 4.22 where the fingers advance faster in surfactant flood. The surfactant flood also has a lower oil recovery efficiency than the waterflood (see Figure 4.23(a)). This result is not surprising if we compare the mobility ratios for each of the two floods. The surfactant flood has a higher mobility ratio than the waterflood and hence has a lower oil recovery efficiency. This is also supported by the water recovery curves of the waterflood and the

surfactant flood in Figure 4.23(b). The SP flood on the other hand combines the twin effect of the polymer and the surfactant and hence not only are the growth of fingers arrested, but also an improved sweep of the reservoir is achieved in comparison to the waterflood and the surfactant flood. Also, in Figure 4.23(a), it can be seen that oil recovery curve for the SP flood steadily surpasses that of the surfactant flood, but trails that of the polymer flood. While this might look counterintuitive, a comparison of the mobility ratios of the polymer flood ($M_\lambda = 2.60$) and the SP flood ($M_\lambda = 3.06$) explains this phenomenon. From the standpoint of physics, this can be explained as well. The polymer flood has a lower mobility ratio and hence is able to achieve a better areal sweep of the reservoir. This means that the finger formations slowly become thicker and the resident oil in a larger area is swept through. Also, with the passage of time after water breakthrough, the region where the finger tips intersect with the line sink becomes larger compared to the SP flood, allowing for more discharge of oil. On the other hand, the surfactant in the SP flood tries to facilitate the movement of the more mobile displacing phase through the pathways formed by the finger formations. Hence, even though a larger percentage of oil is made available for recovery (in the SP flood), this is recovered only at the narrow tips where the fingers intersect with the line sink (see Figure 4.22). The oil in the regions not yet swept by the displacing phase is not recovered. The better oil recovery efficiency of the polymer flood over the SP flood can be attributed to a combination of all these effects. The higher water recovery efficiency of the SP flood given in Figure 4.23(b), compared to the polymer flood, supports these observations. Moreover, the bimodal trend in the oil recovery efficiency curves separating the polymer flood ($M_s = 0.90$) and the SP flood ($M_s = 0.92$) from the waterflood ($M_s = 3.78$) and the surfactant flood ($M_s = 4.03$) is reflected in their respective shock front mobility ratio M_s values which can be used to categorize them as dynamically stable ($M_s < 1$) and dynamically unstable ($M_s > 1$) processes.

Overall, it appears from our simulations that a careful study of the mobility ratios and

the reservoir properties are critical for designing an efficient flooding scheme that can maximize recovery.

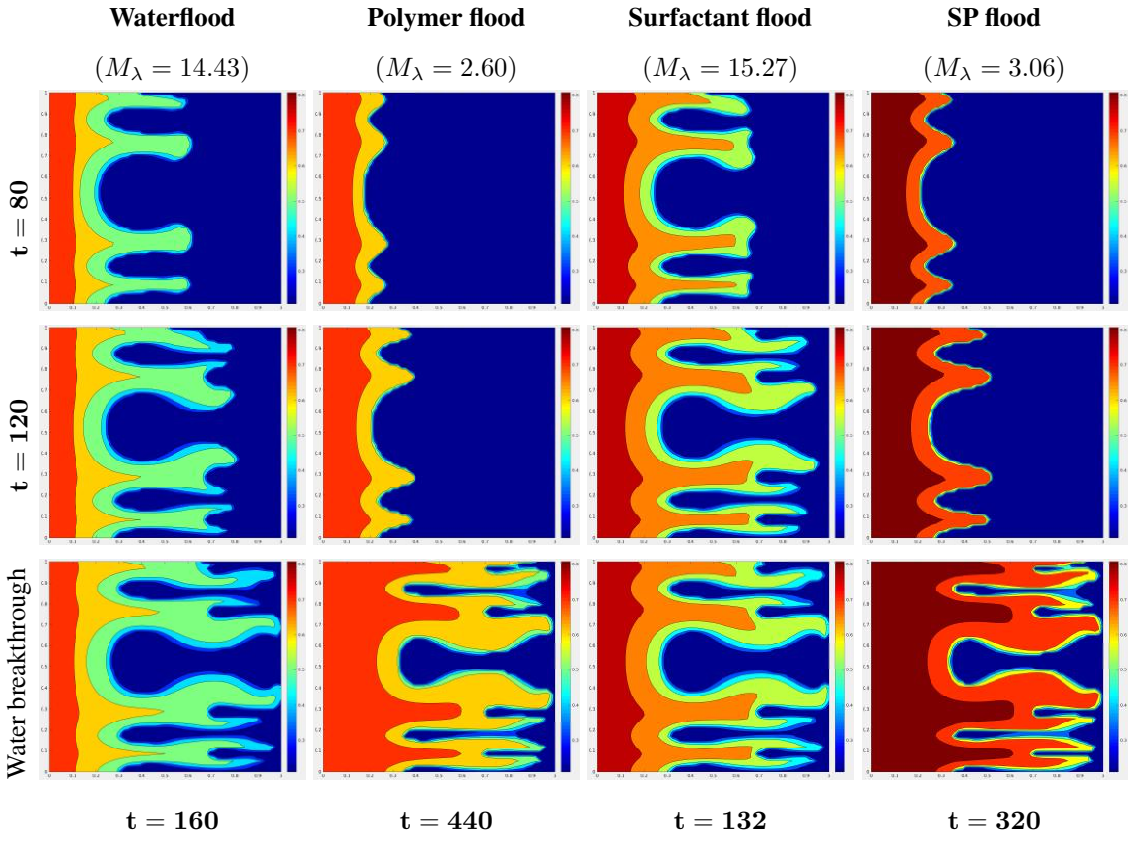

Figure 4.22: Comparison of saturation contours during four different types of chemical floods in a rectilinear geometry with 60×60 spatial resolution at three different time levels. The heterogeneous permeability field from [1] (plotted leftmost in Figure 4.9) has been used. The saturations contours have been presented at $t = 80$ (first row), $t = 120$ (second row) and at water breakthrough in each of the different floods, with the corresponding time levels mentioned below each figure.

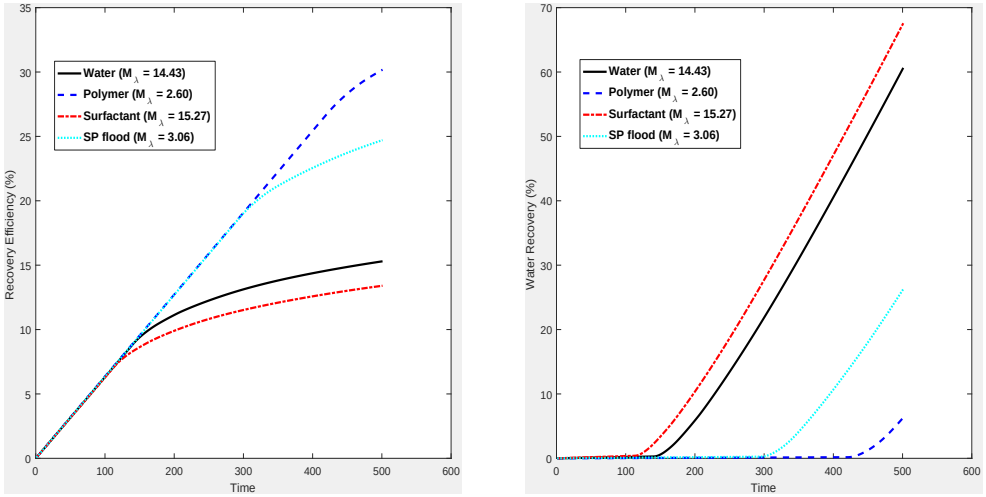

(a) Oil recovery versus time

(b) Water recovery versus time

Figure 4.23: Effect of the different flooding systems on oil recovery and water recovery in a rectilinear geometry with a heterogeneous permeability field from [1] (plotted leftmost in Figure 4.9).

5. CONCLUSIONS AND FUTURE DIRECTIONS

5.1 Conclusions

In this dissertation, we have studied immiscible two-phase, multi-component, incompressible flows in porous media that arise in the context of chemical EOR processes, in particular polymer flooding and surfactant-polymer flooding. In chapter 2 we proposed a mathematical model for such flows in the form of a coupled nonlinear system comprising of an elliptic equation for pressure and transport equations for water saturation, polymer concentration and surfactant concentration. This model takes into account the capillary pressure. A new global pressure formulation has been developed which renders the form of the elliptic equation with a discontinuous coefficient to be the same as the one without the capillary pressure included in the model, except for the fact that now we solve the elliptic equation for the global pressure. In this global pressure formulation, the system of flow and transport equations bears some resemblance with that of a miscible displacement process.

A new hybrid numerical method for solving the system of flow and transport equations was introduced in chapter 3. This method is based on a discontinuous finite element method for the elliptic global pressure equation and a modified method of characteristics (MMOC) in combination with a time-implicit finite difference method for the transport equations. The discontinuous finite element method incorporates any discontinuity in the elliptic coefficient inside the finite element basis functions and facilitates efficient computation of the solution using a fixed computational mesh. The transport equations are primarily advection dominated with some diffusive regularization induced by the capillary pressure. The MMOC leverages this behavior to replace the advection operator by a suitable derivative along its characteristic curve and treats the capillary diffusion term

separately using an Eulerian grid. As a result, this method allows for larger time steps to be used in the numerical computation without sacrificing the accuracy or the stability.

In chapter 3, we also performed numerical analysis of the method to prove convergence by considering a reduced system, namely two-phase one component porous media flow in one-dimension. In the analysis presented, the convergence behavior of the MMOC based finite difference part of this hybrid numerical method was studied. An optimal order $O(h)$ error for the pressure gradient obtained by the finite element part was assumed, which has been numerically validated in [82]. Using this result, L^2 error estimates of the wetting phase saturation s and the component concentration c have been computed. The novelty in this proof is the consideration of the transport equation for a component which significantly complicates the analysis previously performed by others [55, 68] without any component. Basic ideas of the proof can be extended to two-dimensions and to two-components which were discussed but needless to say, the extension will be even more involved technically as one can see from the proof for the case presented in this dissertation.

In chapter 4 numerical results from simulations of several water, polymer and SP floods through heterogeneous porous media were reported. These demonstrate the convergence and robustness of the numerical method both qualitatively and quantitatively. In particular, the numerical method has been validated with an exact two dimensional solution for waterflooding. The corresponding error norms and order of accuracy calculations are in agreement with the L^2 estimates of the transport variables obtained from the convergence study and quantitatively demonstrate the accuracy of the method. Several other numerical simulations have been carried out on both a quarter five-spot geometry as well as on a rectilinear geometry with four different types of heterogeneous permeability fields - piecewise discontinuous with rectangular inclusions, the Upper-Ness formation type and the Tarbert formation type from the SPE10 dataset and a scalar, log-normal permeability

field generated using a stationary, isotropic, fractal Gaussian distribution. Two types of piecewise discontinuous permeability fields with one or more square inclusions have been used in the simulations. The method has been validated qualitatively by comparing these numerical results with those available in the literature. Simulations of a five-spot flood have been performed on a parallel and a diagonal grid to demonstrate that the method does not suffer from any serious grid orientation effects. The method is able to produce results which show that under similar reservoir conditions with heterogeneous Upper-Ness type permeability field data from the SPE10 benchmark problem, polymer flood improves the sweeping efficiency and inhibits growth of fingering instability in comparison to secondary recovery (waterflood). Numerical convergence of the method under grid refinement has been shown by performing polymer flood simulations in heterogeneous porous media using three different mesh sizes. The robustness of the method has been further demonstrated by simulating surfactant-polymer floods with various different compositions of the surfactant-polymer solution. The method is able to capture, fairly well, all the intricate details of the flow including the heterogeneity and viscosity driven finger formations. Using the saturation plots, the oil recovery curves and the water cut curves we are able to compare the relative effectiveness of different types of chemical flooding schemes in both types of flow geometry.

5.2 Future Directions

There is a broad range of problems in this area that are still open and can be the topic of future studies. Particularly, there are several questions that arise from the above work that are worthy of a more in-depth investigation.

For instance, a problem worthy of exploration would be a study on the effect of anisotropic mechanical dispersion of the dissolved components in two-phase, multicomponent flows. This will improve the SP flooding model by including an essential physical

phenomena that contributes to the effective flux of components and possibly helps in the partial suppression of the fingering instability. In [114] a study involving linear stabilization of three-layer porous media flow models of EOR for two different types of interfaces has revealed some promising results on the stabilizing capacity of molecular diffusion and mechanical dispersion. Various experimental [115], semianalytic [116] and numerical [117] studies have shown the significant impact of the dispersive flux in the transport of components in multiphase flow. Hence, it would be interesting to study the importance of this effect on the overall efficiency of the chemical enhanced oil recovery process. As discussed earlier, reducing grid orientation effect (GOE) is a crucial step in the development of any efficient reservoir simulator and it requires minimization of numerical diffusion. It would be an interesting challenge to accurately model the stabilizing effect of the physical anisotropic dispersion [100] while simultaneously minimizing numerical diffusion to control GOE.

There are also several computational and modeling challenges involved in developing our mathematical framework in order to make it more easily available for practical use. First and foremost, this would require extending the framework to simulate three dimensional problems by incorporating gravitational effects and carefully implementing the MMOC method on a 3D grid. Any such extension would also require optimization and possible parallelization of the code to increase the speed and efficiency of the massive computation. Another important question that we are already studying is the development of a generalized global pressure formulation for two-phase n-component flows in three dimensions. This would also require an in-depth investigation of the existence and uniqueness properties of the global pressure formulation. For a start, we would need to consider the global pressure formulation for two-component, two-phase flows, as proposed in this dissertation, and study its existence and uniqueness properties along the lines of similar analysis done for existing global pressure formulations [16, 20].

One of the major future research direction would be the study of *non-Newtonian flows in porous media*, especially viscoelastic flows. The SP laden aqueous phase in EOR, biofluids like blood and most other complex fluids that occur in multicomponent flows possess intricate rheological properties that directly influence the flow. The current practice in EOR is to model polymer solutions as power-law shear thinning fluids by ignoring the elastic effects and the existing literature is severely limited (see [118]). We have started exploring the models for various classes of non-Newtonian fluids like viscoelastic (Maxwell [119], Oldroyd-B [120], FENE-P), time-independent (Ellis [121], Herschel-Bulkley [122]) and time-dependent (Godfrey [123]) and ultimately, the aim is to develop a physically correct macroscale mathematical model for multiphase, multicomponent, *non-Newtonian* flow in porous media. We are also looking into modifying and extending the Newtonian flow framework to develop an efficient and accurate non-Newtonian flow framework that can also capture multiscale variations in permeability. This will help us study the non-Newtonian effects on the overall dynamics of the flow and also quantify the impact on the recovery efficiency and the displacement efficiency of the chemical flooding process.

REFERENCES

[1] J. A. Ferreira, G. Pena, and G. Romanazzi, "Anomalous diffusion in porous media," Appl. Math. Model., vol. 40, pp. 1850–1862, 2015.

[2] C.-C. Chueh, N. Djilali, and W. Bangerth, "An h-adaptive operator splitting method for two-phase flow in 3d heterogeneous porous media," SIAM J. Sci. Comput., vol. 35, no. 1, pp. 149–175, 2013.

[3] J. Sheng, Modern Chemical Enhanced Oil Recovery: Theory and Practice. Gulf Professional Publishing, 1st ed., 2011.

[4] P. Daripa, J. Glimm, B. Lindquist, M. Maesumi, and O. McBryan, "On the simulation of heterogeneous petroleum reservoirs," in Numerical Simulation in Oil Recovery, IMA Vol. Math. Appl. 11, (New York, NY), pp. 89–103, Springer, 1988.

[5] O. Karazincir, S. Thach, W. Wei, G. Prukop, T. Malik, and V. Dwarakanath, "Scale formation prevention during ASP flooding," in SPE International Symposium on Oilfield Chemistry, Society of Petroleum Engineers, 2011.

[6] E. Katsanis, P. Krumrine, and J. Falcone Jr., "Chemistry of precipitation and scale formation in geological systems," in SPE Oilfield and Geothermal Chemistry Symposium, Society of Petroleum Engineers, 1983.

[7] A. M. Alsofi, J. S. Liu, and M. Han, "Numerical simulation of surfactant-polymer coreflooding experiments for carbonates," J. Petrol. Sci. Eng., vol. 111, pp. 184–196, 2013.

[8] C. Gao, J. Shi, and F. Zhao, "Successful polymer flooding and surfactant-polymer flooding projects at Shengli oilfield from 1992 to 2012," J. Petrol. Explor. Prod. Technol., vol. 4, no. 1, pp. 1–8, 2014.

[9] Z. Wu, X. Yue, T. Cheng, J. Yu, and H. Yang, "Effect of viscosity and interfa-

cial tension of surfactant-polymer flooding on oil recovery in high-temperature and high-salinity reservoirs," J. Petrol. Explor. Prod. Technol., vol. 4, no. 1, pp. 9–16, 2014.

[10] Q. Yu, H. Jiang, and C. Zhao, "Study of interfacial tension between oil and surfactant polymer flooding," Petrol. Sci. Technol., vol. 28, no. 18, pp. 1846–1854, 2010.

[11] Y. Zhu, Y. Zhang, J. Niu, W. Liu, and Q. Hou, "The research progress in the alkali-free surfactant-polymer combination flooding technique," Petrol. Explor. Dev., vol. 39, no. 3, pp. 371–376, 2012.

[12] J. Bear, Dynamics of Fluids in Porous Media. New York: Elsevier, 1972.

[13] S. Whitaker, "Flow in porous media I: A theoretical derivation of Darcy's law," Transport in Porous Media, vol. 1, no. 1, pp. 3–25, 1986.

[14] L. W. Lake, R. Johns, B. Rossen, and G. Pope, Fundamentals of Enhanced Oil Recovery. Society of Petroleum Engineers, 2014.

[15] R. Helmig, Multiphase Flow and Transport Processes in the Subsurface. Springer-Verlag Berlin Heidelberg, 1st ed., 1997.

[16] G. Chavent and J. Jaffr$e^{'}$, Mathematical Models and Finite Elements for Reservoir Simulation. Amsterdam, North Holland: Studies in Mathematics and its applications, 1986.

[17] Z. Chen and R. E. Ewing, "Comparison of Various Formulations of Three-Phase Flow in Porous Media,," Journal of Computational Physics, vol. 132, no. 2, pp. 362–373, 1997.

[18] B. Amaziane and M. Jurak, "A new formulation of immiscible compressible two-phase flow in porous media," CR Mec., vol. 336, no. 7, pp. 600–605, 2008.

[19] B. Amaziane, M. Jurak, and A. Z. Keko, "Modeling and numerical simulations of immiscible compressible two-phase flow in porous media by the concept of global

pressure," Transport Porous Med., vol. 84, no. 1, pp. 133–152, 2010.

[20] B. Amaziane, M. Jurak, and A. Žgaljić Keko, "An existence result for a coupled system modeling a fully equivalent global pressure formulation for immiscible compressible two-phase flow in porous media," J. Differ. Equations, vol. 250, no. 3, pp. 1685–1718, 2011.

[21] B. Amaziane, M. Jurak, and A. Žgaljić Keko, "Numerical simulations of water-gas flow in heterogeneous porous media with discontinuous capillary pressures by the concept of global pressure," J. Comput. Appl. Math., vol. 236, no. 17, pp. 4227–4244, 2012.

[22] B. Amaziane, M. Jurak, and A. Žgaljić Keko, "Modeling compositional compressible two-phase flow in porous media by the concept of the global pressure," Computat. Geosci., vol. 18, no. 3-4, pp. 297–309, 2014.

[23] G. Chavent, "A fully equivalent global pressure formulation for three-phases compressible flows," Appl. Anal., vol. 88, no. 10-11, pp. 1527–1541, 2009.

[24] R. di Chiara Roupert, G. Chavent, and G. Schäfer, "Three-phase compressible flow in porous media: Total differential compatible interpolation of relative permeabilities," J. Comput. Phys., vol. 229, no. 12, pp. 4762–4780, 2010.

[25] P. Daripa and S. Dutta, "Modeling and simulation of surfactant-polymer flooding using a new hybrid method," Journal of Computational Physics, vol. 335, pp. 249–282, 2017.

[26] P. Daripa, J. Glimm, J. Grove, B. Lindquist, and O. McBryan, "Reservoir simulation by the method of front tracking," in Proc. of the IFE/SSI seminar on Reservoir Description and Simulation with Emphasis on EOR, pp. 1–18, 1986.

[27] P. Daripa, J. Glimm, B. Lindquist, and O. McBryan, "Polymer floods: A case study of nonlinear wave analysis and of instability control in tertiary oil recovery," SIAM J. Appl. Math., vol. 48, pp. 353–373, 1988.

[28] M. Islam and A. Chakma, "Mathematical modelling of enhanced oil recovery by alkali solutions in the presence of cosurfactant and polymer," J. Petrol. Sci. Eng., vol. 5, no. 2, pp. 105–126, 1991.

[29] Y. Shiyi, Y. Puhua, D. Zhongqiu, and S. Kuiyou, "Numerical simulation of alkali/surfactant/polymer flooding," in International meeting on petroleum engineering, pp. 139–152, 1995.

[30] L. J. Durlofsky, "A triangle based mixed finite element-finite volume technique for modeling two phase flow through porous media," J. Comput. Phys., vol. 105, no. 2, pp. 252–266, 1993.

[31] R. W. Healy and T. F. Russell, "A finite-volume Eulerian-Lagrangian localized adjoint method for solution of the advection-dispersion equation," Water Resour. Res., vol. 29, no. 7, pp. 2399–2413, 1993.

[32] Z. Chen, G. Huan, and H. Wang, "Computer simulation of compositional flow using unstructured control volume finite element methods," Computing, vol. 78, no. 1, pp. 31–53, 2006.

[33] S. A. Sadrnejad, H. Ghasemzadeh, S. A. Ghoreishian Amiri, and G. H. Montazeri, "A control volume based finite element method for simulating incompressible two-phase flow in heterogeneous porous media and its application to reservoir engineering," Petrol. Sc., vol. 9, no. 4, pp. 485–497, 2012.

[34] W. H. Reed and T. R. Hill, "Triangular mesh methods for the neutron transport equation," tech. rep., Los Alamos Scientific Lab., N.Mex. (USA), 1973.

[35] B. Rivière and M. F. Wheeler, "Discontinuous Galerkin methods for flow and transport problems in porous media," Commun. Numer. Meth. Eng., vol. 18, no. 1, pp. 63–68, 2002.

[36] P. Bastian, Higher Order Discontinuous Galerkin Methods for Flow and Transport in Porous Media, vol. 35, pp. 1–22. Berlin, Heidelberg: Springer Berlin Heidelberg,

2003.

[37] Y. Epshteyn and B. Rivière, "Fully implicit discontinuous finite element methods for two-phase flow," Appl. Numer. Math., vol. 57, no. 4, pp. 383–401, 2007.

[38] D. Nayagum, G. Schäfer, and R. Mosé, "Modelling two-phase incompressible flow in porous media using mixed hybrid and discontinuous finite elements," Comput. Geosci., vol. 8, no. 1, pp. 49–73, 2004.

[39] H. Hoteit and A. Firoozabadi, "Numerical modeling of two-phase flow in heterogeneous permeable media with different capillarity pressures," Adv. Water Resour., vol. 31, no. 1, pp. 56–73, 2008.

[40] H. Hoteit and A. Firoozabadi, "Multicomponent fluid flow by discontinuous Galerkin and mixed methods in unfractured and fractured media," Water Resour. Res., vol. 41, no. 11, 2005.

[41] J. Erhel, J.-R. de Dreuzy, and B. Poirriez, "Flow simulation in three-dimensional discrete fracture networks," SIAM J. Sci. Comput., vol. 31, no. 4, pp. 2688–2705, 2009.

[42] R. Ahmed, M. G. Edwards, S. Lamine, B. A. H. Huisman, and M. Pal, "Control-volume distributed multi-point flux approximation coupled with a lower-dimensional fracture model," J. Comput. Phys., vol. 284, pp. 462–489, 2015.

[43] Y. Efendiev, V. Ginting, T. Hou, and R. Ewing, "Accurate multiscale finite element methods for two phase flow simulations," J. Comput. Phys., vol. 220, pp. 155–174, 2006.

[44] E. Weinan, B. Engquist, X. Li, and W. Ren, "The heterogeneous multiscale method: A review," Commun. Comput. Phys., vol. 2, no. 3, pp. 367–450, 2007.

[45] H. Zhou, S. H. Lee, and H. A. Tchelepi, "Multiscale finite volume formulation for the saturation equations," Soc. Petrol. Eng. J., vol. 17, pp. 198–211, 2012.

[46] Z. Chen, "Characteristic-nonconforming finite-element methods for advection-

dominated diffusion problems," Comput. Math. Appl., vol. 48, pp. 1087–1100, 2004.

[47] F. H. Harlow, "The particle-in-cell computing method for fluid dynamics," Methods in Computational Physics, vol. 3, pp. 319 – 343, 1964.

[48] F. H. Harlow and J. E. Welch, "Numerical Calculation of Time-Dependent Viscous Incompressible Flow of Fluid with Free Surface," Physics of Fluids, vol. 8, no. 12, p. 2182, 1965.

[49] C. W. Hirt, A. A. Amsden, and J. L. Cook, "An arbitrary lagrangian-eulerian computing method for all flow speeds," Journal of Computational Physics, vol. 14, no. 3, pp. 227 – 253, 1974.

[50] D. Snider, "An Incompressible Three-Dimensional Multiphase Particle-in-Cell Model for Dense Particle Flows," Journal of Computational Physics, vol. 170, no. 2, pp. 523–549, 2001.

[51] D. Tskhakaya, K. Matyash, R. Schneider, and F. Taccogna, "The particle-in-cell method," Contributions to Plasma Physics, vol. 47, no. 8-9, pp. 563–594, 2007.

[52] J. Douglas Jr., F. Furtado, and F. Pereira, "On the numerical simulation of waterflooding of heterogeneous petroleum reservoirs," Comput. Geosc., vol. 1, pp. 155–190, 1997.

[53] H. Wang, R. E. Ewing, G. Qin, S. L. Lyons, M. Al-Lawatia, and S. Man, "A family of Eulerian-Lagrangian Localized Adjoint Methods for multi-dimensional advection-reaction equations," J. Comput. Phys., vol. 152, no. 1, pp. 120–163, 1999.

[54] J. Douglas Jr., D. Frías, N. Henderson, and F. Pereira, "Simulation of single-phase multicomponent flow problems in gas reservoirs by Eulerian-Lagrangian techniques," Transport Porous Med., vol. 50, no. 3, pp. 307–342, 2003.

[55] J. Douglas Jr. and T. F. Russell, "Numerical methods for convection-dominated diffusion problems based on combining the method of characteristics with finite

element or finite difference procedures," SIAM J. Numer. Anal., vol. 19, no. 5, pp. 871–885, 1982.

[56] H. K. Dahle, M. S. Espedal, R. E. Ewing, and O. Sævereid, "Characteristic adaptive subdomain methods for reservoir flow problems," Numer. Meth. Part. D. E., vol. 6, no. 4, pp. 279–309, 1990.

[57] J. Douglas Jr., C.-S. Huang, and F. Pereira, "The modified method of characteristics with adjusted advection," Numer. Math., vol. 83, no. 3, pp. 353–369, 1999.

[58] M. A. Celia, T. F. Russell, I. Herrera, and R. E. Ewing, "An Eulerian-Lagrangian localized adjoint method for the advection-diffusion equation," Adv. Water Resour., vol. 13, no. 4, pp. 187–206, 1990.

[59] T. Arbogast and M. F. Wheeler, "A characteristics-mixed finite element method for advection-dominated transport problems," SIAM J. Numer. Anal., vol. 32, no. 2, pp. 404–424, 1995.

[60] J. Douglas Jr., F. Pereira, and L.-M. Yeh, "A locally conservative Eulerian-Lagrangian numerical method and its application to nonlinear transport in porous media," Comput. Geosci., vol. 4, no. 1, pp. 1–40, 2000.

[61] F. Gao and Y. Yuan, "The characteristic finite volume element method for the nonlinear convection-dominated diffusion problem," Comput. Math. Appl., vol. 56, no. 1, pp. 71 – 81, 2008.

[62] K. Wang, H. Wang, and M. Al-Lawatia, "An Eulerian-Lagrangian discontinuous Galerkin method for transient advection-diffusion equations," Numer. Meth. Part. D. E., vol. 23, no. 6, pp. 1343–1367, 2007.

[63] M. S. Mahmood, "Solution of nonlinear convection-diffusion problems by a conservative Galerkin-characteristics method," Numer. Math., vol. 112, no. 4, pp. 601–636, 2009.

[64] H. Wang, "An optimal-order error estimate for an ELLAM scheme for two-

dimensional linear advection-diffusion equations," SIAM Journal on Numerical Analysis, vol. 37, no. 4, pp. 1338–1368, 2000.

[65] P. Daripa and S. Dutta, "Convergence analysis of a characteristics-based hybrid method for multicomponent transport in porous media," arXiv:1707.00035 [math.NA], 2017.

[66] P. Daripa, J. Glimm, B. Lindquist, M. Maesumi, and O. McBryan, "On the simulation of heterogeneous petroleum reservoirs," in Numerical Simulation in Oil Recovery, IMA Vol. Math. Appl. 11, (New York, NY), pp. 89–103, Springer, 1988.

[67] P. Daripa, J. Glimm, B. Lindquist, and O. McBryan, "Polymer floods: A case study of nonlinear wave analysis and of instability control in tertiary oil recovery," SIAM Journal on Applied Mathematics, vol. 48, pp. 353–373, 1988.

[68] J. Douglas Jr., "Finite difference methods for two-phase incompressible flow in porous media," SIAM J. Numer. Anal., vol. 20, no. 4, pp. 681–696, 1983.

[69] H. L. Chang, Z. Q. Zhang, Q. M. Wang, Z. S. Xu, Z. D. Guo, H. Q. Sun, X. L. Cao, and Q. Qiao, "Advances in polymer flooding and alkaline/surfactant/polymer processes as developed and applied in the People's Republic of China," J. Pet. Tech., vol. 58, no. 02, pp. 84–89, 2006.

[70] P. Daripa, J. Glimm, B. Lindquist, and O. McBryan, "Polymer floods: A case study of nonlinear wave analysis and of instability control in tertiary oil recovery," SIAM J. Appl. Math., vol. 48, pp. 353–373, 1988.

[71] M. Muskat and M. W. Meres, "The flow of heterogeneous fluids through porous media," Journal of Applied Physics, vol. 7, no. 921, pp. 346–363, 1936.

[72] J. Glimm, E. Isaacson, D. Marchesin, and O. McBryan, "Front tracking for hyperbolic systems," Adv. Appl. Math., vol. 2, no. 1, pp. 91–119, 1981.

[73] I.-L. Chern, J. Glimm, O. Mcbryan, B. Plohr, and S. Yaniv, "Front tracking for gas dynamics," J. Comput. Phys., vol. 62, no. 1, pp. 83–110, 1986.

[74] A. T. Corey, Mechanics of Immiscible Fluids in Porous Media. Littlton, Colorado: Water Resources Publications, 1986.

[75] M. T. van Genuchten, "A closed form equation for predicting the hydraulic conductivity of unsaturated soils," Soil Sci. Soc. Am. J., vol. 44, pp. 892–898, 1980.

[76] J. C. Parker, R. J. Lenhard, and T. Kuppusamy, "A parametric model for constitutive properties governing multiphase flow in porous media," Water Resour. Res., vol. 23, no. 4, pp. 618–624, 1987.

[77] B. Ghanbarian-Alavijeh, A. Liaghat, G.-H. Huang, and M. T. van Genuchten, "Estimation of the van Genuchten soil water retention properties from soil textural data," Pedosphere, vol. 20, no. 4, pp. 456–465, 2010.

[78] R. H. Brooks and A. T. Corey, "Properties of porous media affecting fluid flow," J. Irrig. Drain. Div., vol. 92,(IR2), pp. 61–90, 1966.

[79] C. L. Brown and G. A. Pope, "Simulation of surfactant-enhanced aquifer remediation," Water Resour. Res., vol. 30, pp. 2959–2977, November 1994.

[80] J. O. Amaefule and L. L. Handy, "Effect of interfacial tensions on relative oil/water permeabilities of consolidated porous media," Soc. Petrol. Eng. J., vol. 22, no. 3, pp. 371–381, 1982.

[81] Q. Liu, M. Dong, S. Ma, and Y. Tu, "Surfactant enhanced alkaline flooding for Western Canadian heavy oil recovery," Colloid. Surface. A, vol. 293, no. 13, pp. 63 – 71, 2007.

[82] S. Hou, W. Wang, and L. Wang, "Numerical method for solving matrix coefficient elliptic equation with sharp-edged interfaces," J. Comput. Phys., vol. 229, pp. 7162–7179, 2010.

[83] Z. Li, T. Lin, and X. Wu, "New Cartesian grid methods for interface problems using the finite element formulation," Numer. Math., vol. 96, pp. 61–98, 2003.

[84] X.-D. Liu, R. P. Fedkiw, and M. Kang, "A boundary condition capturing method for

Poisson's equation on irregular domains," J. Comput. Phys., vol. 160, pp. 151–178, 2000.

[85] R. E. Ewing and H. Wang, "A summary of numerical methods for time-dependent advection-dominated partial differential equations," J. Computat. Appl. Math., vol. 128, no. 1-2, pp. 423–445, 2001.

[86] J. H. Bramble, "Second order finite difference analogue of the first biharmonic boundary value problem," Numer. Math., vol. 9, pp. 236–249, 1966.

[87] J. Hagoort, "Displacement Stability of Water Drives in Water-Wet Connate-Water-Bearing Reservoirs," Society of Petroleum Engineers Journal, vol. 14, no. 1, pp. 63–74, 1974.

[88] J. Li and B. Rivière, "Numerical solutions of the incompressible miscible displacement equations in heterogeneous media," Comput. Method Appl. M., vol. 292, pp. 107–121, 2014.

[89] M. R. Todd, P. M. O'Dell, and G. J. Hirasaki, "Methods for increased accuracy in numerical reservoir simulators," Soc. Petrol. Eng. J., vol. 12, no. 6, pp. 515–530, 1972.

[90] J. Kozdon, B. Mallison, and M. Gerritsen, "Robust multi-D transport schemes with reduced grid orientation effects," Transport in Porous Media, vol. 78, no. 1, pp. 47–75, 2009.

[91] W. H. Chen, L. J. Durlofsky, B. Engquist, and S. Osher, "Minimization of grid orientation effects through use of higher order finite difference methods," in SPE Advanced Technology Series, vol. 1, pp. 43–52, 1993.

[92] D. S. Wolcott, H. Kazemi, and R. H. Dean, "A Practical Method for Minimizing the Grid Orientation Effect in Reservoir Simulation," in SPE Annual Technical Conference and Exhibition, 6-9 October, Denver, Colorado, 1996.

[93] K. Pruess and F. S. Bodvarsson, "A Seven-Point Finite Difference Method for Im-

proved Grid Orientation Performance in Pattern Steamfloods," in SPE Reservoir Simulation Symposium, 15-18 November, San Francisco, California, 1983.

[94] G. R. Shubin and J. B. Bell, "An analysis of the grid orientation effect in numerical simulation of miscible displacement," Computer Methods in Applied Mechanics and Engineering, vol. 47, no. 1-2, pp. 47–71, 1984.

[95] Z. Heinemann, C. Brand, M. Munka, and Y. Chen, "Modeling Reservoir Geometry With Irregular Grids," SPE Reservoir Engineering, vol. 6, no. 2, pp. 225–232, 1991.

[96] K. Liu, G. Subramanian, D. I. Dratler, J. P. Lebel, and J. A. Yerian, "A general unstructured grid, EOS-based, fully-implicit thermal simulator for complex reservoir processes," in SPE Reservoir Simulation Symposium,26-28 February, Houston, Texas, pp. 153–158, 2007.

[97] J. Yanosik and T. McCracken, "A Nine-Point, Finite-Difference Reservoir Simulator for Realistic Prediction of Adverse Mobility Ratio Displacements," Society of Petroleum Engineers Journal, vol. 19, no. 4, pp. 253–262, 1979.

[98] G. S. Shiralkar, "Reservoir Simulation of Generally Anisotropic Systems," SPE Reservoir Engineering, no. August, pp. 409–414, 1990.

[99] C. T. Tan and G. M. Homsy, "Stability of miscible displacements in porous media : Radial source flow," Physics of Fluids, vol. 30, no. 5, pp. 1239–1245, 1987.

[100] A. Riaz, C. Pankiewitz, and E. Meiburg, "Linear stability of radial displacements in porous media : Influence of velocity-induced dispersion and concentration-dependent diffusion," Physics of Fluids, vol. 16, no. 10, pp. 3592–3598, 2004.

[101] J. Kozdon, M. Gerritsen, and M. Christie, "Grid orientation revisited: Near-well, early-time effects and solution coupling methods," Transport Porous Med., vol. 73, no. 3, pp. 255–277, 2008.

[102] K. Pruess, "Grid orientation and capillary pressure effects in the simulation of water injection into depleted vapor zones," Geothermics, vol. 20, no. 5/6, pp. 257–277,

1991.

[103] C. Brand, J. Heinemann, and K. Aziz, "The grid orientation effect in reservoir simulation," in Proceedings of SPE Symposium on Reservoir Simulation, pp. 225–232, 1991.

[104] G. Chavent, "A new formulation of diphasic incompressible flows in porous media," in Applications of Methods of Functional Analysis to Problems in Mechanics: Joint Symposium IUTAM/IMU Held in Marseille, September 1–6, 1975 (P. Germain and B. Nayroles, eds.), pp. 258–270, Berlin, Heildelberg: Springer Berlin Heidelberg, 1976.

[105] Y. C. Yortsos, "The relationship between immiscible and miscible displacement in porous media," AIChE J., vol. 33, no. 11, pp. 1912–1915, 1987.

[106] M. A. Christie and M. J. Blunt, "Tenth SPE Comparative Solution Project: A Comparison of Upscaling Techniques," SPE Reserv. Eval. Eng., vol. 4, no. 4, pp. 308–317, 2001.

[107] P. Daripa and G. Pasa, "An optimal viscosity profile in enhanced oil recovery by polymer flooding," Int. J. Eng. Sci., vol. 42, no. 19-20, pp. 2029–2039, 2004.

[108] P. Daripa and X. Ding, "A numerical study of instability control for the design of an optimal policy of enhanced oil recovery by tertiary displacement processes," Transport Porous Med., vol. 93, no. 3, pp. 675–703, 2012.

[109] P. Daripa, "Fluid dynamical and modeling issues of chemical flooding for enhanced oil recovery," in ASME 2013 32nd International Conference on Ocean, Offshore and Arctic Engineering, (Nantes, France), pp. 1–8, 2013.

[110] M. R. Borges, F. Pereira, and H. P. Amaral Souto, "Efficient generation of multiscale random fields: A hierarchical approach," Int. J. Numer. Method. Biomed. Eng., vol. 26, pp. 176–189, 2010.

[111] J. Glimm, W. B. Lindquist, F. Pereira, and Q. Zhang, "A theory of macrodispersion

for the scale-up problem," Transport Porous Med., vol. 13, no. 1, pp. 97–122, 1993.

[112] F. Furtado and F. Pereira, "Crossover from nonlinearity controlled to heterogeneity controlled mixing in two-phase porous media flows," Computat. Geosci., vol. 7, no. 2, pp. 115–135, 2003.

[113] E. Abreu, "Numerical modelling of three-phase immiscible flow in heterogeneous porous media with gravitational effects," Math. Comput. Simulat., vol. 97, pp. 234–259, 2014.

[114] P. Daripa and C. Gin, "Studies on dispersive stabilization of porous media flows," Physics of Fluids, vol. 28, no. 8, p. 082105, 2016.

[115] J. M. P. Q. Delgado, "Longitudinal and Transverse Dispersion in Porous Media," Chemical Engineering Research and Design, vol. 85, no. 9, pp. 1245–1252, 2007.

[116] K. S. Schmid, S. Geiger, and K. S. Sorbie, "Semianalytical solutions for cocurrent and countercurrent imbibition and dispersion of solutes in immiscible two-phase flow," Water Resources Research, vol. 47, no. 2, pp. 1–16, 2011.

[117] S. Bekri and P. M. Adler, "Dispersion in multiphase flow through porous media," International Journal of Multiphase Flow, vol. 28, no. 4, pp. 665–697, 2002.

[118] J. Pearson and P. Tardy, "Models for flow of non-Newtonian and complex fluids through porous media," Journal of Non-Newtonian Fluid Mechanics, vol. 102, no. 2, pp. 447–473, 2002.

[119] B. Mena, O. Manero, and L. G. Leal, "The influence of rheological properties on the slow flow past spheres," J. Non-Newton. Fluid, vol. 26, pp. 247–275, 1987.

[120] R. B. Bird, R. C. Armstrong, and O. Hassager, Dynamics of Polymeric Liquids, vol. 1. US: Wiley, 2nd ed., 1987.

[121] T. J. Sadowski and R. B. Bird, "Non-Newtonian flow through porous media. i. Theoretical," T. Soc. Rheol., vol. 9, pp. 243–250, 1965.

[122] A. H. P. Skelland, Non-Newtonian Flow and Heat Transfer. New York: Wiley,

1967.

[123] J. C. Godfrey, “Steady shear measurement of thixotropic fluid properties,” Rheol. Acta, vol. 12, pp. 540–545, 1973.